A SCANNING ION MICROSCOPE WITH

A FIELD IONIZATION SOURCE

Jonathan Harris Orloff
B.S., Massachusetts Institute of Technology, 1964

A dissertation submitted to the faculty
of the Oregon Graduate Center
in partial fulfillment of the
requirements for the degree
Doctor of Philosophy
in
Applied Physics

December 1976

This thesis has been examined and approved by the following Thesis Committee:

Lynwood W. Swanson, Thesis Advisor
Professor

Douglas F. Barofsky
Associate Professor

Gertrude F. Rempfer
Professor, Portland State University

O. Hayes Griffith
Professor, University of Oregon

ACKNOWLEDGMENT

I wish to express my considerable thanks to Professor Swanson for suggesting this area of research, for his continuous help and support in it and for his physical insight which was of such great value in improving my understanding of this branch of physics.

TABLE OF CONTENTS

FIGURES

ABSTRACT

This work was undertaken to determine the feasibility of using a field ionization (FI) source to produce fine focus ion beams. Operating parameters for a FI source have been measured and a source sensitivity of $\approx 5 \times 10^{-5}$ A sr^{-1} $torr^{-1}$ was found for both H_2 and Ar at 77 K. The source is gas phase, differentially pumped with typical operating pressures of $1 - 30 \times 10^{-3}$ torr at 77 K, resulting in a maximum source brightness $\approx 10^{8}$ A cm^{-2} sr^{-1} and angular intensity of $\approx 10^{-6}$ A sr^{-1} with beam energies of 10 - 20 keV. Angular distributions were measured and found to be uniform near $\theta = 0°$, with the beam confined to $\pm 20°$. A scanning ion microscope (SIM) was built to further evaluate the source. The SIM has been operated with currents on the specimen of $10^{-11} - 10^{-10}$ amperes in the secondary electron mode with contrast provided primarily by the $\sec(\theta)$ dependence of the secondary electron yield, where θ is the angle between the beam and the specimen normal. Secondary electrons are detected and amplified with a channeltron multiplier and images generated as with a conventional SEM. All electrostatic optics are used in a doublet arrangement, and with this configuration current is independent of working distance which is 3 - 4 cm. A current of 5×10^{-11} A was focussed into a spot of ≈ 6500 Å with H_2 gas, the resolution being limited by chromatic aberration caused by the $\approx$ 4 eV energy spread of the two component ($H^+ + H_2^+$) beam. Signal to

noise ratio measurements on the source made at the specimen position show that the bulk of the noise power spectrum falls below f = 30 Hz.

I. INTRODUCTION

This thesis describes the design and test of a scanning ion microscope which uses a field ionization ion source. It includes reviews of basic electron optics and the theory of field ionization which I hope will be useful to those starting work in the areas of field ionization and ion optics.

This project was undertaken to determine whether a field ionization (FI) source could be adapted to produce focussed ion beams for use in an ion microprobe. The goals were to build and test a FI source, to design and construct a source which could be used with a microprobe, then to build the microprobe and determine in what current-resolution regime it would prove to be useful, i.e., equal or superior to conventional ion source microprobes.

Ion beam devices are used for many applications. At high energies ($\gtrsim$ 1 MeV) they are common in nuclear and high energy research. At intermediate energies ($\sim$ 100 - 300 keV) ion beams are used for implantation in transistor and integrated circuit production. At low energies ($\lesssim$ 50 keV) ion beams have been utilized primarily in ion probe microanalyzers for elemental analysis (for a review of ion beams in microanalysis see the article Ion Probe Microanalysis by H. Liebl (reference 1)). This is an application which may have a limited future because, while the two methods used (Ion Scattering Spectroscopy - ISS and Secondary Ion Mass Spectroscopy - SIMS) have

great sensitivity, they lack spatial resolution and speed in comparison with electron beam techniques such as Auger analysis and electron microprobes.[2] Except where very great sensitivity or the ability to detect isotopes is needed, SIMS really has no advantage over the other means of elemental analysis. This is especially true because the resolution of ion microprobes is severely limited by the need for high currents in SIMS and ISS. Present ion sources are not capable of producing beams which have usable intensity for elemental analysis when highly focussed, whereas even conventional (thermionic) electron sources permit elemental analysis to be done at the ~ 1 μm level.

Other uses for low energy ion beams include microscopy and micromachining (high resolution sputtering). Ion beams have been used in transmission microscopes in place of electron beams, with modest results.[3] Broad area sputtering with ions is an old technique, of course. With sufficient beam intensity it can be done in a programmed manner by using a probe.

The scanning electron microscope (SEM) is famous and resolution of 100 Å is more or less routine for this instrument and 30 Å has been achieved under certain circumstances in the secondary electron mode. 5 Å has been attained[4] in the scanning transmission mode with thin specimens. To date little work has been done to produce images with a focussed ion beam. If the problem of providing sufficient beam intensity at very small spot sizes can be overcome,

the scanning ion microscope (SIM) has the potential for even higher resolution than the SEM because of the reduced de Broglie wavelength of the ions and reduced scattering in the specimen. In the secondary electron mode the resolution of the SEM is limited by the scattering of the beam as it enters the specimen which causes secondaries to be emitted over an area much larger than the beam cross section. Electron beam fabrication machines which write on electron sensitive resist appear to be limited to 500 - 1000 Å because of the same problem. The limit is due to specimen-beam interaction, not electron source or optics.

The main advantage of an ion beam over an electron beam for this sort of application is that the probability for the scattering of the beam is orders of magnitude less than for an electron beam, so the beam resolution is not degraded upon entering the specimen. Of course, for this advantage to be of any value the beam diameter must compare with that of an electron beam used for the same application - $\lesssim$ 1000 Å for fabrication and $\lesssim$ 100 Å for scanning microscopy. Resolution of this magnitude has not been practical to date with any ion sources regardless of the quality of the optics used to focus the beam. The reason is none of the ion sources used heretofore have had sufficient brightness to provide useful current at $\lesssim$ 3000 Å resolution.

Until quite recently, ion microprobes have used duoplasmatron ion sources almost exclusively[1,5] and the best performance demonstrated

was by Drummond and Long,[5] who achieved a resolution of 0.2 μm with an unreported amount of Ar beam current at 20 kV. They also obtained 5 nA beam current with a 1 μm beam diameter. Hill[6] demonstrated an estimated 2.5×10^{-10} A of Ar current with a beam diameter of 0.3 μm at 30 kV. While these are significant achievements, the currents and resolution fall short of the needs for either ion microscopy or high resolution sputtering and ion implantation. For example, in high density memories a high read and write rate is essential. If the writing consists of ion-implanted regions in a substrate, a 0.3 μm beam would allow at the most 10^9 bits/cm^2 and if we assume 1000 ions/bit, the writing rate would be $\sim 2.5 \times 10^6$ bits/sec. With the same current and resolution it would be possible to sputter through a 0.1 μm gold foil at the rate of only $\sim$ 0.1 mm/sec. In either case, if sub-0.1 μm resolution were desired, the rapid decrease in current as the beam diameter falls below $\sim$ 0.5 μm renders the duoplasmatron source in its present form unsuitable for this application. A brighter source is essential for high resolution work, and the duoplasmatron source with $\beta \sim 10^2 - 10^3$ A/cm^2 sr isn't adequate ($\beta \equiv$ electron optical brightness).

The FI source suggested itself as a solution to the problem of insufficient source brightness. The field electron (FE) source has been used for some years in commercial high brightness electron sources and achieves its spectacular brightness through modest current and very small virtual source size. It is known that the

virtual source size of the FI source is extremely small since the resolution of the FI microscope is ~ 2 Å.

The physical construction of a FI source used in a SIM is quite simple, consisting of a field emitter anode and a cathode containing an aperture. The field emitter is a thin (~ 0.005") wire usually made of a refractory material such as W or Ir, which has been etched at one end to a fine radius. Typically, the radius of the end of the wire is ~ 1000 Å. The region around the emitter of a gas phase supplied FI source is pressurized to ~ 10^{-2} torr with the gas to be ionized and the source is differentially pumped through the beam aperture. The background vacuum for the FI source should be $\lesssim 10^{-5}$ torr. The applied electric field increases with ionization potential of the gas to be ionized - generally it varies from 5×10^7 to 4×10^8 V/cm.

The most striking characteristic of both FI and FE sources is their extremely small apparent source size - ~ 8 Å for a FI source and ~ 30 Å for a FE source when apertured to ~ 0.005 rad beam angle. Apparent source sizes have been calculated using ray tracing calculations of Wiesner;[7] the results are plotted in Figure 1 for emitters of radii 750 Å and 1500 Å. Because of these small source sizes FI and FE sources are extraordinarily bright. Even though the total current from a gas phase FI source is 10^{-8} - 10^{-7} A the brightness can be ~ 10^8 A/cm^2 sr. This is to be compared with current densities available from other ion sources[8] (see Table I).

TABLE I

Source	Total Current (A)	Current Density (A/cm^2)	Energy Spread (eV)
Field Ionization	10^{-9} to 10^{-8}	10^{3}	2 - 5
Duoplasmatron	10^{-3} to 10^{-1}	10^{-2} to 1	10
RF	10^{-4} to 10^{-2}	10^{-2} to 10^{-1}	30 to 500
Penning Discharge	10^{-1} to 1	10^{-4}	10
Sputter	10^{-4} to 10^{-2}	10^{-3} to 10^{-2}	10 to 50

When a source such as the FI source (or the field electron source in electron optics) is used in a probe, the appropriate optics are quite different from that used with a duoplasmatron source (or a thermionic electron source). The reason is that the gaussian source size is extremely small to begin with, so the optical system operates near unit magnification rather than in the strong demagnification mode.

The problem faced in the microprobe is how to image the small source onto the specimen with maximum current. One answer to this problem is to use a doublet, with the first lens forming a collimated beam (source located at f_o, the focal point) and the second focussing the collimated beam on the specimen. Blanking plates, stigmator, etc. are placed between the lenses. Beam deflectors can be placed either between the lenses or after the final lens. With the object for the second lens of the doublet located at $z = \infty$ the overall lateral magnification of the doublet is given by $M = f_p / f_o$ where f_o = focal length of the objective (first) lens and

f_p = focal length of the projector (second) lens. The terminology is that of the transmission electron microscope (TEM) and is appropriate because the objective lens attempts to resolve the source which has a (virtual) size $r_g \sim 10$ A. Providing $M \gtrsim 2$ the image of the source on the specimen will have a diameter given by*

$$d = 2M[(r_g)^2 + (r_s)^2 + (r_c)^2]^{\frac{1}{2}} \qquad (1)$$

where $r_s = \frac{1}{4}C_s\alpha^3$ is the contribution of the spherical aberration and $r = \frac{1}{2}C_c \frac{\Delta V}{V} \alpha$ is the contribution due to the chromatic aberration of the objective lens. C_s and C_c are the experimental spherical and chromatic aberration coefficients of the lens, respectively. Each has units of length. V is the beam accelerating voltage, ΔV is the beam energy spread (FWHM) and α is the half-angle of the beam determined by the diameter of the objective aperture located just behind the objective lens. Diffraction of the ion beam is completely negligible if V > 100 volts. In this work the energy of the ion beams varied between about 10 keV and 15 keV.

When hydrogen is field ionized two species of ions, H^+ and H_2^+ dominate the current. At the typical ionizing field of $\approx 2 \times 10^8$ V/cm the ratio of H_2^+ to H^+ is about two to one.[9] Each species has an energy spread of $\approx$ 1 volt FWHM and the centroids are separated by approximately 3.5 volts.[9] The energy spread of the beam is then taken to be 4 volts, FWHM.

If the source is located so that $f_o \approx 5$ mm then $C_s = 88$ mm, $C_c = 18$ mm, $\Delta V = 4$ volts, V is assumed = 12 kV, $f_p = 30$ mm and

*see Section II

$\alpha = 0.012$, then

$$d = 2M[(2.2 \times 10^7 \times (.012)^3)^2 + (9 \times 10^7 \times \frac{4}{12{,}000} .012)^2]^{\frac{1}{2}}$$

$$= 6300 \text{ A.}$$

If a higher resolution beam is desired α must be reduced. Because the spherical aberration term depends on α^3 the spherical contribution rapidly becomes unimportant and the system is chromatic aberration limited: at $d = 0.1$ μm, $\alpha = 3$ mr, $r_c = 0.5$ μm and $r_s = 8 \times 10^{-4}$ μm.

If a gas other than hydrogen is field ionized a reduction in the chromatic term may result. Typical values for the energy spread of mono-atomic gas are ~ 2 eV, for example. Use of such a gas (He, Ar, Xe) would improve the resolution by ~ 2.5 times, all else being equal.

A comparison of a state of the art duoplasmatron source[8] and a FI source using the same optical configuration has been made and is presented in Figure 2. It is clear that the FI source is the superior source when it is desired to focus the ion beam to a diameter $\lesssim$ 2000 Å. In fact, if the ion beam were focussed to 100 Å the FI source could deliver ~ 5×10^{-15} A (see also Section IV).

The energy spread of the FI source increases with the applied electric field. Since the current also increases with field, a balance must be struck between current and energy spread.

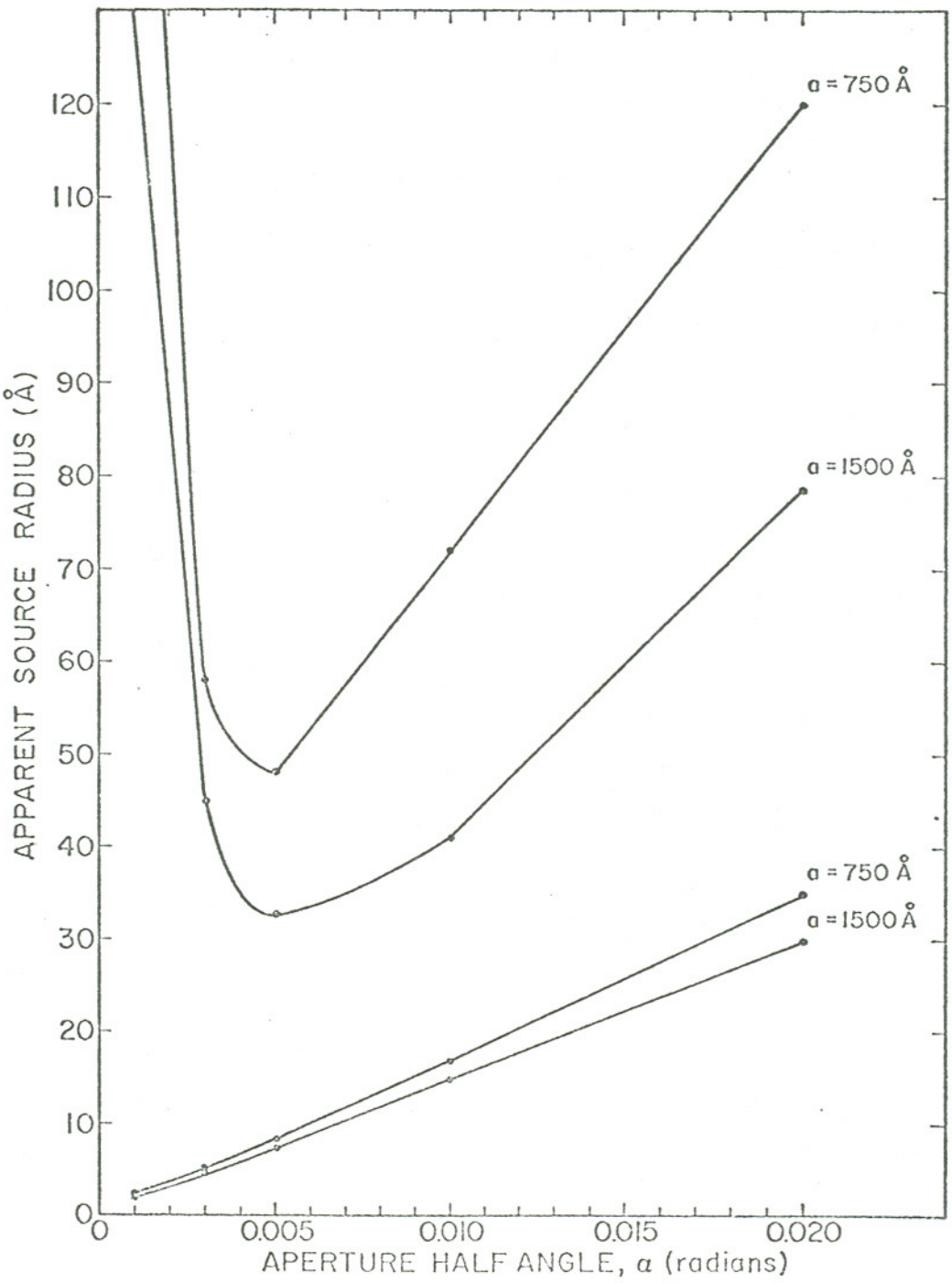

Fig. 1. Apparent source radius for electrons (upper two curves) and ions (lower two curves) of a field emitter is given for two emitter radii a as a function of beam half angle α. Data are obtained from Weisner's[7] computer calculation of charged particle trajectories.

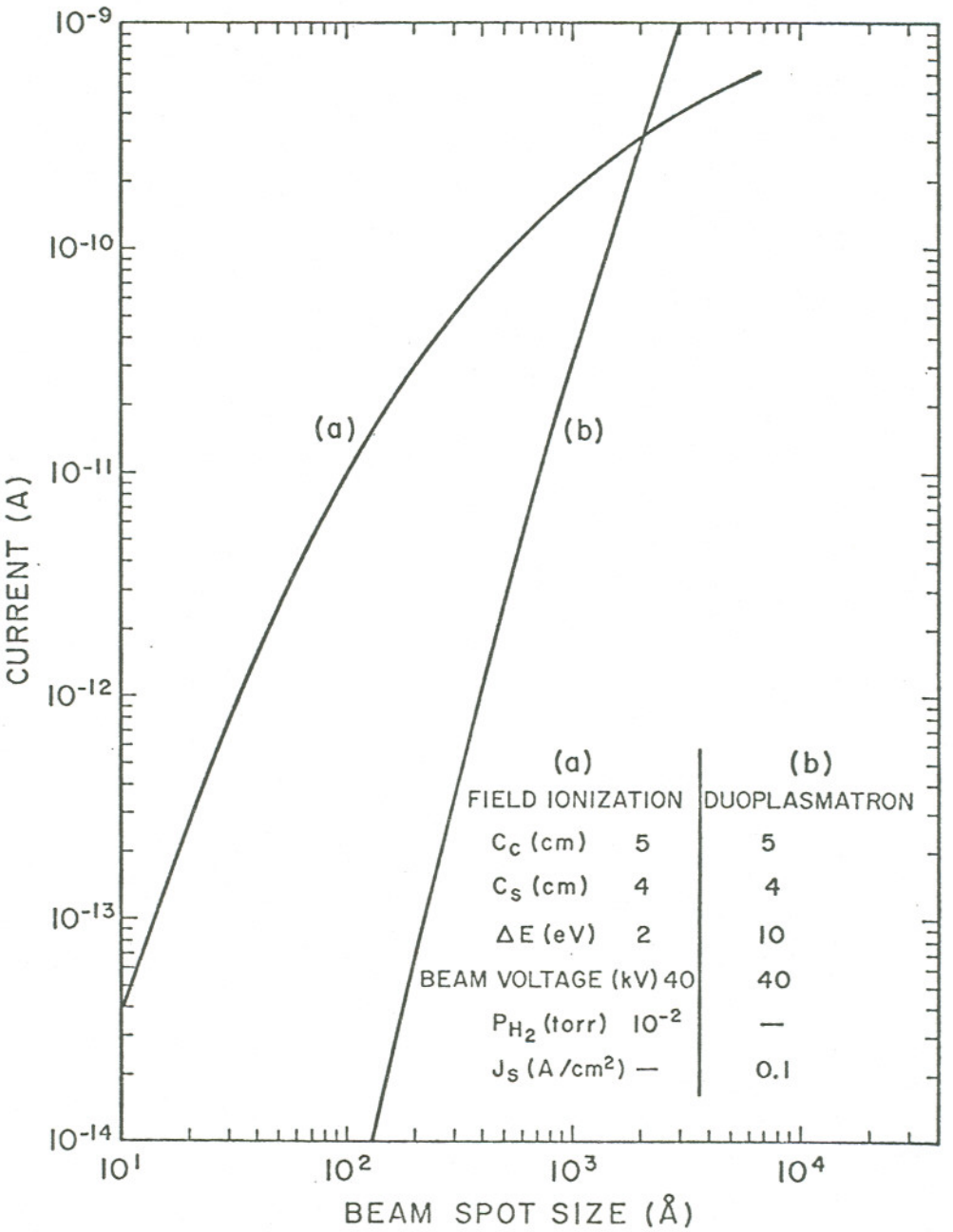

Fig. 2. A comparison of the calculated current vs. focussed spot size for a state of the art FI gun using H_2 gas and an advanced state of the art duoplasmatron gun (using parameters from Reference 6).

Beam energy spread is of importance because at the small beam divergence angles which must be employed in high resolution work chromatic aberration is the dominant lens aberration up to a beam half angle of $\alpha = 0.010$ rad. The evident superiority of the FI source over other ion sources is seen from Table I, where the energy spread of the other sources is greater by factors of 5 to 100.

Practically any gaseous compound can be field ionized. In some cases different ionic species may be formed with different energies. For example, H forms H^+, H_2^+ and H_3^+. To avoid severe chromatic aberration, only one species can be used, the other(s) being removed by a magnetic filter or by choosing a field at which one species is dominant, if current considerations permit.

In addition to field ionization of gaseous compounds, it is also possible to operate the emitter in a "field desorption" (FD) mode whereby the ionizable material is the emitter itself (usually called field evaporation) or a thin film of material on the emitter surface supplied by surface diffusion. The FD mode of operation, although it has received little study thus far, has the possibility of providing even higher current densities than gas phase FI sources. Recent studies have shown that several hundred μA of current can be obtained from liquid metal sources.[10]

New applications for high resolution ion beams have mainly to do with semiconductor device fabrication. The limit of how finely information can be written is the wavelength of the radiation used

for the writing. Hence, masks for integrated circuit (IC) manufacture are limited to a scale of $\approx$ 1 micron when light is used as the writing medium. The use of electron beams permits a reduction in scale of $\approx$ 10 X (electron beam lithography), the limit now being beam scatter in the resist material. The use of ion beams may permit another reduction of 2 X - 10 X by eliminating the scattering problem.

Another approach to miniaturization of IC's is to directly implant ions of dopant material with highly focussed beams, which again require FI sources. This would require higher voltage (10 - 100 kV) systems capable of forming beams of a variety of materials (liquid Ga and In sources, gas phase phosphorous, boron and nitrogen sources) with $\leqslant$ 0.2 micron resolution.

Recently hydrogen ion beams have been used[11] to create highly localized crystal damage in the junction regions of transistors in order to vary the properties of the device. The use of a FI source would permit this to be done on a smaller (higher resolution) scale.

There has long been interest in super high density memories. By the use of highly focussed ion beams for ion implantation it may be possible to write 10^{12} bits/cm^2. This requires writing on a 100 Å scale. (The read-out of such a memory would require an electron beam with a current density $\sim 10^3$ A/cm^2 on target. Both reading and writing requirements can be met only with FE and FI sources respectively.)

A matrix of applications for high resolution ion beams is presented in Table II.

TABLE II

	SIM	High Resolution Ion Implantation	High Resolution Ion Milling	High Density Memory Writing	Semiconductor Device "Tailoring"
Hydrogen Source	X				X
Xenon Source			X	X	X
Liquid Metal Sources		X	X	X	
Other Gas Sources	X	X			

The above considerations were the impetus for the design and construction of the scanning ion microscope. Somewhat earlier, Levi-Setti[12] began work on a scanning proton microscope using a FE source made by adapting a Crewe electron gun. Because of the configuration of this gun he and his coworkers were only able to extract $\sim 10^{-15}$ amperes, but the resolution was 0.1 - 0.2 μm. The current limitation was caused by low gas pressure ($\lesssim 10^{-4}$ torr) in the source and lack of cooling of the source, which probably accounts for a factor of $\sim 10^{4}$ in intensity loss.

In this study high quality electrostatic optics (courtesy of Elektros, Inc.) were used. Two deflection systems have been used.

A double-deflection beam deflector was designed and placed in between the two lenses along with a beam steering device for fine alignment purposes and later a single deflection system was placed after the final lens. The source is described in detail below.

The beam is scanned in a raster pattern across a specimen by the beam deflector which is energized by the deflection voltages from a scan generator. The secondary electron signal produced in the specimen is amplified with a continuous dynode (channeltron) detector. This signal modulates the intensity of a long-persistence CRT driven along the X-Y axes by the scan generator. The images are similar in appearance to those of an SEM (see Experimental Results).

REFERENCES

1. H. Liebl, J. Phys. E, 8 (1975).

2. F. W. Karasek, Research and Development (October 1974) 48.

3. C. E. Hall, "Introduction to Electron Microscopy," (McGraw-Hill Co., (1966) Ch. 7).

4. A. V. Crewe, Science 168 (1970) 1338.

5. Premierè Conférence Internationale Sur Les Source D'ions, Saday, France, 1969.

6. A. R. Hill, Nature 218 (1968) 292.

7. J. C. Wiesner, Report No. ERL-70-6, College of Engineering, University of California at Berkeley, 1970.

8. R. G. Wilson and G. R. Brewer, "Ion Beams" (J. Wiley and Sons, 1973).

9. E. W. Müller and T. S. Tsong, J. Chem. Phys. 41 (1964) 3279.

10. C. A. Evans and C. D. Hendricks, Rev. Sci. Inst. 43 (1972) 1527.

11. R. L. Seliger and J. W. Ward, J. Vac. Sci. and Tech. 12 (1975).

12. R. Levi-Setti, Proceedings of the 1974 Scanning Electron Microscopy Symposium, ITTRI.

II. REVIEW OF THE BASICS OF ELECTRON OPTICS

A. Introduction

The purpose of this section is to acquaint the reader with some of the fundamentals of electron optics and to explain the close analogy between geometrical optics and the focussing of beams of charged particles by electric fields. The case of focussing by magnetic fields, although more important for electron microscopy will not be considered here. Electron optics, now perhaps more appropriately called charged particle optics, consists primarily of the determination of the trajectories of particles in electric and magnetic fields and the way in which the fields can be produced so that the trajectories have certain desirable properties. The usual results one aims at are to produce highly focussed beams of particles or faithful point to point imaging of some small object.

Because electron optics deals with objects of atomic size the question immediately arises as to whether a quantum mechanical description of their motion is necessary. It turns out that the classical description is almost always valid. The classical description is the short wavelength limit of the quantum mechanical description which in turn, is formally the same as the short wavelength representation of light optics, called geometrical optics. This is why the dynamics of charged particles is called electron optics. The nomenclature of geometrical optics can be taken over virtually

intact to electron optics. For example:[1] light flux $\longleftrightarrow$ current; emittance $\longleftrightarrow$ current density; luminous intensity $\longleftrightarrow$ current per solid angle; surface brightness $\longleftrightarrow$ electron optical brightness ($\longleftrightarrow$ = "corresponds to").

The reason the classical description of the motion can be used is that almost everywhere the beam of particles encounters the optical system on a macroscopic basis. The dimensions of the system are >> the de Broglie wavelength of the particle ($\lambda = \frac{h}{p} \approx \frac{12 \times 10^{-8} \text{ cm}}{\sqrt{V}}$ for electrons and $\approx \frac{0.3 \times 10^{-8} \text{ cm}}{\sqrt{V}}$ for protons, where eV is the kinetic energy of the particle in electron volts).

The wave aspect of the particles becomes important at limiting apertures where diffraction effects can be introduced, at the surfaces of field emitters and in beam-specimen interactions (Fresnel fringes around holes in thin films which can be seen in a transmission electron microscope are a good example of the latter effect).

Consider now the short wavelength limit of the Schrödinger equation

$$\frac{-\hbar^2}{2m} \nabla^2 \psi + V\psi = i\hbar \frac{\partial \psi}{\partial t} \tag{1}$$

Writing the wave function ψ as[2]

$$\psi(\vec{r}) = A(\vec{r},t) \exp\left(\frac{i}{\hbar} S(\vec{r},t)\right) \tag{2}$$

the Schrödinger equation separates into two equations when the real and imaginary components are equated:

$$\frac{\partial S}{\partial t} + \frac{(\vec{\nabla}S)^2}{2m} + V = \frac{\hbar^2}{2m}\frac{\nabla^2 A}{A} \tag{3}$$

$$m\frac{\partial A}{\partial t} + \vec{\nabla}A \cdot \vec{\nabla}S + \frac{A}{2}\nabla^2 S = 0 \tag{4}$$

In the short wavelength, or classical approximation, $\hbar$ is set equal to zero and Eq. (3) becomes

$$\frac{\partial S}{\partial t} + \frac{(\vec{\nabla}S)^2}{2m} + V = 0 \tag{5}$$

Eq. (5) is the Hamilton-Jacobi equation[3] with S the Hamilton's principal function. If the Hamiltonian is time independent, $S = S(r, \frac{\partial S}{\partial r}, t) = W(r, \frac{\partial S}{\partial r}) - Et$. Then $\frac{\partial S}{\partial t} = -E$ and the equation of motion is

$$(\vec{\nabla}W)^2 = 2m(E-V). \tag{6}$$

Eq. (4) is the equation of continuity for the probability density -- let $\vec{J} \equiv R_e(\psi^* \frac{\hbar}{im}\vec{\nabla}\psi)$ be the probability current and $P \equiv |\psi|^2$ be the probability density. Then from Eq. (2), $J = Re(A\exp(-\frac{i}{\hbar}S)\frac{\hbar}{im}\exp(\frac{i}{\hbar}S)(\vec{\nabla}A + \frac{i}{\hbar}A\vec{\nabla}S)) = \frac{A^2\vec{\nabla}S}{m}$ and Eq. (4) becomes $\vec{\nabla}\cdot\vec{J} + \frac{\partial P}{\partial t} = 0$.

When the wave properties of the particles can be ignored (i.e., when we may consider $\hbar = 0$) then their paths can be calculated by using Eq. (5), or by using Lagrange's or Newton's equations, which are more convenient. We will now see why these are formally identical with geometrical optics.

The laws governing the propagation of a light beam in a non-conducting medium are Maxwell's equations

$$\vec{\nabla} \cdot \epsilon\vec{E} = 0 \tag{7a}$$

$$\vec{\nabla} \cdot (\mu\vec{H}) = 0 \tag{7b}$$

$$\vec{\nabla} \times \vec{E} = -\mu \frac{\partial \vec{H}}{\partial t} \tag{7c}$$

$$\vec{\nabla} \times \vec{H} = \epsilon \frac{\partial \vec{E}}{\partial t} \tag{7d}$$

Defining the index of refraction as $n(\vec{r}) = \frac{v}{c} = \sqrt{\frac{\epsilon_o \mu_o}{\epsilon \mu}}$ the solutions to Eqs. (7) can be written as[4] $\vec{E}(\vec{r},t) = \vec{e}(\vec{r}) \exp i(K_o L(\vec{r}) - \omega t)$, $\vec{H}(\vec{r},t) = \vec{h}(\vec{r}) \exp i(K_o L(\vec{r}) - \omega t)$ where $K_o = \frac{\omega}{c}$ and $L(\vec{r})$ is the optical path of the light. $\vec{e}$ and $\vec{h}$ are complex functions of position. Inserting these solutions into Eqs. (7) one obtains

$$\vec{\nabla}L \times \vec{h} + \epsilon c\vec{e} = -\frac{1}{iK_o} \vec{\nabla} \times \vec{h} \tag{8a}$$

$$\vec{\nabla}L \times \vec{e} - \mu c\vec{h} = -\frac{1}{iK_o} \vec{\nabla} \times \vec{e} \tag{8b}$$

$$\vec{e} \cdot \vec{\nabla}L = -\frac{1}{iK_o} (\vec{e} \cdot \vec{\nabla} (\log \epsilon) + \vec{\nabla} \cdot \vec{e}) \tag{8c}$$

$$\vec{h} \cdot \vec{\nabla}L = -\frac{1}{iK_o} (\vec{h} \cdot \vec{\nabla} (\log \mu) + \vec{\nabla} \cdot \vec{h}) \tag{8d}$$

In the approximation of geometrical optics the wavelength $\lambda \to 0$, $K_o \to \infty$ and Eqs. (8) reduce to

$$\vec{\nabla}L \times \vec{h} + \epsilon c\vec{e} = 0 \tag{9a}$$

$$\vec{\nabla}L \times \vec{e} - \mu c\vec{h} = 0 \tag{9b}$$

$$\vec{e} \cdot \vec{\nabla}L = 0 \tag{9c}$$

$$\vec{h} \cdot \vec{\nabla} L = 0 \tag{9d}$$

Substituting Eq. (9b) $\vec{h} = \frac{\vec{\nabla} L \times \vec{e}}{\mu c}$, into equation (9a)

$$\vec{\nabla} L \times (\vec{\nabla} L \times \vec{e}) + \mu \epsilon c^2 \vec{e} = 0$$

or

$$\frac{\mu \epsilon}{\mu_o \epsilon_o} \vec{e} = \vec{\nabla} L \times (\vec{e} \times \vec{\nabla} L)$$

which with the vector identity $\vec{A} \times (\vec{B} \times \vec{C}) = (\vec{A} \cdot \vec{C})\vec{B} - (\vec{B} \cdot \vec{C})\vec{A}$, and Eq. (9c) leaves us with

$$(\vec{\nabla} L)^2 \vec{e} = \frac{\epsilon \mu}{\epsilon_o \mu_o} e = n^2(\vec{r})\vec{e}$$

or

$$(\vec{\nabla} L)^2 = n^2(\vec{r}) \tag{10}$$

Eq. (10) is the eikonal equation of geometrical optics, which describes the variation in optical path as a function of index of refraction. Consider as an example the case of a light ray traveling in the Z-direction through a medium where n = const.

$\left(\frac{\partial L}{\partial Z}\right)^2 = n^2$, $\frac{\partial L}{\partial Z} = \pm n$, $L = \pm n\ Z$ + constant and $\vec{E}(\vec{r},t)$

$= \vec{e}\ e^{i(\pm n K_o Z - \omega t)}$, ignoring the constant of integration which merely introduces a constant phase factor. $L(\vec{r})$ is the equation of the wave-front of constant phase of the light beam, and the beam is perpendicular to surfaces of constant L. Eq. (10) is formally identical with Eq. (6) if we identify L with W and n with $\sqrt{2m(E - V)}$, so that light rays in the approximation of geometrical optics obey the same equation of motion as particles in Hamiltonian mechanics.

The most common electron optical instruments are microscopes and probes (oscilloscopes fall into the latter classification). The beams of charged particles either carry information about a specimen for display as an image or for energy analysis, or they are brought to a focus and scanned across a specimen in order to generate information about its morphology, chemical composition, etc.

This study is concerned with the latter type of application of electron optics, and the following discussion is oriented towards it.

In practice the electron optical problem of producing fine focus beams is approached either by parameterizing the optical elements in terms of focal lengths, aberration coefficients, etc. and then using standard geometrical optics, or by ray tracing procedures involving self-consistent calculations of the fields in the optical elements and the solutions to Newton's equations for the motion of particles in these fields. The methods used in this study were the former, although considerable use was made of ray tracing calculations[7] for electrons in a field emitter diode.

This study involved the application of symmetric, electrostatic lenses for the formation of highly focussed beams. Therefore the description of electron lenses will be formulated using these for reference.

B. Derivation of Lens Equations

Lenses can be understood most easily in terms of a (hypothetical) ideal lens. The ideal lens was described by Maxwell[5] and the three conditions it must meet are paraphrased below:

1. Every ray leaving a single object point must, after passing through the lens converge to or diverge from a single image point;
2. If the object is a plane perpendicular to the lens axis the image must also be a plane perpendicular to the lens axis;
3. The image of the object must be similar to the object.

Image, object and axis are shown in Fig. 1.

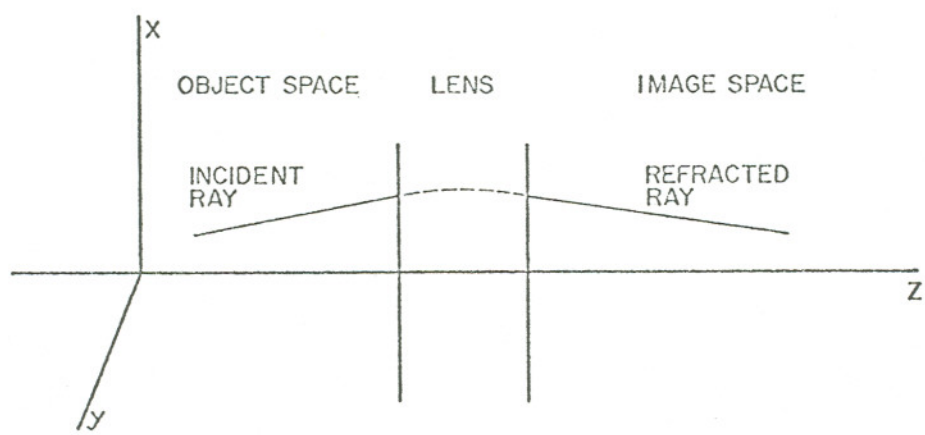

Fig. 1

Optical nomenclature. Z-axis is the optical axis.

It can be shown (see for example, Born and Wolfe, Principles of Optics, pages 132-146) that perfect imaging from a three-dimensional object space into a three-dimensional image space in accord with Maxwell's conditions is a projective transformation. Real lenses, while not perfect, can be approximated by assuming they perform projective transformations.

A projective transformation images lines into lines and is described[4] by

$$x_i = \frac{F_1}{F_0}, \quad y_i = \frac{F_2}{F_0}, \quad z_i = \frac{F_3}{F_0} \tag{11}$$

where x_i, y_i, z_i are the image coordinates and x_o, y_o, z_o are the object coordinates and

$$F_n = a_n x_o + b_n y_o + c_n z_o + d_n, \quad n = 0, 1, 2, 3.$$

F_n is the equation of a plane in the object coordinates x_o, y_o and z_o. The inverse transformation is given by $x_o = \frac{F'_1}{F'_0}$ etc. with $F'_m = a'_m x_i + b'_m y_i + c'_m z_i + d'_m$, $m = 0, 1, 2, 3$, as before.

If $F_0 = 0$, the image of a point in the plane defined by F_0 lies at infinity. Similarly, the object whose image appears in the plane $F'_0 = 0$ lies at $-\infty$. The planes F_0 and F'_0 are called the principal focal planes and the points in the planes lying on the z axis ($x_o = x_i = y_o = y_i = 0$) are called the focal points of the lens in object space and image space, respectively.

Since we are concerned with rotationally symmetrical lenses we can consider rays from points in just one plane. We choose the plane

to be the x - z plane. Then from Eq. (11)

$$x_i = \frac{a_1 x_o + c_1 z_o + d_1}{a_0 x_o + c_0 z_o + d_0} \tag{12a}$$

$$z_i = \frac{a_3 x_o + c_3 z_o + d_3}{a_0 x_o + c_0 z_o + d_0} \tag{12b}$$

By the summetry of the lens if x_o is changed to $-x_o$, z_i should be unchanged implying $a_0 = a_3 = 0$. Also, when $x_o \to -x_o$, x_i should $\to -x_i$ so that $c_1 = d_1 = 0$ and Eqns. (12) reduce to

$$x_i = \frac{a_1 x_o}{c_0 z_o + d_0} \tag{13a}$$

$$z_i = \frac{c_3 z_o}{c_0 z_o + d_0} \tag{13b}$$

If the object is at the focal point in object space z_i is infinite so the equation for F_o is $c_0 z_o + d_0 = 0$, from Eqn. (13b). This is the equation of a plane intersecting the z axis at $-\frac{d_0}{c_0}$ and perpendicular to it. If Eqns. (13) are solved for x_o and z_o

$$x_o = \frac{c_0 d_3 - c_3 d_0}{a_1 (c_0 z_i - c_3)} \tag{14a}$$

$$z_o = \frac{d_3 - d_0 z_i}{c_0 z_i - c_3} \tag{14b}$$

Eqn. (14b) defines the position of the focal plane in image space:

$$c_0 z_i - c_3 = 0 \text{ or } z_i = \frac{c_3}{c_0}$$

Let axial distances to objects and images be measured from the object and image space focal points, respectively. We define

$c_0 z_o + d_0 = c_0 z$, $c_0 z_i - c_3 = c_0 z'$, $x = x_o$ and $x' = x_i$. Then Eqns. (13) become

$$x' = \frac{a_1 x}{c_0 z} \quad \text{and} \quad z' = \frac{c_0 d_3 - c_3 d_0}{c_0{}^2 z}$$

By setting $\frac{a_1}{c_0} = f$ and $\frac{c_1 d_3 - c_3 d_0}{a_1 c_0} = f'$ we can further simplify Eqns. (13) to $x' = \frac{fx}{z}$, $z' = \frac{f'a}{c_0 z} = \frac{f'f}{z}$ (f is called the focal length of the lens). From these equations we see

$$\frac{x'}{x} = \frac{f}{z} = \frac{z'}{f'} \quad \text{or} \quad zz' = ff' \tag{15}$$

(Newton's equation). The relationship of these variables can be seen in Fig. 2.

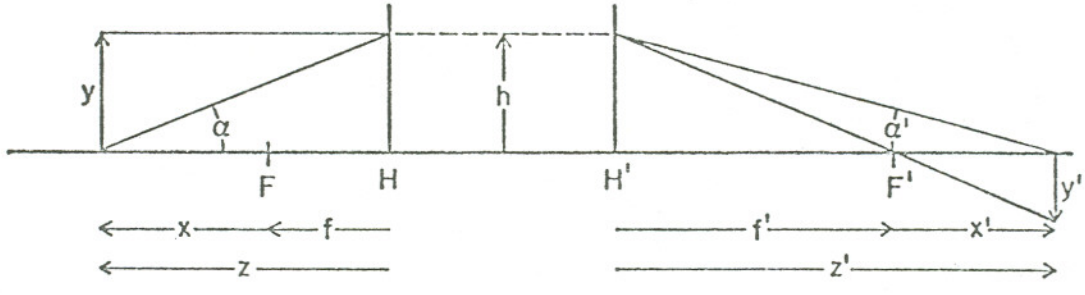

Fig. 2

The variables used for elementary lens calculations. F and F' are the object side and image side focal points, H and H' the principal planes in object and image space, respectively. x and x' denote object and image positions with respect to the focal planes in object and image space.

The magnification of the lens is defined as $M = \frac{x'}{x} = \frac{f}{z} = \frac{z'}{f'}$. M is independent of y and y' so the shape of an object in a plane perpendicular to the z axis is unchanged. M = 1 when z = f and z' = f'. The planes perpendicular to the z axis at these points are called the principal planes of the lens and are denoted by H and H' respectively.

The two focal planes and principal planes are called the cardinal planes of the lens. The points where they intersect the axis are cardinal points. There are two other cardinal points (and planes) - the nodal points.

A ray leaving the axis with angle α intersects the first principal plane at a height h and is imaged with unit magnification into the second principal plane at height h. The ray in image space intersects the axis at an angle α'. From Fig. 2, $\tan \alpha = \frac{h}{f - z}$ (z is the negative direction) and $\tan \alpha' = \frac{h}{z' - f'}$ (negative angle). The angular magnification is defined as

$$m = \frac{\tan \alpha'}{\tan \alpha} = \frac{f - z}{z' - f'} = \frac{z}{f'} = \frac{f}{z'} .$$

When $z = f'$ and $z' = f$, m = 1. These values of z and z' define the nodal points. Conjugate rays passing through the nodal points are parallel to each other.

When the principal points of a lens are specified, everything about the lens is known within the limits of validity of geometrical optics (excluding aberrations - we are considering an ideal lens).

An interesting property of electron lenses is that the principal planes are crossed, as opposed to light optical lenses. The paths of the virtual rays (extended from the red rays in field free space) are shown in Fig. 3 for object and image on the optical lens.

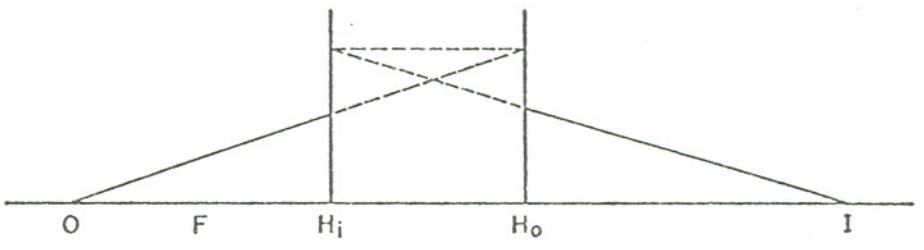

Fig. 3

The crossing of the principal planes for an electron lens.

No lens is ideal, although modern lenses for light are extremely good. Electron lenses, by contrast, are very poor. A good light microscope is capable of resolving detail ~ the wavelength of light used to illuminate the object. The best electron microscopes can resolve detail ~ 3 Å, which is ≈ 60 times the de Broglie wavelength of a 50 kV electron - a typical energy for an electron microscope.

Electron lenses are capable of forming excellent images or extremely well focussed beams, but only if the paths of the charged

particles lie very close to the optical axis and make small angles with respect to it ($\lesssim 0.05$ rad).

C. Derivation of Equations of Motion for Electrostatic Lenses

As demonstrated above, charged particles obey the equations of geometrical optics, so we may use the terminology and concepts of geometrical optics to describe electron optics. At this point, it seems worthwhile to show how symmetric fields can actually act like a lens in order to better visualize how an electron lens works, which isn't obvious from the formal identity.

Let us now consider the solution to the equations of motion of a charged particle passing through a symmetric (and rotationally symmetric) electrostatic lens.

First, the physical reason electrostatic lenses are used for ions can be seen by writing down the Lorentz equation $\vec{F} = e(\vec{E} + \vec{v} \times \vec{B})$. $|\vec{v}| = \left(\frac{2e\ V_{acc}}{m}\right)^{\frac{1}{2}}$ (V_{acc} is the accelerating voltage). For a given V_{acc} a magnetic lens will need to be stronger by a factor $\left(\frac{m_{ion}}{m_{elect}}\right)^{\frac{1}{2}}$ for ions than for electrons. This can be seen as follows: to deflect a beam of particles through some angle θ corresponding to a radius of curvature ρ the magnetic field must exert a force evB equal to the particle's mass times its acceleration $\frac{V^2}{\rho}$, so that $B = \frac{m}{e}\frac{v}{\rho}$.

The electric field must exert a force eE so that $E = \frac{m}{e}\frac{v^2}{\rho}$. With $\frac{1}{2} m v^2 = e V_{acc}$ the ratio of B to E is $\left(\frac{m}{2eV_{acc}}\right)^{\frac{1}{2}}$, and so the ratio of B to E for particles with mass M and m respectively and with the same energy $e V_{acc}$ is $\left(\frac{M}{m}\right)^{\frac{1}{2}}$. This factor amounts to 43 for protons and 500 for Xe ions. Even though magnetic lenses have significantly better aberration coefficients than electrostatic lenses for a given focal length they would have to be very large and powerful to focus ion beams. The electrostatic lenses used in this study are small (5 cm diameter) and extremely simple to operate.

The experimental setup in this study had approximately the potential energy diagram shown in Fig. 4, ignoring the beam deflectors.

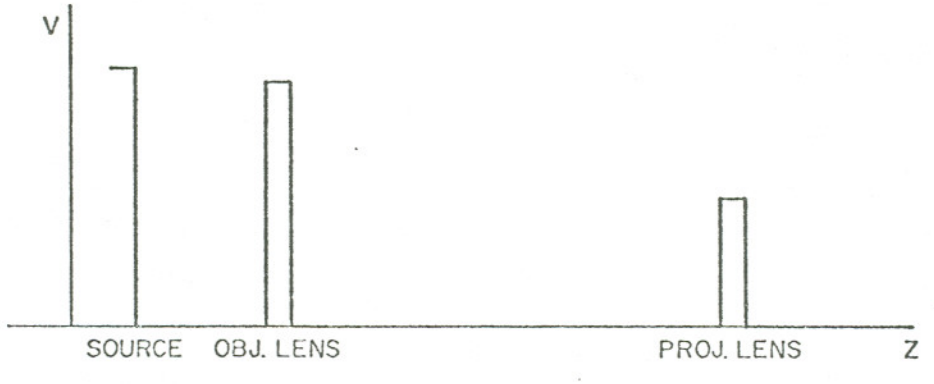

Fig. 4

Schematic potential energy diagram of the SIM.

Before going on, it is of considerable interest to estimate the speed of a particle as it passes through the center of a lens. The lenses consist of three elements. The outer apertures are at ground potential and the inner one is near the accelerating potential. Approximate the lens by an infinite conducting plane with an aperture of radius a. Assume the particle moves along the Z axis which passes through the center of the aperture. The field due to the plane is given by[7]

$$F(z) = F_o \left(1 + \frac{2}{\pi}\left(\tan^{-1}\left(\frac{a}{z}\right) - \frac{az}{a^2 + z^2}\right)\right) \tag{20}$$

for $z \leq 0$. F_o is the field due to a plane without an aperture. $F(z) \to F_o$ as $z \to -\infty$.

We imagine the particle starting at $-z_o$, moving to the right with initial energy $\frac{1}{2}mv_o^2 = eF(z_o)z_o$. In the absence of the aperture the particle would reach the plane with zero kinetic energy. With the aperture,

$$\frac{1}{2} mv^2(z = 0) = \frac{1}{2} m v_o^2 - e \int_{-z_o}^{o} F(z)dz$$

$$= eF(z_o')z_o - eF_o \int_{-z_o}^{o} \left(1 + \frac{2}{\pi}\left(\tan^{-1}\left(\frac{a}{z}\right) - \frac{az}{a^2 + z^2}\right)\right) dz$$

$$= \frac{2eF_o z_o}{\pi} \tan^{-1}\left(\frac{a}{z_o}\right)$$

In a real lens, the particle would enter the lens aperture on the axis and suddenly encounter a field crudely approximated by Eqn. (20). Very little field extends beyond the entrance aperture. A typical value of $\frac{a}{z_o}$ would be 0.5, where z_o is the separation of the electrodes. Then $\frac{1}{2}\,mv^2\ (z = 0) = 0.29 \times \frac{1}{2}\,m\,v_o^{\,2}$ and $v(z = 0) = 0.54\ v_o$. Thus even if the center electrode of the lens is at gun potential the particle retains half of its initial speed and one quarter its initial energy, i.e., the potential at the center of the electrode is $\approx \frac{3}{4}$ that of the initial energy of the particle.

In the non-relativistic limit ($mc^2 \approx 935$ Mev for protons) the Lagrangian is $L = T - V = \frac{1}{2}\,mv^2 - e\Phi$. Φ is determined by the field distribution along the optical path and is zero except in the gun and lenses. v is the velocity and $|\vec{v}| = \left(\frac{2eV_{acc}}{m}\right)^{\frac{1}{2}}$ except in the lenses. Since the lenses are symmetrical the particles have the same speed upon leaving as entering. The potential in space is determined by the solution to Laplace's equation $\nabla^2\Phi = 0$, in the approximation where the field created by the beam of charged particles can be ignored.

If a lens is rotationally symmetric and we consider only meridional rays, then by the procedure detailed in Appendix 1 it is possible in a straightforward way to derive the differential equation of a charged particle as it passes through the lens. The equation in the Gaussian approximation (trajectories very near the optical axis and always making small angles with the axis), is

$$\frac{d^2r}{dz^2} + \frac{1}{2\phi}\frac{d\phi}{dz}\frac{dr}{dz} + \frac{1}{4\phi}\frac{d^2\phi}{dz^2}\,r = 0 \qquad (21)$$

where $\phi = \phi(r,z)$ and the z-axis coincides with the optical axis (axis of rotational symmetry of the lens). This is a linear, homogeneous second-order differential equation, which implies a number of important facts. In order to more easily visualize the solutions to (21), let us suppose that the paths of the charged particles lie in the x-z plane. We then consider the nature of the solutions to

$$\frac{d^2x}{dz^2} + P(z)\frac{dx}{dz} + Q(z) = 0 \qquad (22)$$

Suppose two independent solutions of (22) are x_1 and x_2. The Wronskian of x_1 and x_2 is $W(z) = x_1\frac{dx_2}{dz} - \frac{dx_1}{dz}x_2$ and this is equal to[8] $A \exp(-\int P(z)\,dz)$, where A is a constant.

$x_1(z) = 1$, $x_2(z') = 1$, then clearly $\frac{dx_1(z)}{dz} = 0$, $\frac{dx_2(z')}{dz} = 0$, $\frac{dx_1(z')}{dz} = -\frac{1}{f'}$ and $\frac{dx_2(z)}{dz} = \frac{1}{f}$. $W(z) = \frac{1}{f}$, $W(z') = \frac{1}{f'}$. Since $P(z) = \frac{1}{2\phi}\frac{d\phi}{dz}$, $W(z) = \exp(-\int P(z)\,dz) = \exp(-\frac{1}{2}\int \phi^{-1}\,d\phi = \text{const.} \times \phi^{-1/2}$ then we have

$$\frac{1}{f} = \text{const.} \times \phi^{-1/2}\,(z)$$

$$\frac{1}{f'} = \text{const.} \times \phi^{-1/2}\,(z), \text{ resulting in}$$

$$\frac{f'}{f} = \left(\frac{\phi(z')}{\phi(z)}\right)^{1/2} \qquad (23)$$

Since for a unipotential lens $\phi(z) = \phi(z')$, $f' = f$.

It is possible to show that Eqn. (22) implies lens action and that the lens is always a positive lens, that is, the action of the lens is always such as to cause the trajectories of the particles to converge towards the axis. If the appropriate linear combinations of solutions to (22) are chosen one has $x_1(z) = 1$, $\frac{dx_1(z)}{dz} = 0$ and $x_2(z) = 0$, $\frac{dx_2(z)}{dz} = 1$. These solutions represent two rays at z, one at unit distance with zero slope, the other passing through the axis at z with unit slope. The trajectories of the rays are determined by

$$x(z) = Ax_1(z) + Bx_2(z) = h \tag{23a}$$

$$\frac{dx(z)}{dz} = A\frac{dx_1(z)}{dz} + B\frac{dx_2(z)}{dz} = \alpha \tag{23b}$$

where h is the distance of the trajectory from the axis at z and α is the slope. Evidently $Ax_1(z) = h$. On the image space side of the lens both trajectories cross the axis (for simplicity it is assumed a real image is formed). At the point where $x_2(z') = 0$ the ratio of $x(z')$ to $x(z)$ is $\frac{x_1(z')}{x_1(z)} = x_1(z') = M$, the magnification. $M = M(z,z')$.

In order that $x_2(z') = 0$ the trajectory must curve towards the axis. That this is indeed the case can be demonstrated[9] by letting $X = x\phi^{1/4}$. With this substitution the paraxial ray equation (22) becomes

$$X'' + \frac{3}{16}\left(\frac{\phi'}{\phi}\right)^2 X = 0. \tag{24}$$

The second derivative of X is always opposite in sign from X, so X always curves towards the axis. Outside the lens, where ϕ = constant the particle trajectories are straight lines: $\phi' = 0$

so $X'' = 0$, $X = C_1 z + C_2$ and $x = c_1' z + c_2'$. In the lens where $\phi \neq$ const. the trajectory curves toward the axis because of Eqn. (24). Then X crosses the axis either in the lens or X will be represented by a straight line intersecting the axis outside the lens. In either case X outside the lens where ϕ = const., will make a less acute angle with respect to the axis. Since x is proportional to X when ϕ = const. the actual path of the ray will also be at a less acute angle to the axis, i.e. the path is curved towards the axis by the lens. If the trajectory was initially at such an angle that the lens is unable to curve it sufficiently to pass through the axis in image space a virtual image will be formed in object space, with the trajectories appearing to diverge from it. The lens action of an arbitrary potential which is rotationally symmetric about the axis has thus been demonstrated by Newton's laws as well as by symmetry.

D. Aberrations

So far we have discussed ideal lenses. Real lenses never form perfect images of arbitrary objects because of the inability of any lens to transform an incoming family of rays on a positive spherical wavefront into an outgoing family on a negative spherical wavefront (see Fig. 5).

It is clearly necessary that such a transformation take place if a point object P is to be imaged as a point P' and since an arbitrary object is composed of a large (infinite) number of points, a perfect image will be formed only if that transformation is possible.

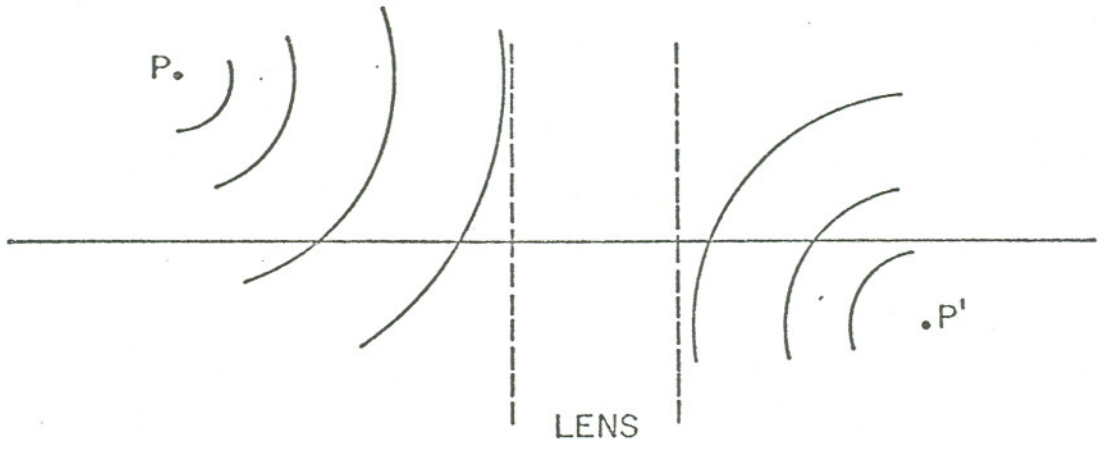

Fig. 5

Action of an Aberrationless Lens

It is clearly necessary that such a transformation take place if a point object P is to be imaged as a point P' and since an arbitrary object is composed of a large (infinite) number of points, a perfect image will be formed only if that transformation is possible. The deviation of the performance of a real lens from that of an ideal lens is described in terms of aberrations (from the Latin aberrare, to deviate).

There are two kinds of aberrations: geometrical, which are a function of the shape of the lens, and electronic, which are a function of the charge and speed of the particles. First we consider the geometrical aberrations.

The effect of aberrations is to displace an image point from its ideal gaussian position. This displacement can be characterized[4]

by a change in optical path length using the eikonal equation (Eq. 10). The function L can be expanded in terms of the co-ordinates of object and image and then used to determine the displacement. The mathematics of this is somewhat involved, and reference should be made to Born and Wolfe[4] or Zworykin et al[6] for the details. The result of such a computation is that the deviation of the image point from the ideal gaussian position can be expressd to third order in the expansion in terms of five so-called aber-ration coefficients (for magnetic lenses there are three additional terms arising from rotation of the beam). The coefficients are called the Seidel coefficients and were first worked out in the 19th century for light optics. If we denote the coordinates of the exit aperture of the lens (which may be in field free space) by x_a, y_a and the coordinates of the object by x, y then the displacements $\Delta x'$ and $\Delta y'$ in the image plane (for unit magnification) are given by

$$\Delta x' = S_1 \times (x^2 + y^2) + S_2\, r_a \cos\theta\, (x^2 + y^2) + S_3 r_a ((x^2 - y^2)\cos\theta + 2xy \sin\theta) + S_4\, r_a^2\, ((1 + 2\cos^2\theta)x + 2y \cos\theta \sin\theta) + S_5\, r_a^3 \cos\theta \qquad (25a)$$

$$\Delta y' = S_1\, y(x^2 + y^2) + S_2\, r_a \sin\theta\, (x^2 + y^2) + S_3\, r_a\, (-(x^2 - y^2)\sin\theta + 2x\, y \cos\theta) + S_4\, r_a^2\, ((1 + 2\sin^2\theta)y + 2x \cos\theta \sin\theta) + S_5 r_a^3 \sin\theta \qquad (25b)$$

where $x_a = r_a \cos\theta$, $y_a = r_a \sin\theta$. The notation is illustrated in Fig. 6.

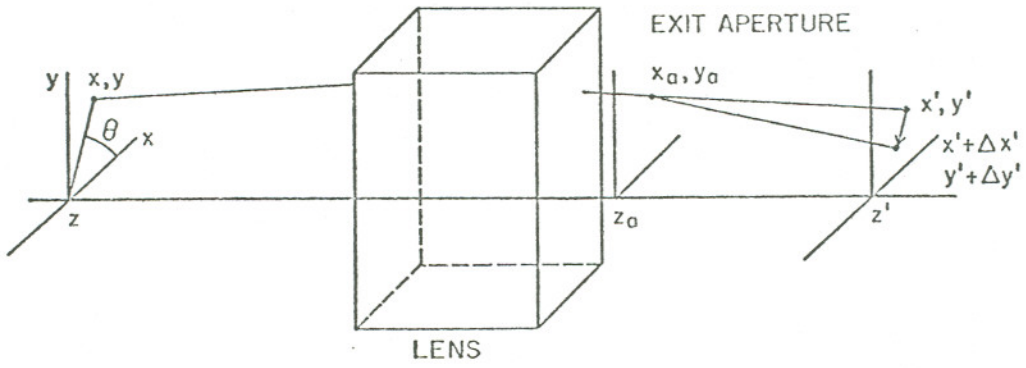

Fig. 6

Deviation $\Delta x'$, $\Delta y'$ from perfect imaging caused by lens aberrations.

It is easier to interpret the meaning of the coefficients $S_1 \ldots S_5$ by considering them one at a time, assuming all are zero except the one of interest.

S_1: Suppose $x = 0$. Then $\Delta y' = S_1 y^3$. Similarly, if $y = 0$, $\Delta x' = S_1 y^3$. The image point is displaced by an amount proportional to the cube of the distance of the object point from the axis. This results in a distortion of the image and S_1 is the distortion coefficient. It may be negative or positive.

S_2: If $x = 0$, $\Delta y' = S_2 r_a \sin\theta\, y^2$, $\Delta x' = S_2 r_a \cos\theta\, y^2$. This results in curvature of field - the image plane becomes a curved surface, as can be seen in Fig. 7.

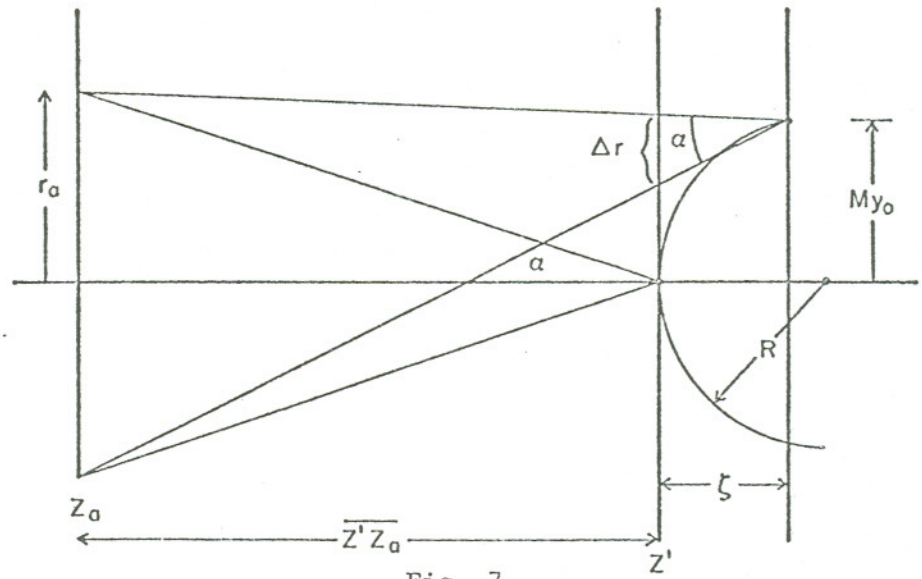

Fig. 7

Curvature of field (greatly exaggerated).

Points on the axis are imaged on the axis at z. Tan $\alpha = \frac{r_a}{\overline{zz_a}}$ so the object point at y is imaged into a circle of radius $\Delta r' = S_2 y^2 r_a$ in the image plane, at a height My where M is the magnification of the lens. These rays then converge to an image point a distance ζ behind (if $S_2 > 0$) or in front (if $S_2 < 0$) of the image plane. The radius R of the surface is given by $R^2 = M^2y^2 + (R - \zeta)^2$, and $R \approx \frac{M^2y^2}{2\zeta}$ if $\zeta << R$ (the figure is greatly exaggerated). Since $\zeta = \frac{S_2 y^2 r_a}{\tan \alpha} \approx S_2 y^2 \overline{zz_a}$, $R \approx \frac{M^2y^2}{2S_2y^2\overline{zz_a}}$. A sharp image appears on a curved surface. This can be a noticeable effect in a transmission electron microscope at very low magnification.

S_3: $x = 0$, $\Delta x' = -S_3 y^2 r_a \cos\theta$, $\Delta y' = S_3 y^2 r_a \sin\theta$. This aberration is 3rd order astigmatism - a point is imaged to two lines separated along the z axis. At the image plane the rays from the object point at y form a circle of radius $\Delta r' = S_3 y^2 r_a$. The effect is due to the minus sign in the equation for $\Delta x'$, as shown in Fig. 8. The displacement in the x direction is negative (at the image plane), hence the rays must cross over before reaching the gaussian image

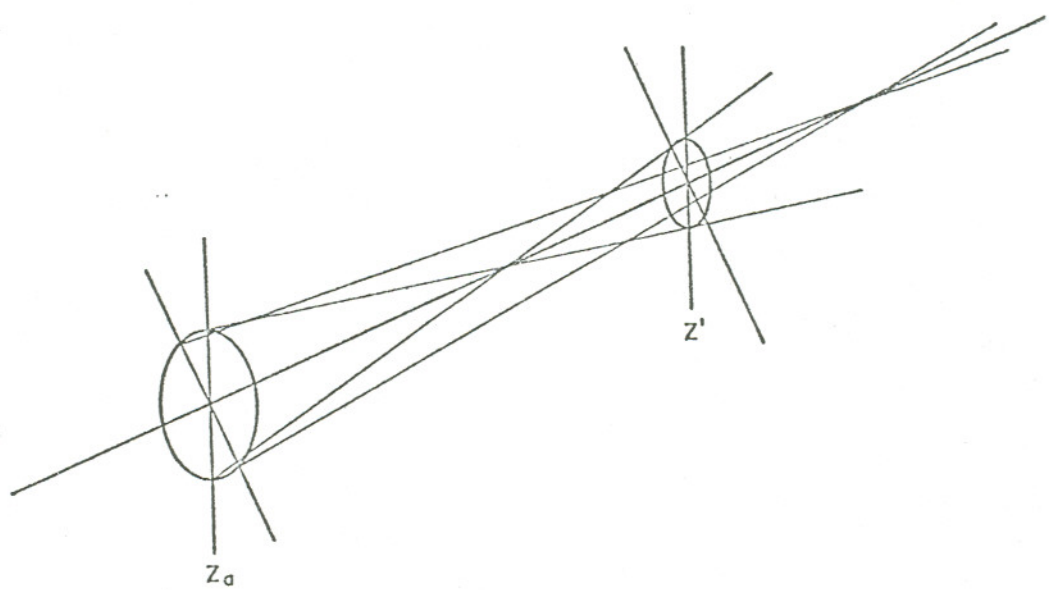

Fig. 8

Third Order Astigmatism

plane. If the sign of S_3 is reversed, the effect is the same except now the meridional rays (the ones in the y - z plane) will come to a focus ahead of the gaussian image plane. The displacement in the

y direction has the opposite sense from x, so the rays cross over behind (in front of) the image plane.

Of the many electron optical devices it is probably easiest to detect astigmatism in an oscilloscope. In the older instruments manufactured by Tektronix, Inc. there was a control to correct astigmatism in the cathode ray tube. When the control was varied the beam spot could be made to focus into a line at one extreme of the control range and, at the other extreme into a line at right angles to the first one. When the control was properly set the beam spot was circular.

In addition to third order astigmatism, there is first order astigmatism caused by a lack of symmetry in the optical system which can then offset on-axis objects for which $x_o = y_o = 0$, as well as off-axis objects. Lack of symmetry can be caused by contamination on parts of the optical system which "see" the beam of particles. Contaminants (dirt, diffusion pump oil, vaporized specimens, etc.) will deposit themselves in a generally non-symmetrical way and if they consist of non-conducting materials will charge electrically when struck by the beam. Conducting contaminants will alter the mechanical symmetry of optical components. Of course, it is not possible to machine any optical component with perfect symmetry so there will always be some first order astigmatism in any system, but this can be compensated by introducing an optical element consisting of six or eight plates

symmetrically surrounding the beam axis and electrically connected in pairs. By applying appropriate voltages to the plates the beam can be refocused in only one plane to correct the astigmatism. This device is called, naturally, a stigmator.

S_4: $x_o = 0$, $\Delta x = 2S_4 r_a^2 y_o \cos\theta \sin\theta = S_4 r_a^2 y_o \sin 2\theta$

$\Delta y = S_4 r_a^2 y_o (1 + 2\sin^2\theta) = S_4 r_a^2 y_o (2 - \cos 2\theta)$. If r_a is fixed, $(\Delta x)^2 + (\Delta y)^2 = S_4^2 r_a^4 y_o^2 [5 - 4\cos 2\theta]$ which is the equation of a circle of radius $\Delta r = S_4 r_a^2 y_o$ with its center a distance $2\Delta r$ from the gaussian image point in the + y direction. The circles are tangent to a cone of half angle $\phi = \sin^{-1}\left(\frac{R}{2R}\right) = 30°$ (see Fig. 9).

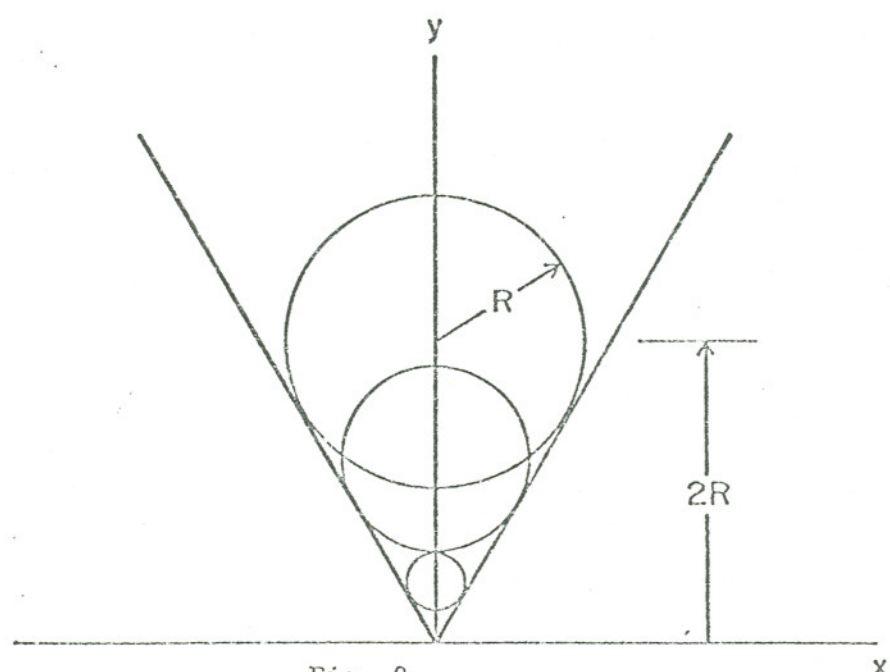

Fig. 9

The Effect of Coma

This aberration is called coma.

The name derives from the appearance of a point whose image is spoiled by this aberration - as Δy increases the radiation from the object point is spread over a larger area so the density per cm^2 decreases. The image then appears fainter the further it is from the gaussian image point and looks like a comet with a bright head and faint tail.

S_5: $x_o = 0$, $y_o = 0$, $\Delta x = S_5 r_a^3 \cos\theta$, $\Delta y = S_5 r_a^3 \sin\theta$, $\Delta r = S_5 r_a^3$. This aberration depends only on the cube of the aperture radius and is called spherical aberration. Rays farther from the axis suffer greater deflection and are focussed closer to the lens than the gaussian image plane. $r_a \approx \alpha' \overline{z_a z'}$, so $\Delta r = S_5 (\overline{z_a z'})^3 \alpha'^3 = C_5 \alpha'^3$. Note that the longitudinal aberration ζ is $\zeta \approx \frac{\Delta r}{\alpha} = C_5 \alpha'^2$.

There is unfortunately some confusion about the terminology and notation describing spherical aberration. This problem will be addressed below.

Spherical aberration is usually the most important geometrical aberration in a well made electron optical system. It is easy[1] to show that the rays leaving the aperture form a "disc of least confusion," i.e. form a minimum beam diameter $r_{min} = \frac{1}{4} C_5 \alpha'^3$, a short distance in front of the gaussian image plane (see Appendix 2).

The spherical aberration coefficient C_s varies as the dimensions of the lens varies. For example, with unipotential lenses it was found that $\frac{C_s}{f} \approx \left(\frac{f}{R}\right)^2$ where R is the radius of the aperture of the central electrode.

E. Special Analysis of Spherical Aberration

At this point some caution is due regarding terminology. It is important to know whether the α in the formula for the spherical aberration refers to the object side or the image side. In the discussion above it referred to the image side, but usually one refers to the object side. The transformation is simple: $\alpha = M\alpha'$, where M is the magnification of the lens. Hence, if $\Delta r' = \frac{1}{4} MC_s\alpha^3$ it is also given by $\frac{1}{4} M^4 C_s \alpha'^3$. Another problem is that you must be sure of the magnification when looking up spherical aberration coefficients for lenses. C_s is a function of object distance and hence magnification.

Professor Gertrude Rempfer of Portland State University, suggests the following way of understanding this. If the disc of confusion on the image side of the lens has radius $\Delta r'$, define C_s' by $\Delta r' = C_s'\alpha'^3$ (see Fig. 10). Since $\Delta r'$ is already defined as $S_5 r_a^3$ and $r_a = \alpha' \overline{z_a z'}$ this gives us $C_s' \left(\frac{r_a}{\overline{z_a z'}}\right)^3 = S_5 r_a^3$ or $C_s' = S_5 \overline{(z_a z')}^3$. Thus C_s' as defined here depends on the magnification through the term $\overline{(z_a z')}^3$: $C_s' = C_s'(M)$. Similarly, in object space $\Delta r = C_s(M)\alpha^3$, $\alpha = M\alpha'$, $\Delta r = \frac{\Delta r'}{M}$ and $C_s\alpha^3 = \frac{\Delta r'}{M} = \frac{C_s'\alpha'^3}{M} = \frac{C_s'\alpha^3}{M^4}$

$C_s' = M^4 C_s$. People who work with transmission microscopes quote C_s for high magnifications - the object close to the lens focal point (the author is in this group). Those who work with probes sometimes quote C_s' for low magnification, where an object a long

way off is greatly demagnified on an image plane close to the lens. This can cause confusion.

The following analysis of spherical aberration is due to Professor Rempfer and has not been published. Because the principal planes of the lens are actually curved surfaces not only does the position of the focal point (g) along the axis change as the distance of the incoming ray from the axis varies, but the focal length f varies independently. Recall that f is defined as the distance from the principal plane, which is actually curved (see Fig. 10).

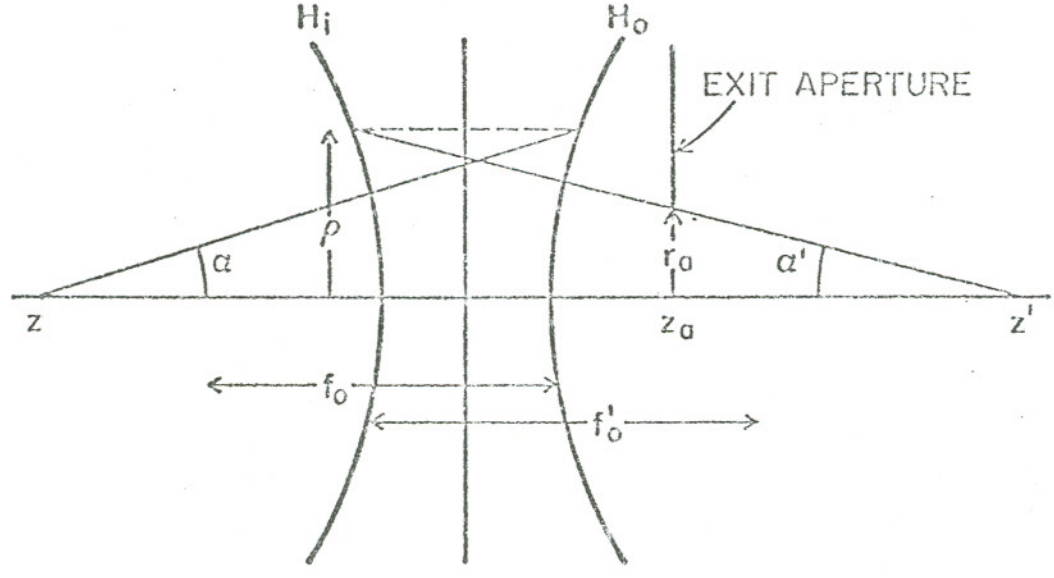

Fig. 10

Newton's equation can be written as $(z' - g)(z - g) = f^2$ for a unipotential lens (see Eqn. 15) where z, z' are measured from the center of the lens. Since the variation in f is independent

of that in g we have

$$(\Delta z' - \Delta g)(z - g) + (z' - g)(\Delta z - \Delta g) = 2f\Delta f \tag{26a}$$

With the magnification $M = \frac{f_o}{z - g_o} = \frac{z' - g_o}{f_o}$,

$$\Delta z' - \Delta g + M^2(\Delta z - \Delta g) = 2M\Delta f \tag{26b}$$

Here Δf is the difference between the focal length for a ray almost coincident with the axis (f_o) and one at some finite distance ρ from the axis (f) and similarly for Δg. If one assumes $\Delta z = 0$ (object - lens distance fixed)

$$\Delta z' = (1 + M^2)\ \Delta g + 2M\Delta f\ . \tag{26c}$$

If the object is at $z = \infty$ (parallel incoming rays), $M = 0$ and $\Delta z' = \Delta g$.

The quantities Δf and Δg have been measured for certain configurations of unipotential lenses and can be expressed to second order in ρ as

$$\frac{\Delta g}{f_o} = - C_g \frac{\rho^2}{f_o{}^2} \tag{27a}$$

$$\frac{\Delta f}{f_o} = - C_f \frac{\rho^2}{f_o{}^2} \tag{27b}$$

We consider two cases: $z = \infty$ and $z \neq \infty$. The important case when $z \neq \infty$ is $z \gtrsim f_o$ (strong magnification case). When $z = \infty$, $\Delta z'_\infty = \Delta g = - C_g \frac{\rho^2}{f_o{}^2} f_o = - C_g f_o \alpha'^2 = - C'_s(o)\alpha'^2$. The spherical aberration coefficient $C'_s(o) = C_g f_o$. The disc of confusion is then $\Delta r' = C_g f_o \alpha'^3$ for parallel incoming rays.

When $z \neq \infty$, referring to Fig. 10 we see that $\alpha' = \frac{\rho}{f_o + z' - g_o} = \frac{\rho}{f_o} \frac{1}{1 + M}$ and $\alpha = \frac{\rho}{f_o + z - g_o} = \frac{\rho}{f_o} \frac{1}{1 + \frac{1}{M}}$ and $\frac{\alpha'}{\alpha} = \frac{1}{M}$. Then we

have

$$\Delta z' = -(1 + M^2)\, C_g\, f_o \left(\frac{\rho}{f_o}\right)^2 - 2MC_f\, f_o \left(\frac{\rho}{f_o}\right)^2 \tag{28a}$$

$$= -\left[(1 + M^2)\, C_g + 2MC_f\right] f_o (1 + M)^2 \alpha'^2 \tag{28b}$$

and the disc of confusion in the gaussian image plane is given by

$$\Delta r' = \left[(1 + M^2)\, C_g + 2MC_f\right] f_o (1 + M)^2 \alpha'^3 \tag{28c}$$

or, in terms of $\alpha = M\alpha'$,

$$\Delta r' = \left[(1 + M^2)\, C_g + 2MC_f\right] f_o \frac{(1 + M)^2}{M^3} \alpha^3$$

$$= \left[\left(M + \frac{1}{M}\right) C_g + 2C_f\right] f_o \left(1 + \frac{1}{M}\right)^2 \alpha^3. \tag{28d}$$

When $z \approx f_o$, i.e. the strong magnification case $M \gg 1$ ($M \sim 50$), $\Delta r' \approx MC_g\, f_o\, \alpha^3$ and $C_s \approx C_g\, f_o$ again, since $C_g \approx C_f$ within a factor of 4 for most focal lengths used ($f_o \lesssim 5$ cm).

In the intermediate case, $M \sim 1$, from (26b) we have: $\Delta z = 0$ and $\Delta z' = -\left[(1 + M^2)\ C_g + 2MC_f\right] f_o (1 + M)^2\, \alpha'^2$; or $\Delta z' = 0$ and $\Delta z = -\left[\left(1 + \frac{1}{M^2}\right) C_g + \frac{2}{M} C_f\right] f_o \left(1 + \frac{1}{M}\right)^2 \alpha^2$. In which case, referring to <u>image space</u>

$$C'_s = -\left[(1 + M^2)\, C_g + 2MC_f\right] f_o\, (1 + M)^2 \tag{29a}$$

and referring to <u>object space</u>

$$C_s = -\left[\left(1 + \frac{1}{M^2}\right) C_g + \frac{2}{M} C_f\right] f_o \left(1 + \frac{1}{M}\right)^2 \tag{29b}$$

In the strong magnification case

$$\frac{C'_s}{C_s} = \frac{\left((1 + M^2)\, C_g + 2MC_f\right)(1 + M)^2}{\left(\left(1 + \frac{1}{M^2}\right)C_g + \frac{2}{M} C_f\right)\left(1 + \frac{1}{M}\right)^2} \simeq (1 + M)^4$$

i.e., the aberration coefficient referring to image space is approximately M^4 times larger than the coefficient referring to object space.

This means that rays coming from a point at z in object space will be spread into a disc at the gaussian plane of radius

$$\Delta r' = C_s' \alpha'^3 = C_s' \left(\frac{\alpha}{M}\right)^3 = \left[\left(M + \frac{1}{M}\right) C_g + 2C_f\right] \times f_o \left(1 + \frac{1}{M}\right)^2 \alpha^3. \qquad (30a)$$

Conversely, rays moving in the reverse direction through the lens from a point z' will be spread into a disc of radius

$$\Delta r = C_s \alpha^3 = C_s (M\alpha')^3$$

$$= \left[\left(\left(M + \frac{1}{M}\right) C_g + 2C_f\right)\right] f_o (1 + M)^2 \alpha'^3$$

M refers to rays moving from object space to image space. For rays moving in the reverse direction $M \rightarrow M' = \frac{1}{M}$ and the C_s' of Eqn. (29a) would have the same form as the C_s of Eqn. (29b), thus $C_s'(M) = C_s\left(\frac{1}{M}\right)$.

F. Electronic Aberrations

Besides the geometrical aberrations there are so-called electronic aberrations - chromatic aberration and space charge. The former is analogous to chromatic aberration in light optical systems caused by dispersion. There is no light optical analogy to space charge.

Chromatic aberration is caused by the fact that charged particles with different velocities are brought to different foci by the lens.

Space charge aberration is due to the mutual repulsion of the charged particles which causes a beam to slowly disperse. The latter aberration will not be discussed here and one should refer to reference 1, Chapter 7 for a discussion of the problem.

When the paraxial ray equation (Eqn. 6) of Appendix 1 is solved with ϕ replaced by $\phi + \Delta\phi$, it can be shown (see Ref. 6) that the variation in beam energy $\Delta\phi$ causes the image point r' to be replaced to $r' + \Delta r'$. If $\frac{\Delta\phi}{\phi} << 1$, $\Delta r'$ can be written as $[MC_{c1}r + MC_{c2}\ \alpha]\ \frac{\Delta\phi}{\phi}$ where M is the lens magnification, r the object position, α the maximum angle of acceptance of the lens, C_{c1} the coefficient of chromatic error by magnification and C_{c2} the coefficient of chromatic error of position. For magnetic lenses there is also a term describing chromatic error of image rotation. The meaning of the terms is as follows: For a given energy difference $\Delta\phi$ rays leaving the same object point a distance r from the axis will be brought to a focus at different points r' proportional to $\frac{\Delta\phi}{\phi}$ r. Also, the variation in the position of z' along the axis at which the rays are brought to a focus is proportional to $\frac{\Delta\phi}{\phi}$. The constants of proportionality are C_{c1} and C_{c2}, respectively. For points on the axis only C_{c2} is important. Calling the coefficient C_c we see that for rays with energy $\phi - \Delta\phi$ the focal point shifts by $-\Delta z' = M^2 C_c \frac{\Delta\phi}{\phi}$, causing the image at z' to be surrounded by a ring of radius $MC_c\ \frac{\Delta\phi}{\phi}\ \alpha$. If the rays have a continuous energy distribution between ϕ and

ϕ -- $\Delta\phi$ the resultant image in the gaussian plane at z' will be a disc of radius $MC_c \frac{\Delta\phi}{\phi} \alpha$, as shown in Fig. 11.

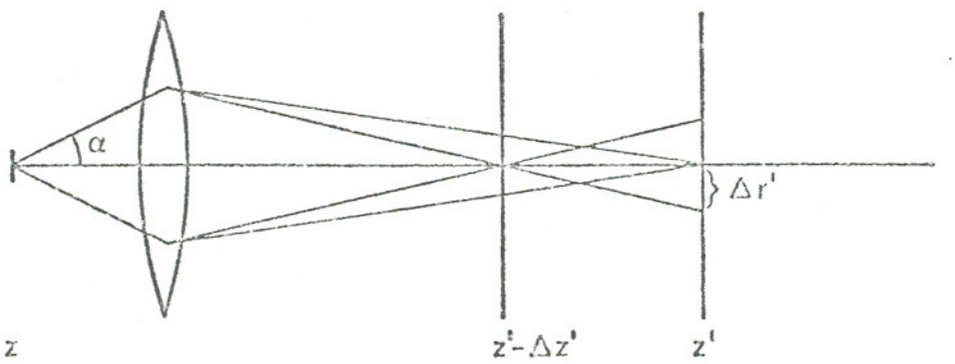

Fig. 11

Image deterioration due to longitudinal chromatic aberration.

Evidently, the cone of rays will have a minimum diameter of almost exactly $\frac{1}{2} \Delta r'$ at a distance of $\frac{1}{2} \Delta z'$ in front of the Gaussian image plane. Physically, higher energy particles will be influenced less by the lens field and so will always be brought to focus farther from the lens than particles with lower energy.

If we refer to Eqn. (26c) it is evident that when $M >> 1$, $\Delta z' \approx M^2 \Delta g$, so that $C_c = \frac{\Delta g}{\frac{\Delta\phi}{\phi}}$. C_c may be determined by differentiating the curve of g plotted as a function of $\frac{V_L}{VB}$.

The aberrations discussed here can be expressed in terms of the field distributions of the lenses, electrostatic or magnetic, so that in principle their magnitude and sign can be calculated.

However in almost all cases the field distributions cannot be expressed in a simple closed form and exact calculations are impossible. The aberration coefficients are usually measured experimentally, either with an electron optical bench or by various means of stimulating the electric potential (electrolytic trough, rubber model, etc.[1,6]). With high speed digital computers the problem of determining the properties of lenses is attacked by calculating the field distribution due to given arrangements of electrodes or magnetic pole pieces, in the case of magnetic lenses, and then tracing the paths of particles through the lens by means of Newton's equation $\frac{d\vec{p}}{dt} = e(\vec{\nabla}\phi + \vec{v} \times \vec{B})$, or by calculating the aberration coefficients in terms of integrals over the field distributions.

In a properly constructed, cylindrically symmetrical lens the primary aberrations are spherical and chromatic. The effect of these aberrations on an object point lying on the axis is to produce an image which consists of circles of radius r'_s and r'_c slightly ahead of the gaussian image plane.

$$r'_s = \tfrac{1}{4} MC_s \alpha^3 \tag{31a}$$

$$r'_c = \tfrac{1}{2} MC_c \frac{\Delta\phi}{\phi} \alpha \tag{31b}$$

where M is the magnification of the lens, C_s is the spherical aberration coefficient referred to object space, α is the angle of the ray leaving the object which just passes through the aperture, C_c is the coefficient of chromatic aberration, ϕ is the

energy of the beam and $\Delta\phi$ the energy spread. The combined effect is generally taken to be

$$r = M\left[\frac{C_s{}^2\alpha^6}{16} + \frac{C_c{}^2\left(\frac{\Delta\phi}{\phi}\right)^2\alpha^2}{4}\right]^{1/2} \qquad (32)$$

Sometimes one finds C_s used instead of $\frac{1}{4}\,C_s$, and care should be exercised before using values of C_s to know which notation is intended and also for what object-lens distance C_s was measured.

It would appear that the effect of the lens aberrations could be made arbitrarily small by decreasing α. There are two problems, however. First, as α is made smaller by decreasing the aperture size the current passing the aperture decreases. Second, there is the effect of the non-zero de Broglie wavelength of the particles. The wavelength is given by $\lambda = \frac{h}{p} = \frac{h}{(2me\Phi)^{1/2}}$. $\lambda_{elec} = \frac{12.5}{\Phi^{1/2}}$ Å, for Φ in volts. For protons, $\lambda_p = \frac{1}{43}\,\lambda_{elec}$. A beam of wavelength λ, whether light or charged particles, will be diffracted upon passing through an aperture. If the aperture is circular the diffraction pattern consists of a bright central disc surrounded by fainter rings. The diameter of the central disc, called the Airy disc, is given[6] by $d = \frac{0.61\,\lambda}{\sin\,\alpha}$. For an ion beam diffraction is of no consequence - for a 10 kV beam of protons d is negligible until $\alpha < 10^{-4}$ radians. For electrons, however, diffraction is a serious problem if $\alpha < 2 \times 10^{-3}$ radians when the energy $\sim$ 10 kV. The image of a point object formed by an electron beam is expressed as

$$r' = M\left[\frac{C_s^2\alpha^6}{16} + \frac{C_c^2}{4}\left(\frac{\Delta\phi}{\phi}\right)^2 \alpha^2 + \left(\frac{7.6}{\alpha}\right)^2 \frac{1}{\phi}\right]^{1/2}$$

so there is an optimum value of α which will minimize the image size.

G. Beam Deflection System

In order to scan a beam over a specimen it is necessary to have a deflection system which applies appropriate electric or magnetic fields to the charged particles.

The subject of deflection system design is one of intense interest because of the need for wide area deflection in e-beam lithographic systems used for integrated circuit manufacture, as well as in cathode ray tubes. In these cases it is necessary to move the beam many millimeters across a target while maintaining high resolution. A less rigorous problem is the deflection system for a scanning microscope. Here the resolution requirements increase as the scanned area is decreased (that is, as the magnification of the microscope increases), so the effect of the deflection system on the state of focus becomes less as the need for high resolution becomes greater.

Beam spot size (or state of focus) is affected several ways by beam deflection. The most obvious way is that when the beam is deflected it has to travel a greater distance before reaching the specimen, so the point of focus moves above the specimen plane as

the deflection angle increases. This can be compensated for by changing the focal length of the lens slightly. The amount of change is proportional to $x^2 + y^2$ where x and y are the coordinates of the beam on the specimen with respect to the optical axis. This is called the dynamic focus correction method.

A second way in which deflection can affect spot size is through the lens properties of the deflection system. Any arbitrary magnetic or electric field distribution acts to deflect the beam. If the field has symmetry in some plane it will tend to focus the beam in that plane or in a plane perpendicular to it, if the field is a magnetic one.

Magnetic deflection systems are not suitable for ion beams because of the small charge to mass ratio, so electrostatic systems must be used. Consider such a system consisting of two plates of length ℓ separated by a distance d. A beam of diameter Δy passes through the plates equidistant from them. If a potential V_p is placed across the plates a field $E_p = \frac{V_p}{d}$ will exist between them (neglecting fringing at the ends). The transverse velocity imparted to the beam is $v_t \int \frac{e}{m} E_p \, dt = \int \frac{e}{m} \frac{V_p}{d} \frac{ds}{v} = \frac{e}{m} \frac{\ell}{d} \frac{V_p}{v}$, where v is the speed of the beam, $v^2 = v_z^2 + v_t^2$. $v_z = \left(2\frac{e}{m} V\right)^{\frac{1}{2}}$ where V is the beam acceleration voltage. The angle of deflection is given by

$$\tan \theta = \frac{v_t}{v_z} = \frac{\frac{e}{m} \frac{\ell}{d} \frac{V_p}{v}}{v_z} = \frac{e}{m} \frac{\ell}{d} \frac{V_p}{v_z \left(v_t^2 + v_z^2\right)^{\frac{1}{2}}} \qquad (33)$$

Solving for $\left(\frac{v_t}{v_z}\right)^2$ we find

$$\left(\frac{v_t}{v_z}\right)^2 = \frac{1}{2}\left[-1 + \left(1 + \left(\frac{2\frac{e}{m}\frac{\ell}{d}V_p}{v_z^2}\right)^2\right)^{\frac{1}{2}}\right]$$

$$= \frac{1}{2}\left[\frac{1}{2}\left(2\frac{e}{m}\frac{\ell}{d}\frac{V_p}{v_z^2}\right)^2 - \frac{1}{8}\left(2\frac{e}{m}\frac{\ell}{d}\frac{V_p}{v_z^2}\right)^4 + - \ldots.\right] \qquad (34)$$

For small deflection angles we may ignore the higher terms and, with $v_z^2 = 2\frac{e}{m}V$

$$\tan\theta = \theta = \frac{v_t}{v_z} = \frac{1}{2}\frac{\ell}{d}\frac{V_p}{V} . \qquad (35)$$

This calculation assumes the field falls to zero abruptly outside the region of the deflection plates. This is clearly not the case, however Recknagel[12] showed that if the length of the plates ℓ is replaced by $\ell + \Delta\ell$ where

$$\Delta\ell = 0.318\ d\left[1 - \ln\left(0.636\frac{d}{\ell}\right)\right] \qquad (36)$$

then the calculations will be valid. The potential of the beam will be changed as it passes through the plates. Differentiating the equation for θ one gets $\delta\theta = \frac{1}{2}\theta\frac{\delta V_p}{V_p}$, where $\delta V_p = \frac{V_p}{d}\delta y$ is the distance along the field lines between the plates. If the width of the beam is Δy, one edge will be deflected by $\Delta\theta$ more than the other edge - the deflection system acts like a lens in the plane of the field E_p. When the beam has traveled a distance F, $F\delta\theta = \Delta y$

and the edges of the beam intersect, so F is the focal length of the deflection system, to first order.

A pair of parallel plates will change the shape of the beam profile, introducing astigmatism. This is easily seen by considering the two plates each to be at $+V_p$ above ground so that the midplane is an equipotential. The action of them will be to "flatten" the beam. Indeed, this principle is used in electrostatic astigmatism correctors. If deflectors for the x-direction are followed by similar deflectors for the orthogonal (y) direction the astigmatism will be corrected to some extent.

The third way spot size is affected is that, by moving the beam off the optical axis and tilting it before passing it through a lens will increase the contribution of the lens aberrations to the spot size.

The precise effect of beam deflectors must be calculated numerically by computer. In a scanning microscope where resolution requirements decrease as the deflection angle increases the problem is relatively simple. In high resolution CRT's, e-beam lithography systems, etc. where resolution must be maintained over large deflection angles the problem is serious and of considerable present interest (see for example, the article by E. Munro[11] and related articles in the same reference journal).

APPENDIX 1

For a rotationally symmetric lens $\Phi = \Phi(r,z)$ where r is the radial distance from the z-axis (the optical axis). Then

$$\nabla^2 \Phi = \frac{1}{r}\frac{\partial}{\partial r} r \frac{\partial \Phi}{\partial r} + \frac{\partial^2 \Phi}{\partial z} = 0 \qquad (1)$$

We are only interested in the potential near the axis, so we represent it by a power series expansion:

$$\Phi(r,z) = \sum_{n=0}^{\infty} A_n(z)\, r^n \text{ so that}$$

$$\nabla^2\Phi = \sum_{n=0}^{\infty}\left[n^2 A_n(z)\, r^{n-2} + \frac{\partial^2 A_n(z)}{\partial z^2} r^n\right] = 0, \text{ or, relabeling}$$

with $m = n - 2$,

$$\nabla^2\Phi = \frac{A_1}{r} + \sum_{m=0}^{\infty}\left[(m+2)^2 Am + 2\,(z) + \frac{\partial^2 Am(z)}{\partial z^2}\right] r^m = 0 \qquad (2)$$

Since Φ is finite at $r = 0$, $A_1 = 0$. The recursion relation

$$\frac{\partial^2 Am}{\partial z^2} = -(m+2)^2 Am + 2$$

tells us $Am = 0$ if m is odd. Let $Ao(z) = \Phi(0,z) \equiv \phi(z)$. Then $A_2 = -\frac{1}{4}\frac{\partial^2\phi}{\partial z^2}$, $A_4 = +\frac{1}{64}\frac{\partial^4\phi}{\partial z^4}$ etc. and

$$\Phi(r,z) = \phi(z) - \frac{r^2}{4}\frac{\partial^2\phi(z)}{\partial z^2} + \frac{r^4}{64}\frac{\partial^4\phi}{\partial z^4} + \ldots. \qquad (3)$$

Retaining terms through r^2 the Lagrangian for meridional rays is, with $\frac{dz}{dt} \equiv \dot{z}$ and $\frac{dr}{dz} \equiv r'$

$$L = \frac{1}{2} m (\dot{r}^2 + \dot{z}^2) - e\phi + \frac{e}{4} r^2 \phi'' - eV_{acc} \tag{4}$$

The Lagrange equations $\frac{d}{dt} \frac{\partial L}{\partial \dot{q}_i} - \frac{\partial L}{\partial q_i} = 0$ yield

$$m\ddot{r} = \frac{\partial L}{\partial r} = \frac{er\phi''}{2} \tag{5a}$$

$$m\ddot{z} = \frac{\partial L}{\partial z} = - e\phi' + \frac{er^2}{4} \phi''' \tag{5b}$$

Eqn. (5a) implies lens action because $\ddot{r}$ is proportional to r.

In the Gaussian approximation $r' = \frac{dr}{dz} << 1$. Then $\dot{r} = \frac{dr}{dz} \dot{z} = r' \dot{z}$ shows that $\frac{\dot{r}}{\dot{z}} << 1$ so that $\frac{1}{2} mV^2 \approx \frac{1}{2} m\dot{z}^2 = eV_{acc} - e\phi$. It is convenient to add a constant to the potential so that $\frac{1}{2} mV^2 + e\phi = 0$, rather than eV_{acc}. With $\frac{e}{m} = \eta$, from Eqns. (5a) and (5b)

$$\ddot{r} = \frac{\eta r\phi''}{2} = \frac{d(r' \dot{z})}{dt}$$

$$= \ddot{z} r' + \dot{z}^2 r''$$

$$= - \eta\phi' r' - 2\eta\phi r''$$

to first order in r. By dividing by $2\eta\phi$ there results the paraxial ray equation describing the trajectory of a particle through the lens:

$$r'' + r' \frac{\phi'}{2\phi} + r \frac{\phi''}{4\phi} = 0 \tag{6}$$

Since $\phi = \phi(z)$, we can rewrite (1) as

$$\frac{d^2 r}{dz^2} + P(z) \frac{dr}{dz} + Q(z) r = 0 \tag{7}$$

with $P(z) = \frac{\phi'}{2\phi}$, $Q(z) = \frac{\phi''}{4\phi}$.

APPENDIX 2

This demonstration is taken from Klemperer and Barnett (Reference 1).

Consider Fig. 2A. At some point z_{min} and r_{min}

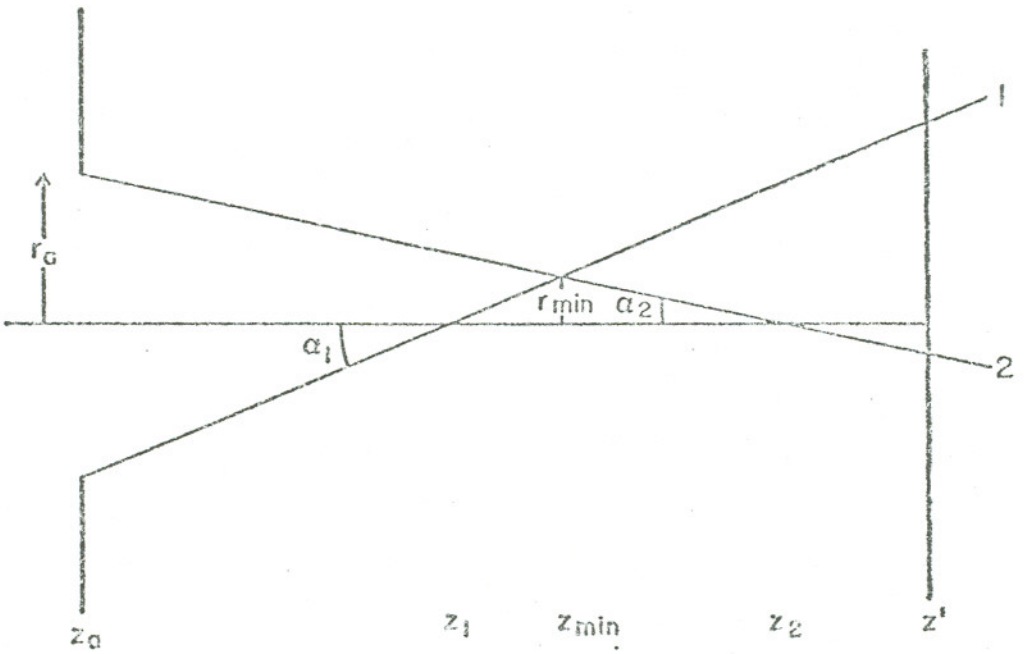

Fig. 2A

$$\overline{z_1 z'} \approx C_s \alpha_1^2, \quad \overline{z_2 z'} = C_s \alpha_2^2$$

$$\overline{z_{min} z_2} = \overline{z_1 z'} - \overline{z_2 z'} - \overline{z_1 z}_{min}$$

$$= C_s \alpha_1^2 - C_s \alpha_2^2 - \overline{z_1 z}_{min}$$

$$= C_s (\alpha_1^2 - \alpha_2^2) - \overline{z_1 z}_{min}$$

then

$$r_{min} = \overline{z_1 z}_{min} \alpha_1 = \overline{z_{min} z_2} \alpha_2$$

$$= \left[C_s(\alpha_1^2 - \alpha_2^2) - \overline{z_1 z}_{min}\right]\alpha_2$$

also $z_1 z_{min}\ (\alpha_1 + \alpha_2) = \overline{z_{min} z_2}\alpha_2 + \overline{z_1 z}_{min}\ \alpha_2$

$$= C_s(\alpha_1^2 - \alpha_2^2)\alpha_2$$

$$= C_s(\alpha_1 + \alpha_2)(\alpha_1 - \alpha_2)\alpha_2$$

so that $\overline{z_1 z}_{min} = C_s(\alpha_1 - \alpha_2)\alpha_2$

and $r_{min} = C_s(\alpha_1 - \alpha_2)\alpha_1\alpha_2$

We minimize this by varying α_2, since we want to keep α_1 fixed by choosing an aperture radius:

$$\frac{\partial r_{min}}{\partial \alpha_2} = C_s(\alpha_1^2 - 2\alpha_1\alpha_2) = 0$$

$$\alpha_2 = \frac{\alpha_1}{2}$$

$$r_{min} = C_s\left(\alpha_1 - \frac{\alpha_1}{2}\right)\alpha_1\frac{\alpha_1}{2}$$

$$= \frac{C_s\alpha_1^3}{4}$$

$$\left(\frac{\partial^2 r_{min}}{\partial \alpha_2^2} = -2C_s, \text{ so this is a minimum}\right).$$

The position of this minimum point of "disc of least confusion" is $\overline{z_{min} z_i} = \overline{z_1 z_i} - \overline{z_1 z}_{min}$

$$= C_s\alpha_1^2 - C_s(\alpha_1\alpha_2 - \alpha_2^2)$$

$$= C_s\alpha_1^2 - C_s\ \frac{\alpha_1^2}{2}\ \frac{\alpha_1^2}{4}$$

$$= \frac{3}{4}\ C_s\alpha_1^2 = \frac{3}{4}\ \overline{z_1 z_i}$$

i.e., the waist occurs 3/4 of the way from where the outermost rays cross the axis to the gaussian image plane.

REFERENCES

1. O. Klemperer and M. E. Barnett, Electron Optics, 3rd Ed., Cambridge University Press (1971).

2. A. Messiah, Quantum Mechanics, North-Holland Publishing Co. (1965).

3. H. Goldstein, Classical Mechanics, Addison-Wesley Press, Inc. (1951).

4. M. Born and E. Wolf, Principles of Optics, The Macmillan Co. (1959).

5. C. Hall, Introduction to Electron Microscopy, 2nd Ed., McGraw-Hill Book Co. (1966).

6. V. K. Zworykin, G. A. Morton, E. G. Ramberg, J. Hillier, and A. W. Vance, Electron Optics and the Electron Microscope, John Wiley and Sons, Inc. (1945).

7. J. C. Wiesner, Report No. ERL-70-6, College of Engineering, University of California at Berkeley (1970).

8. F. Hildebrand, Advanced Calculus for Applications, Prentice-Hall, Inc. (1962).

9. P. W. Hawkes, Electron Optics and Electron Microscopy, Barnes and Noble Books (1972).

10. G. Liebmann, Proc. Phys. Soc. Sec. B, 62 (1949) 213.

11. E. Munro, J. Vac. Sci. and Tech. 12 (1975) 1146.

12. A. Recknagel, Z.Physik 111 (1938) 61.

III. REVIEW OF THE THEORY OF FIELD IONIZATION

A. Introduction

In order to understand the physical principles which govern the behavior of the FI source three important subjects should be discussed: the mechanism of field ionization; the reasons for and nature of the energy distribution of the ion beam; the means by which the material to be ionized is supplied to the field emitter, which determines the current.

A unique feature of the FI source is that it is a quantum mechanical device - it is not possible to explain its behavior in a classical way. Field ionization is the ionization of an atom (or molecule) by electron tunneling through a field-distorted atomic coulomb barrier. There is no classical analogue. When an atom is placed in an electric field of strength comparable to the internal atomic field, the atomic potential is so distorted that there is a finite probability an electron in the atom will "tunnel under" the potential barrier and escape.[1] To visualize this phenomenon consider a hydrogen atom in one dimension. In Fig. 1a the energy diagram for an H atom in field free space is shown with $V = \frac{-e^2}{4\pi\epsilon_o |x_i - x|}$. In Fig. 1b the energy diagram for the H atom in a strong electric field F. The potential energy is now $V = eFx - \frac{e^2}{4\pi\epsilon_o |x_i - x|}$.

The field must be very strong for there to be any reasonable probability for ionization, as is known from everyday experience.

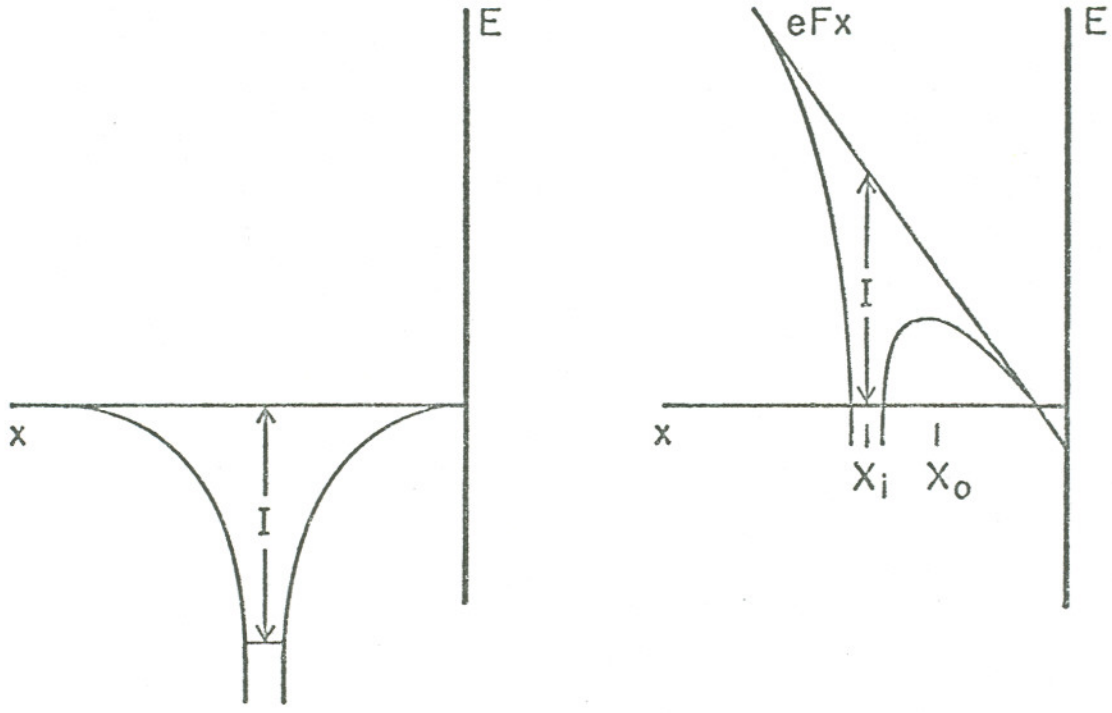

Figure 1a and 1b

An estimate of the order of magnitude of the field can be made using the uncertainty principle.[2] The maximum height of the barrier, where $\frac{\partial V}{\partial x} = 0$, corresponds to $\frac{(\Delta p)^2}{2m}$, $V = eFX - \frac{e^2}{4\pi\epsilon_o |x_i - x|}$, so $\frac{\partial V}{\partial x}\Big|_{x_o} = 0$ yields $x_o = x_i - \sqrt{\frac{e}{4\pi\epsilon_o F}}$. Then $V(x_o) = eFx_i - 2\sqrt{\frac{e^3F}{4\pi\epsilon_o}} = eFx_i - \Delta V$. If it is assumed that the atomic energy levels aren't shifted too drastically,* it can be seen from Fig. 1b that $eFx_i \approx I$, so $V(x_o) \approx I - \Delta V$ and $\Delta p \approx \sqrt{2m(I-\Delta V)}$. The barrier width Δx can be calculated by finding the two values of x for which V = 0. Solving

---

*The first order energy shift for a hydrogen atom, $\langle \psi_o | eFx | \psi_o \rangle$ is zero (Stark effect), for example.

$eFx - \frac{e^2}{4\pi\epsilon_o |x_i - x|} = 0$ for x,

$x = \frac{x_i \pm \sqrt{x_i^2 - 4\frac{e}{4\pi\epsilon_o F}}}{2}$, $\Delta x = \sqrt{x_i^2 - \frac{4e}{4\pi\epsilon_o F}}$, or, with $I = eFx_i$,

$\Delta x = \sqrt{\frac{I^2}{e^2F^2} - \frac{4e}{4\pi\epsilon_o F}}$. The uncertainty principle is $\Delta x \Delta p \approx h$, so by inserting our values for Δx and Δp one obtains $\frac{I^3}{e^2F^2}$.

$$\left[1 - \frac{\Delta V}{I} - \left(\frac{\Delta V}{I}\right)^2 + \left(\frac{\Delta V}{I}\right)^3\right] = \frac{h^2}{2m} .$$

For hydrogen I = 13.5 eV, $F \approx \left(\frac{2mI^3}{e^2h^2}\right)^{1/2} \approx 1.5 \times 10^{10}$ volts/meter (1.5 V/Å) and $\Delta V \approx 0.7$ I. The electric field in a hydrogen atom at a distance of 0.5 Å from the nucleus is ≈ 60 V/Å, so the approximation that the energy levels aren't shifted too greatly is reasonable.

B. Calculation of Ionization Rate by the WKB Approximation

In order to calculate ionization rates for gas atoms in the vicinity of a field emitter held at a high potential, a three-dimensional Schrödinger equation must be solved using a potential which includes information about the emitter crystal structure, the electron wavefunctions of the metal atoms, the polarization of the atom before ionization and of the ion afterwards and the value of the field at the emitter surface. This problem has not been solved exactly, but many features of field ionization have been calculated using various

approximations. The simplest approximation was the one first used by Müller,[2] a one-dimensional WKB approximation. The potential used is a classical one, assumed to be valid everywhere:

$V = \frac{-e^2}{4\pi\epsilon_o|x_i-x|} + eFx - \frac{e^2}{16\pi\epsilon_o x} + \frac{e^2}{4\pi\epsilon_o|x_i+x|}$. Here x_i is the position of the center of mass of the atom [the nucleus] and the third and fourth terms are due to the electrical images of the electron and the ion, respectively. The field F is assumed to go to zero at $x = 0$. In other words, the emitter is replaced by an idealized continuous conducting plane with no atomic features. This is a rather drastic approximation since the ionization takes place only a few angstroms from the atomic lattice of the emitter, but the calculation does bring out the dependence of ionization probability, and hence current, on the field, ionization potential of the gas and work function of the emitter. It also gives a qualitative explanation of the gross energy distribution of the ions as a function of field. Therefore it is worthwhile to see how the WKB approximation is developed and applied.

Suppose the origin to be at the center of the atom, $x_i = 0$ (see Fig. 2). The electron is represented by a plane wave approaching the potential barrier which extends between $x = x_c$ and $x = x_o$. Assume the electron is represented by an outgoing wave for $x > x_c$, by a WKB wavefunction for $x_o < x < x_c$ and by a plane wave plus a reflected plane wave for $x < x_o$. After a somewhat lengthy calculation, which may be found in Appendix 1 the probability of the electron penetrating the

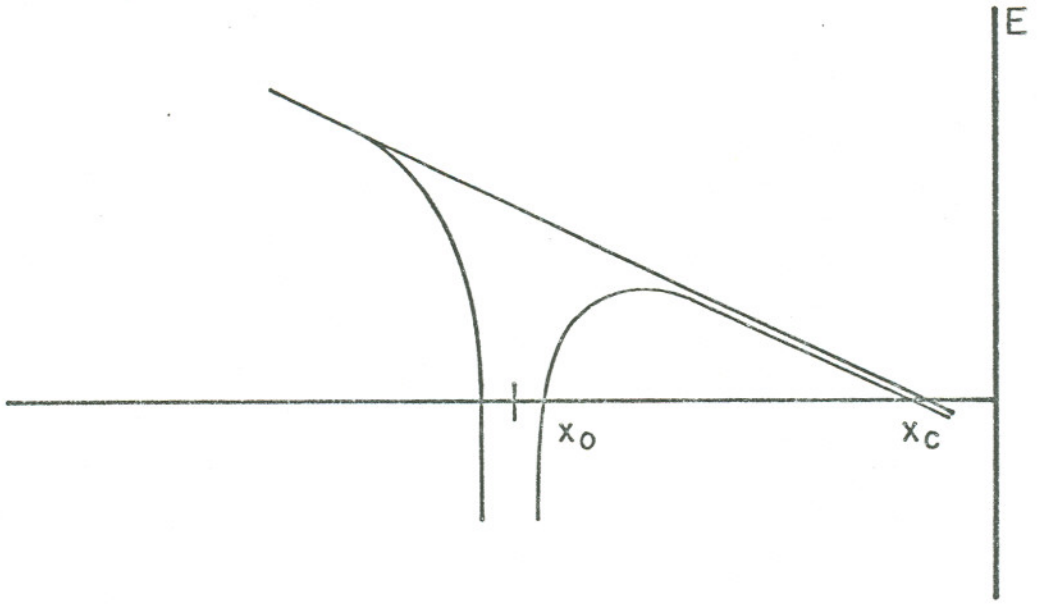

Figure 2

barrier, i.e. ionization, is found to be $D = \exp\left(-1.6 \times 10^{38} \frac{I-\phi}{F} \cdot (I - 1.22 \times 10^{-23} F^{1/2})^{1/2}\right)$. I is the ionization potential of the atom in electron volts, ϕ the work function of the metal field emitter in electron volts and F the applied electric field in volts/meter. For an H atom (I = 13.5 eV) and an Ir emitter (Φ = 5.3 eV) with a field of F = 2 V/Å, $D \approx e^{-6.9} = 10^{-3}$. This is the probability the electron will penetrate the barrier.

To a first approximation the probability of ionization decreases as $e^{-\gamma x_c}$ where γ is a measure of how wide the barrier is (ignoring the change in barrier height with x). A 10% increase in x_i will result in ~ 30% decrease in D. In an extremely simple picture one can imagine the electron approaching the barrier at the rate $\nu = \frac{E}{h}$, where E

is the electron energy in the ground state. The probability of not penetrating the barrier is 1 - D, and the probability of not penetrating it in n attempts is $(1 - D)^n$. Setting $(1 - D)^n$ equal to 1/2 we can define the mean time for ionization as $T \equiv \frac{n}{\nu}$.

$n = \frac{\ln (1/2)}{\ln (1-D)}$ so $T = \frac{-0.693}{\ln (1-D)\nu}$. Since $D << 1$, $\ln (1-D) = -D + 1/2\ D^2 - 1/3\ D^3 + \ldots \approx -D$ and $T = \frac{0.693}{D\nu}$. Using the Poisson distribution the probability of not penetrating the barrier is given by $e^{-t/T}$ and the probability for ionization is $P(t) = 1 - e^{-t/T} = 1 - e^{-\frac{D\nu t}{0.693}} \approx \frac{D\nu t}{0.693}$, for small t.

The WKB approximation is useful for seeing how the main physical parameters - electric field strength, ionization potential and work function - interact to determine the ionization rate and hence the ion current. There are so many approximations in the calculation that the quantitative results aren't very accurate - for example, the predicted[3] energy distribution of the ions is too broad by a factor of 2 while other features of the distribution aren't predicted at all. We will discuss the energy distribution below in terms of the results of more accurate calculations.

C. Energy Distribution

The most important parameter of the source is the energy distribution of the ion beam. This can be determined by calculating the probability of ionization as a function of distance from the tip (the further from the tip an atom is ionized the less kinetic energy the

ion will have). Considerable effort has gone into calculations of the energy distribution. In order to get accurate results it has been necessary to calculate the ionization rate more carefully, using more accurate characterizations of the potential near the tip, and solving the Schrödinger equation in three dimensions.

Boudreaux and Cutler[4] performed a more elaborate calculation in order to try and explain the energy distribution of the ion current. Rather than use the WKB approximation they considered the ionization process to be a re-arrangement scattering process in three dimensions, in which the incoming atom scatters from the tip and loses an electron in the process. This was done by setting up the Schrödinger equation for the system {tip + electron + ion} with an interaction potential between the ion and the tip approximated by an image potential, and calculating the cross section for ionization. An outline of the procedure may be found in Appendix 2. The cross section was found to be proportional to $k_\alpha^{-7}\,\epsilon^{-1/2}$, where $k_\alpha = \frac{2\pi}{h}(2mE_\alpha)^{1/2}$, E_α is the energy level of the emitter into which the electron falls and ϵ is the kinetic energy of the atom before ionization. Since the scattering measures the ionization rate, the probability P(K) of ionization and hence the current is proportional to $k_\alpha^{-7}\,\epsilon^{-1/2}$. E_α can range from E_F up to the vacuum level and since the ionization probability is very sensitive to k_α most of the ionization will occur when k_α has its minimum value, i.e., when $k_\alpha = k_F$. Boudreaux and Cutler estimated the width of the ionization zone ΔR and the energy spread

of the beam by calculating the value of K_α for which $P(K_\alpha) = 1/2P(K_F)$. The result was $\Delta R = 0.12$ Å for the width of the ionization zone, corresponding to a FWHM of ≈ 0.25 eV. Müller and Tsong's[3] experimental results for hydrogen are shown in Fig. 3.

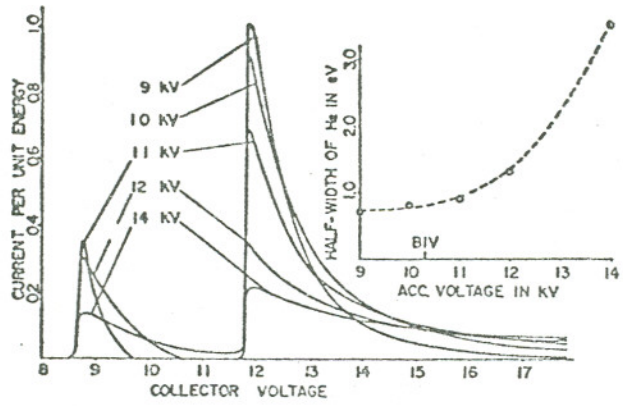

Figure 3

(Reproduced from Ref. 3)

Interest in the problem of the energy distribution was sparked when Jason et al[5] discovered it had more structure than what Müller and Tsong found (see Fig. 4, reproduced from reference 6). Jason accounted[6] for the structure by postulating that the electrons tunneled through the potential barrier resonantly, the resonances occurring at the energy eigenvalues of a triangular well as shown in Fig. 5. The predicted energies correspond roughly to the observed structure and also spread apart as the field increases, which is in qualitative agreement with experiment. The explanation is not adequate however. The actual spacing of the resonances will clearly

depend on the detailed interaction of the electron with the metal surface and it is incorrect to treat the surface as a featureless barrier, as was recognized by Jason.

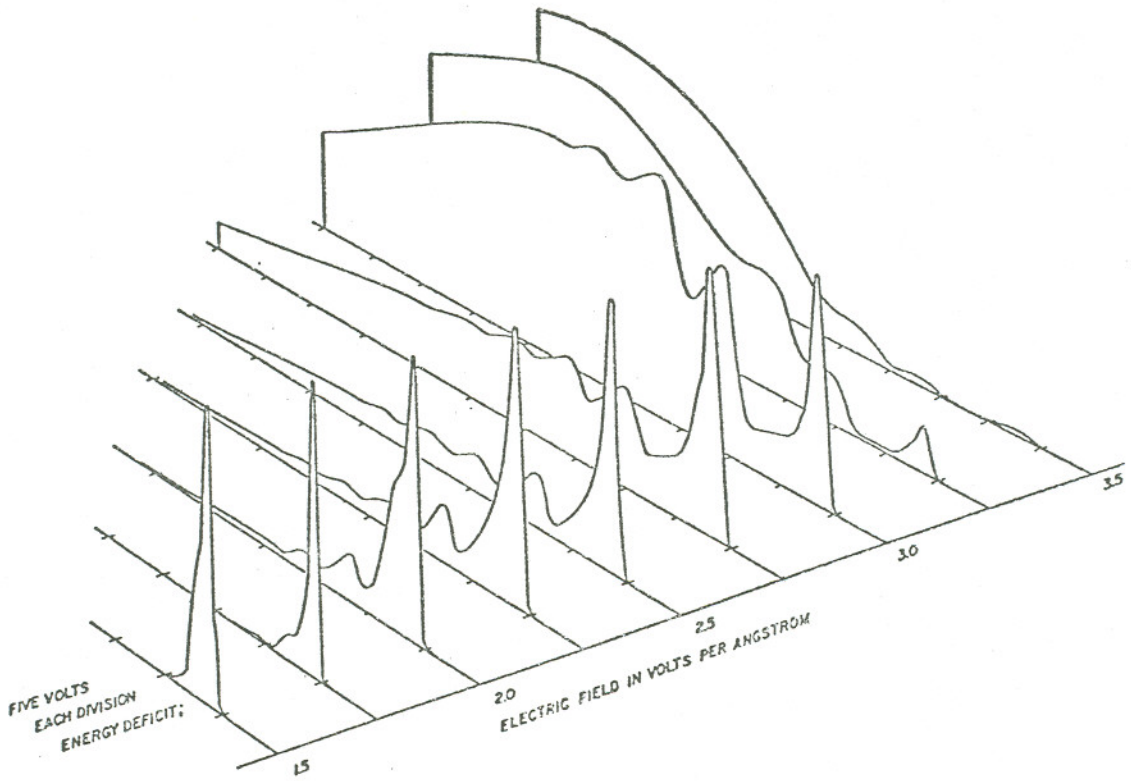

Figure 4

(Reproduced from Ref. 6).

Jason's[6] measurements of ΔE vs. electric field for H_2^+, showing relative intensity of current vs. energy deficit.

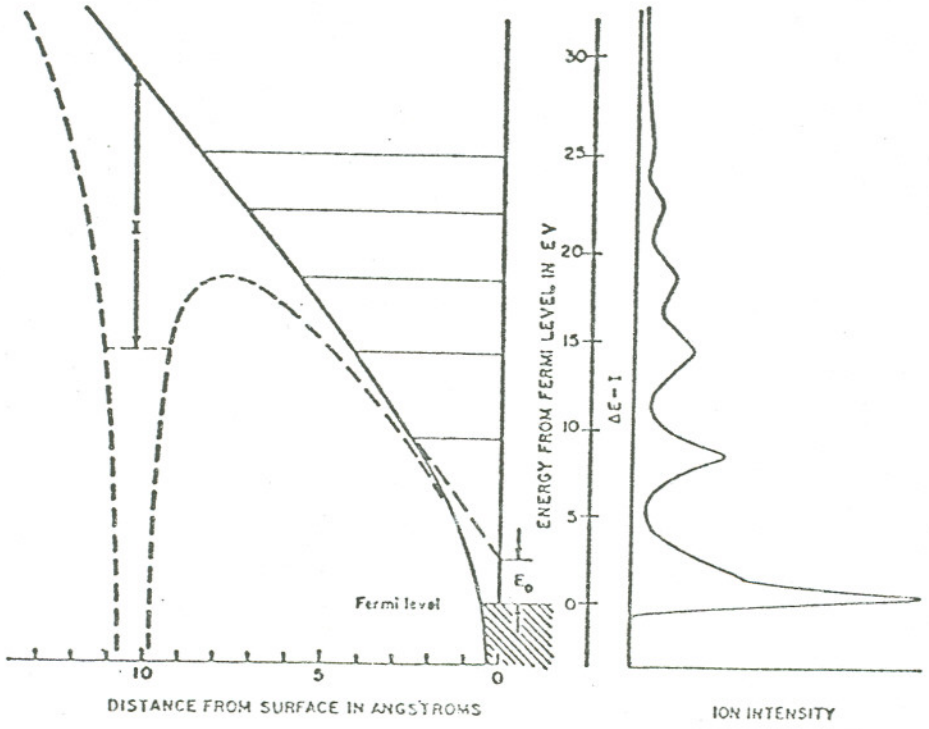

Figure 5

(Reproduced from Ref. 6)

A better treatment was provided by Appelbaum and McRae.[7] Their method consists of setting up the time dependent Schrödinger equation in terms of two "hypothetical" Hamiltonians H_L and H_R which are equal at a point Z_o where the metal-atom potential is a maximum (see Fig. 6). H_L describes the electrons in the metal and H_R the electron in the atom. These have eigenfunctions ψ_i and ψ_a respectively, which are not orthogonal.

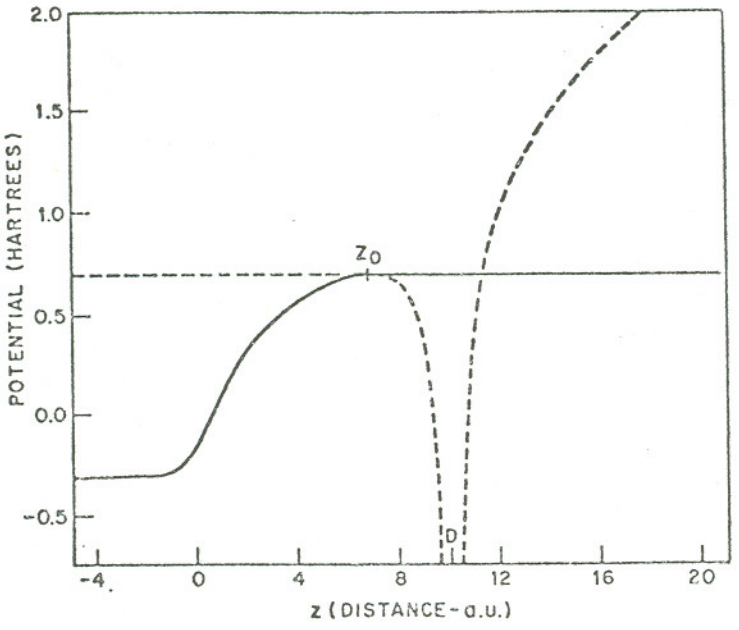

Figure 6

(Reproduced from Ref. 7)

The potentials used by Appelbaum and McRae.[7] The solid line is the potential for H_L and the dashed line the potential for H_K. The transition matrix $\langle\bar{\psi}_i|H - E_a|\bar{\psi}_a\rangle$ is calculated at the point z_o.

The total wave function is then written as

$$\psi = A(t)\exp(-iE_a t)\bar{\psi}_a + \sum_i M_i(t)\exp(-iE_i t)\bar{\psi}_i \qquad (1)$$

$\left(\hbar = m = e = 1,\ \psi_q = \bar{\psi}_q \exp(-iE_q t)\right)$. ψ_a is assumed localized around the atom and ψ_i near the metal. E_a and E_i are the energy levels of the atom and the metal, respectively. A(t) and M(t) are time dependent coefficients with $A(0) = 1$ and $M_i(0) = 0$. By inserting this wave function in the time-dependent Schrödinger equation $i\frac{\partial\psi}{\partial t} = H\psi$, multiplying by ψ_i^* and integrating they obtained $i\frac{\partial M_i}{\partial t} = A\langle\bar{\psi}_i|H-E_a|\bar{\psi}_a\rangle$, where terms such as $\frac{\partial A}{\partial t}\langle\bar{\psi}_i|\bar{\psi}_a\rangle$ are ignored because $\frac{\partial A}{\partial T}$ and $\langle\bar{\psi}_i|\bar{\psi}_a\rangle$ are small quantities. $\frac{\partial M_i}{\partial t}$ is the rate at which the amplitude for finding the electron in the metal increases with time $\left(\frac{\partial M}{\partial t} = -\frac{\partial A}{\partial t}\right)$, so the ionization rate (current) is

$$J = \sum_i \frac{\partial|M_i|^2}{\partial t} = 2\pi\Sigma\ \delta(E_i-E_a)\left|\langle\bar{\psi}_i|H-E_a|\bar{\psi}_a\rangle\right|^2 \qquad (2)$$

if A is taken to be ≈ 1 in the limit of long times $\left(\frac{\partial A}{\partial t} << 1\right)$. The energy distribution is then determined by the integral $\langle\bar{\psi}_i|H-E_a|\bar{\psi}_a\rangle$.

$\bar{\psi}_a$ is taken to be essentially the atomic wave function: $\bar{\psi}_a \sim e^{-\alpha|r-R_n|}\ e^{-\gamma(Z-Zn)}$ where R_n is the position of the atom and Z_n is the Z coordinate of the atom. α depends on the ionization potential and γ on the field strength. The electric field at ~ 2 V/Å has little effect on the atom wave function ($\gamma \sim 0.1$). Determination of $\bar{\psi}_i$ is more difficult. The exact Hamiltonian H_L isn't known, so certain approximations must be made. In the absence of the atom the

potential is very complex and three-dimensional near the metal surface and becomes a one-dimensional potential consisting of FZ plus an image potential for the electron as Z increases. When the atom is present this is disturbed, but the effect near the metal surface is small because the metal remains an equipotential. It was assumed that the three-dimensional character of the potential could be ignored and that the potential can be expressed in terms of Z only. The wave function was expressed as a product of $\phi(Z)$ with a plane wave e^{iKZ}, where $\phi(Z)$ depends on the potential. For $Z > Zo$, $\phi(Z) = \phi(Zo)e^{-\kappa(Z-Zo)}$, $\kappa = (2V(Zo) + \kappa^2 - 2E_i)^{1/2}$. The integral $\langle\bar{\psi}_i|H-E_a|\bar{\psi}_a\rangle$ yields $J \sim D|\phi(Zo)|^2$.

The new physical content in this procedure comes in the determination of $\phi(Z)$. $\phi(Z)$ and its logarithmic derivative must join smoothly to the metal wavefunctions (Bloch wavefunctions) at $Z = 0$. The conditions for joining the wave functions for the metal interior and exterior were written by decomposing the Bloch wavefunctions into plane waves incident on the metal surface which are partially transmitted and partially reflected. The wavefunction outside the metal must approach the Bloch wavefunction as $Z \to 0$. The wavefunction is now written in terms of incident and reflected plane waves which match to the Bloch wavefunctions. The current across the boundary at $Z = 0$ must equal the ionization rate so J can be written in terms of the transmission coefficients for the plane waves across the boundary, or in terms of the reflection coefficients: $J \sim \frac{(1-|R|^2)}{|1-Re^{-2i\ \Delta}|^2}$

where Δ is a phase shift. This form for J produces a resonance effect, since $\Delta = \Delta(Z)$ is a monotonically increasing function of Z. For a phase difference of π the ratio of maximum to minimum current is $\frac{J_{max}}{J_{min}} = \frac{1-|R|^2}{(1-|R|)^2} \times \frac{(1+|R|)^2}{1-|R|^2} = \left(\frac{1+|R|}{1-|R|}\right)^2$. The spacing and relative intensity of the peaks in the energy distribution depend on the amplitude and phase of the reflection coefficients of the electrons on the metal surface.

The authors calculated the reflection coefficients using LEED data for low energy electrons on W(011). Their calculated values for the spacing and intensity of the peaks in the energy distribution of field ionized He, Ne and H_2 gases agree remarkably well with experiment (see Fig. 7).

While of great interest insofar as understanding the mechanism of field ionization, the theoretical explanation of the nature of the "Jason Peaks" is not terribly relevant to scanning ion microprobes. The reasons are that: (1) the intensity of the Jason peaks is low at the fields used, so little current is in them; (2) the Jason peaks are separated from the main intensity peak by many eV so that the chromatic aberration of the lenses of a microprobe will simply spread the lower energy ions into a large circle in the image plane where they will appear as a background "fog."

An interesting effect related to ionization current is that on a clean metal surface, adsorbed noble gas atoms (ad-atoms) can enhance

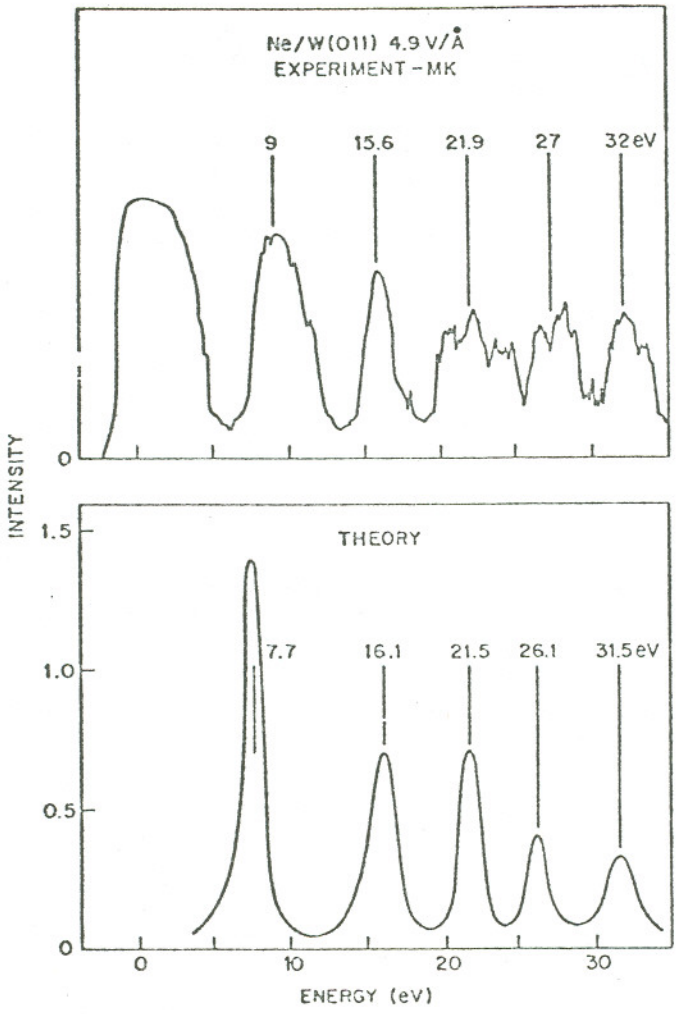

Figure 7

Reproduced from Ref. 7. This shows the excellent agreement between experiment and the calculations of Appelbaum and McRae.

the ionization rate.[8,9] A theoretical explanation of this effect was proposed by Nolan and Herman.[10,11]

Nolan and Herman found that if the field ionization rate was calculated by means of time dependent perturbation theory, then the rate was enhanced by the overlap of the adsorbed gas atomic wavefunctions (orbitals) with those of the atom to be ionized. The ionization rate is proportional[12] to $|\langle i|H|K\rangle|^2$ where $|i\rangle$ represents the electron wavefunctions in the metal and the wavefunction of the electron in the atom to be ionized. $|K\rangle$ represents the metal with one extra electron and the atom with one less electron. If there is an adsorbed atom taking part in the process, $|i\rangle$ and $|K\rangle$ must include its wavefunctions and H must include the interaction of ad-atom and atom to be ionized, as well as the usual image potentials and field terms.

When the matrix element was evaluated it turned out to have the form $\langle i|H|K\rangle \approx \langle U|h|K\rangle - \sum_i \langle U|U_{A_i}\rangle\langle U_{A_i}|h|K\rangle$, where U is the atom wavefunction and U_{A_i} an ad-atom wavefunction. If no ad-atom is present, $\langle i|H|K\rangle \approx \langle U|h|K\rangle$ (h is the single-electron Hamiltonian). If the overlap integrals $\langle U|U_{A_i}\rangle$ are significant, $|\langle i|H|K\rangle|^2$ may be larger than for the case when there is no ad-atom. Nolan and Herman found that, by using wavefunctions which take into account the effect of the field on the atomic orbital, they were able to predict enhancement effects for adsorbed Ne and He when the ionized atoms were He, the ratio of which agreed with experiment to within about 20%.

D. Gas Supply Mechanisms

The ion current from a field ion source is the product of the ionization rate by the supply of gas atoms available to be ionized. The supply (i.e., rate at which atoms reach the emitter) is a complicated function of emitter shape applied voltage, and emitter temperature. Because of the factor $[I - 1.22 \times 10^{-23} F^{1/2}]^{1/2}/F$ in the exponent of the equation for D, the probability of ionization rises very quickly with increasing field. Experimentally it is known that at sufficiently high fields all the gas atoms are ionized before reaching the emitter, so the supply of gas will determine the current. At very low fields the number of atoms impinging on the emitter greatly exceeds the number ionized. At intermediate field strengths the situation is complex.[13]

Consider an H atom in the vicinty of a radial electric field $F = \frac{e}{4\pi\epsilon_o r^2}$. If we imagine the electron bound to the proton by a harmonic oscillator potential (that is, a spring of constant K) then the field will induce a dipole moment: the electron is attracted by a force $\frac{-e^2}{4\pi\epsilon_o r^2}$ and the proton repelled by a force $\frac{e^2}{4\pi\epsilon_o r^2}$. The particles separate until $KX = \frac{e^2}{2\pi\epsilon_o r^2}$, where X is the separation. The induced dipole is $eX = \frac{2e^2}{K} F$, and $X = \frac{2e}{K}F$. The potential energy of the atom in the field due to the force on the dipole is $V = \frac{e^2}{4\pi\epsilon_o\left(r + \frac{X}{2}\right)} - \frac{e^2}{4\pi\epsilon_o\left(r - \frac{X}{2}\right)} = \frac{-e^2X}{4\pi\epsilon_o r^2} = -\frac{1}{2}\alpha F^2$, where $\alpha = \frac{4e^2}{K}$ is the polarizability. The force on the atom is $\frac{-\partial V}{\partial r} = \alpha F \frac{\partial F}{\partial r}$.

In the absence of any field the number of atoms striking the tip of the emitter per second can be easily calculated from kinetic theory: $N = \frac{P \times A}{\sqrt{2\pi mKT}}$, where P is the gas pressure and A the area of the tip. When the field is turned on the pressure rises: from the Maxwell-Boltzmann (M-B) distribution the density of a gas is $n = n_o \exp\left(-\frac{V}{kT}\right)$ and the pressure $P = P_o \exp\left(-\frac{V}{kT}\right)$. $V = -\frac{1}{2}\alpha F^2$ can be very much larger than kT at high fields. For example for H, $\alpha = 6.7 \times 10^{-41}$ coulomb^2 - meters^2 joule. If F = 2 volts/Å and T = 300 K, $p = p_o e^{+3.21} \approx 25\, p_o$. Thus the supply of atoms to be ionized will be significantly increased by the action of the field. This calculation is only a rough estimate because the field is not actually radial. A more accurate estimate would require the integration of the actual field from infinity up to the emitter, and would have to take into account the initial thermal kinetic energy (see below).

At the same time, the kinetic energy of the impinging atoms will be greatly increased so that they will pass through the region of high ionization probability in a very short time. Since the probability of ionization is proportional to the time spent in this region, this works against the desired end of high current. The problem comes down to the interaction of the impinging atoms with the emitter surface - if incoming atoms rebound and retain most of their energy, the probability of ionization will be about the same on the way out as on the way in, and the atoms will in general be lost to the

ionization region. If, on the other hand, the atoms lose a significant portion of their energy i.e., "accommodate," upon colliding with the emitter they may not escape at all, being held by the polarization force α F $\frac{\partial F}{\partial r}$, and the probability of ionization will be greatly increased.[13,14]

The physical process which takes place is that the supply of molecules is increased by polarization forces which attract them to the emitter tip and to the emitter shank, where the field is lower. The molecules arrive at the ionization region from the gas phase and by diffusing up the emitter shank. The supply is decreased primarily by rebounds, and by diffusion of unaccommodated molecules away from the ionization region. Those molecules which diffuse to the ionization region from the shank will by then be thermally accommodated to the emitter temperature while those which initially strike the tip of the emitter will not, because of their large kinetic energy due to the polarization force.

The supply of molecules available is the result of a balance between diffusion into and out of the ionization region, the arrival of molecules from the gas phase and the removal due to ionization. The process depends strongly on the emitter temperature which determines the diffusion rates, energies of diffusion, molecular polarizability and mass, and the electric field of strength.

A thorough treatment of the gas dynamics problem was published in 1970 by Van Eekelen.[15] He was able to predict many of the features of the FI process with fairly good agreement with experiment. The

treatment is fundamental enough that it should be studied in the original.

Briefly, the method consists of approximating the emitter shape by a hyperboloid of revolution and then confining attention to the region within about ± 5° of the axis so the θ variation of the field can be ignored. The field is then approximated by $F = \frac{V}{\kappa} \frac{1}{2r-r_{tip}}$ and supply by diffusion from the emitter shanks is ignored. With this approximation the supply function S was calculated by assuming a M-B distribution for the gas molecules momenta, as modified by the polarization energy and taking into account the conservation of energy and angular momentum (see also reference 16). This method implicitly assumes that the number of molecules which are ionized is small compared with the total supply so that the M-B distribution is valid. It turns out that the region of space which contributes most importantly to the supply is relatively far from the tip, $r \sim 3r_{tip}$, where ionization would take place only for extremely high fields. Since this case is of little practical interest (the tip will begin to field evaporate at $F \sim 6$ V/Å) the results prove to be accurate in the experimentally accessible regime.

The results were that the supply and hence current are enhanced by a factor $\sigma = 1 + \phi + 2.7\phi^{1/3} + 2.7\phi^{2/3}$ where $\phi = \frac{1}{2} \alpha F^2_{tip}/kT$. The original supply calculation by Southon[16] for a spherical tip yielded $\sigma = (\pi\phi)^{1/2}$ and does not fit the experimental data as well as the new result. The variation of σ with α for constant F is shown in Fig. 8.

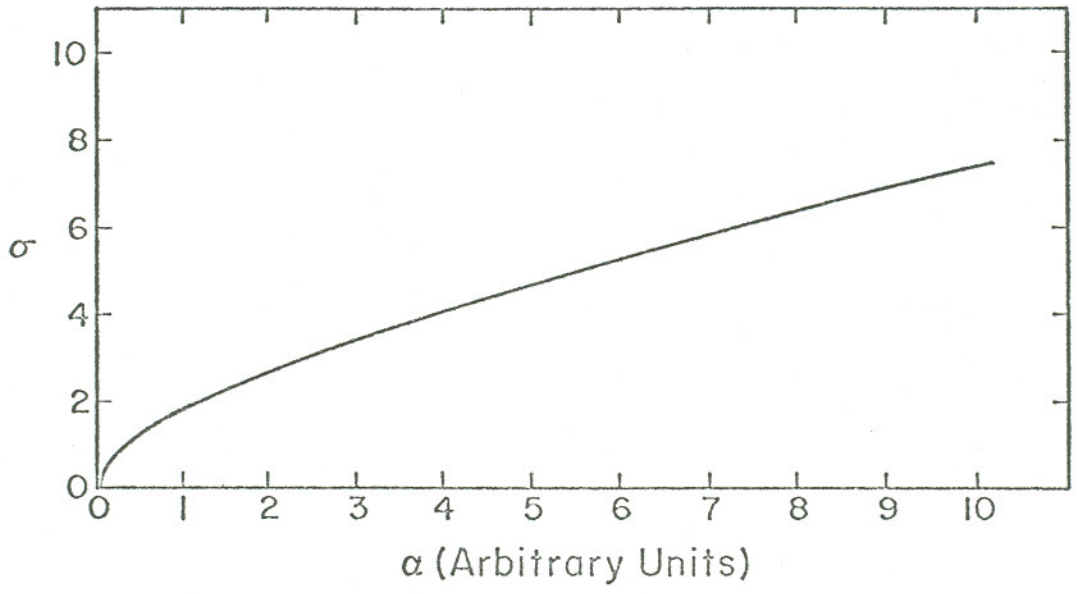

Fig. 8

These results were reproduced by another method[15] which also provides additional insight into the ionization rate dynamics. This method consists of setting up a dynamical equation for the interaction of the incoming gas molecule and the emitter tip, the latter approximated by a box of non-interacting metal atoms. The gas molecules transfer momentum to the metal atoms in a highly temperature dependent way and are generally captured by the polarization force. The dynamical equation describes the collision and takes into account the probability D of ionization (due to the field as given above) each time the molecule passes through the ionization region as it bounces around the tip. The equation was solved by an iteration procedure on a digital computer to yield ionization rates

(current) for several gas species as a function of α, emitter temperature, gas temperature and electric field.

Van Eekelen was able to show good agreement with experiment for calculations of current as a function of field and temperature, the extent to which accommodation precedes ionization, concentration of gas at the tip surface and current from individual spots where the field over a protrusion is enhanced. The results were not very sensitive to changes in work function or width of ionization zone.

Perhaps the most interesting result was that the concentration of atoms at the tip goes through a maximum as the field increases, and then drops off quite rapidly. This is due to the increase in energy $\frac{1}{2}\alpha F^2$ of the atoms which results in decreased accommodation. This means that the relative currents for atoms with different polarizabilities will not necessarily be proportional to the ratio of the polarizabilities unless the field is so high that the current equals the supply (ionization in free space far from the tip). Atoms with very large polarizabilities may gain so much kinetic energy that by the time the field is high enough to allow a reasonably large probability for ionization the accommodation is poor. In this case there will be a smaller current than would be expected for high polarizability molecules.

There are atomic and molecular species which, at appropriate temperatures and fields are supplied to the emitter tip by other mechanisms. In particular, films can form on the emitter that greatly

increase the FI current. For example, Jason et al[17] measured hydrogen ion currents at 4.2 K and 2×10^{-7} torr which were in excess of the current measured at 10^{-3} torr with the same field but at higher temperatures. The additional supply of hydrogen came from diffusion of condensed films up the emitter shank. It was observed that the hydrogen would diffuse up the shank until it reached a point where the ionization probability D was high and the most of it would be ionized. The appearance of the emitter in a FI microscope was a bright ring of emission which expanded as the field was increased and the ionization region moved down the shank. Further evidence that the supply came from a film was that the field necessary to ionize the hydrogen was only about one half that needed for gas phase ionization, which indicated a very long dwell time of the molecules in the ionization region (as compared with the dwell time of incoming gas molecules).

In the case of field ionization of water, mass spectrometric observations show that the FI process can be very complex because of the high pressures due to the permanent dipole moment of the water molecule. Anway[18] found that water would condense on the emitter forming thick layers which would profoundly affect the ionization rate. The layers could build up to the critical distance $x_c = (I - \phi)/eF$ and cause tremendous increases in current because of the long dwell time of the molecules. Under appropriate conditions the thickness could exceed x_c and the decrease in field at a given

voltage which resulted would reduce the current drastically. The current - voltage characteristics for water showed considerable "hysteresis," i.e., depended very much on whether the voltage was being raised or lowered. Complex mass spectra for the ionized water show $H_3O^+ \cdot nH_2O$ where n can range from 0 to 3 at 300 K and up to 9 at dry ice temperature (195 K). Observations in this laboratory have shown that at 300 K considerable water ion current can be seen if the background pressure is 10^{-6} - 10^{-5} torr. This current disappears entirely at 77 K, as all the water vapor freezes out.

E. Angular Distributions

Goldenfeld and Nazarenko[19] have calculated the angular distribution of organic ions when the supply is from the gas phase. They approximated the emitter shape by paraboloids and hyperboloids of revolution and folded together the effects of increasing emitter area and decreasing field as the angle of emission increase ($\theta = 0$ along the axis). The results were that as the field increased the maximum of the angular distribution moved outwards from $\theta = 0$ and that the peak emission could be several times the emission along the axis. Calculations were performed for several organic molecules and agreed qualitatively with measurements made by the authors. For example, the enhancement of hexane ion current at large angles ($\theta = 50° - 60°$) was predicted to be 2 - 3. Experimentally the enhancement was found to be somewhat larger at lower angles: 2 - 4 at $\theta = 30° - 40°$.

The calculations assumed smooth emitters. Angular effects due to emitter non-homogeneities in the radius can be expected to play a very large role in the determination of angular distributions, as they do in field electron emission.[20]

APPENDIX 1

The WKB barrier penetration probability may be calculated[21,22,23] as follows (refer to Fig. 2 of main text).

The Schrödinger equation for the electron is

$$\frac{d^2\psi}{dx^2} + k^2\psi = 0 \tag{1}$$

where

$$k = \frac{\sqrt{2m(E-V)}}{\hbar} = \frac{mv}{\hbar}$$

v being the classical velocity of the particle. Let $\psi = e^{i\,S(x)}$. Then equation (1) becomes

$$i\,\frac{d^2S}{dx^2} - \left(\frac{dS}{dx}\right)^2 = -k^2 \tag{2}$$

This is an exact equation. In the first approximation let $\frac{dS}{dx} = \pm\, k$, i.e., let

$$\left|\frac{\frac{d^2S}{dx^2}}{\left(\frac{dS}{dx}\right)^2}\right| = \left|\frac{\frac{dk}{dx}}{k^2}\right| << 1. \quad \text{Then } S = \pm \int k\,dx \text{ and } \psi_{WKB} = e^{\pm\, i\int k\,dx}.$$

A better approximation is to let $\frac{dS}{dx} = \pm\,(k + \epsilon)$, where ϵ is a small correction and terms in ϵ^2, $\frac{d\epsilon}{dx}$ etc. are ignored. The Schrödinger equation then becomes

$$k^2 + \epsilon^2 + 2\epsilon k - i\,\frac{dk}{dx} = k^2 \tag{3}$$

or, neglecting ϵ^2, $k + 2\epsilon - \frac{i}{k}\frac{dk}{dx} = k$ and

$$\epsilon = \frac{ik'}{2k}\,. \tag{4}$$

Then

$$\frac{dS}{dx} = \pm\left(k + i\,\frac{\frac{dk}{dx}}{2k}\right) \tag{5}$$

so that

$$S = \pm \int k dx \pm \frac{i}{2} \ln k + \text{const.}$$

and

$$\psi_{WKB} = \frac{\text{const}}{\sqrt{k}} e^{\pm i \int k dx} \tag{6}$$

or

$$\psi_{WKB} \sim \frac{1}{\sqrt{k}} \sin [\int k dx + \phi] \tag{7}$$

where ϕ = const. If $E < V$ k is imaginary, $k = i\kappa$ where

$\kappa = \frac{\sqrt{2m(V-E)}}{\hbar}$ and $\psi_{WKB} \sim \frac{1}{\sqrt{i\kappa}} e^{\pm \int k dx}$, i.e., ψ_{WKB} is either increasing or decreasing exponentially.

The WKB approximation breaks down at $x = x_o$ and $x = x_c$, for at these points $E - V \to 0$, $k \to 0$ and the Schrödinger equation must be solved either exactly or by means of a different approximation which remains valid at x_o and x_c. One method consists of expanding k^2 about the singular points. Let x_o stand for x_o or x_c.

$$k^2 = A^2(x - x_o) + B^2(x - x_o)^2 + \ldots. \tag{8}$$

Retaining only the first term the Schrödinger equation is

$$\frac{d^2\chi}{dx^2} + A^2 (x - x_o)\chi = 0 \tag{9}$$

Let $y = A^{\frac{2}{3}} (x - x_o)$. Equation 9 is then $\frac{d^2\chi}{dy^2} + y\chi = 0$, with solutions

$$\chi_{\pm} = C_{\pm} \sqrt{x - x_o}\, J_{\pm \frac{1}{3}} \tfrac{2}{3} A (x - x_o)^{\frac{3}{2}} \quad (C_{\pm} \text{ are constants}). \tag{10}$$

As $x \to x_o$ the WKB solutions must approach eqns. (10) or a linear combination of them. If instead of $\frac{2}{3} A (x - x_o)^{\frac{3}{2}}$ we use $w = \int_{xo}^{x} k dx$ $= \int A(x - x_o)^{\frac{1}{2}} dx$ we have a variable which can replace $\int k dx$ in the WKB

solutions eqn. (7) and which approaches $\frac{2}{3} A(x - x_o)^{\frac{3}{2}}$ as $x \to x_o$.

For large x

$$J_{\frac{1}{3}} \to \sqrt{\frac{2}{\pi w}} \cos\left(w - \frac{5\pi}{12}\right) \tag{11}$$

$$J_{-\frac{1}{3}} \to \sqrt{\frac{2}{\pi w}} \cos\left(w - \frac{\pi}{12}\right)$$

For large x a combination of χ_+ and χ_- with proper coefficients must approach the WKB solutions: let $\Phi = \sqrt{\frac{w}{k}}\,[A\, J_{\frac{1}{3}}(w) + B\, J_{-\frac{1}{3}}(w)]$. As x becomes large,

$$\Phi \to \sqrt{\frac{2}{\pi}}\ \frac{1}{\sqrt{k}} \left[A \cos\left(\int_{x_c}^{x} k dx - \frac{5\pi}{12}\right) + B \cos\left(\int_{x_c}^{x} k dx - \frac{\pi}{12}\right)\right] \tag{12}$$

For $x > x_o$ the WKB solution is an outgoing wave

$\psi_{WKB} \sim \frac{1}{\sqrt{k}}\, e^{\pm i \int k dx} + \text{const}$ and $w = \int_{x_o}^{x} k dx$. Since the electron is moving away from the origin we choose the constant to be $-\frac{\pi}{4}$, for convenience

$$\psi_{WKB} \sim \sqrt{\frac{2}{\pi}}\ \frac{1}{\sqrt{k}}\, e^{i\left(\int_{x_o}^{x} k dx - \frac{\pi}{4}\right)} . \tag{13}$$

Some algebra shows that if in the definition of Φ we choose

$$A = \frac{2e^{-\frac{2}{3} i\pi}}{e^{-\frac{5}{6} i\pi} - e^{-\frac{i\pi}{6}}}\ , \quad B = -\, e^{+\frac{i\pi}{3}} A, \tag{14}$$

then $\Phi \to \psi_{WKB}$ for large x. This connects ψ_{WKB} with the exact solution at x_o.

When $x_c < x < x_o$ k is imaginary and so $w = \int k dx$ is also. Let $k = i|k| = e^{\frac{i\pi}{2}}|k|$. Then, since $w \to \frac{2}{3} A(x - x_o)^{\frac{3}{2}}$, w must equal $-i|w| = e^{\frac{i3\pi}{2}}|w|$. By using the asymptotic values of $J_{\pm\frac{1}{3}}$ the asymptotic form for Φ is then found to be

$$\Phi \to \sqrt{\frac{2}{\pi}} \frac{1}{\sqrt{k}} \left[e^{\frac{5i\pi}{6}} A \cos\left(-i|w| + \frac{5\pi}{12}\right) + e^{\frac{i\pi}{6}} B \cos\left(-i|w| + \frac{\pi}{12}\right)\right]$$

$$= \frac{1}{2}\sqrt{\frac{2}{\pi k}} \left[(B-A)e^{|w|} + \left(Ae^{\frac{i\pi}{6}} + Be^{-\frac{i\pi}{6}}\right) e^{-|w|} e^{\frac{i\pi}{4}}\right] \qquad (15)$$

Unless A = B the term involving $e^{-|w|}$ can be ignored. With A and B from (14) Eqn. (15) becomes $\Phi \to \sqrt{\frac{2}{\pi k}}\, ie^{|w|}$.

When $x < x_o$, i.e. in the region $x_c < x < x_o$, let $w' = \int_x^{x_c} k dx$. Then $|w'| = -|w| + \int_{x_c}^{x_o} |k| dx$, as can be seen by examining the intervals of integration on the x-axis. Denoting $\int_{x_c}^{x_o} |k| dx$ by τ and $|w| = -|w'| + \tau$ the asymptotic form of Φ becomes

$$\Phi \to \sqrt{\frac{2}{\pi k}}\, i\, e^{-|w'|} e^{\tau} \qquad (16)$$

When $x < x_o$ we can also write the asymptotic form for Φ as we did in Eqn. (15) with w replaced by w', and A and B replaced by new constants A' and B':

$$\Phi \to \frac{1}{2}\sqrt{\frac{2}{\pi k}} \left[(B'-A')\, e^{|w'|} + \left(A'e^{\frac{i\pi}{6}} + B'e^{-\frac{i\pi}{6}}\right) e^{-|w'|}\right]$$

comparison with (16) shows $A' = B'$ and $\frac{1}{2} A' \left(e^{\frac{i\pi}{6}} + e^{-\frac{i\pi}{6}}\right) = ie^{\tau}$, or

$A' \cos\left(\frac{\pi}{6}\right) = ie^{\tau}$ in order that $\Phi \to \sqrt{\frac{2}{\pi k}}\ ie^{\tau}\ e^{-|w'|}$.

Since $\psi_{WKB} \to \Phi$, for $x_c < x < x_o$

$$\psi_{WKB} = \sqrt{\frac{2}{\pi k}}\ ie^{-|w'|}e^{\tau}. \tag{17}$$

We must now look at the region $x < x_c$ and match the wavefunctions at x_c. For $x < x_c$

$$\Phi \to \sqrt{\frac{2}{\pi k}}\ \left[A'' \cos\left(w' - \frac{5\pi}{12}\right) + B'' \cos\left(w' - \frac{\pi}{12}\right)\right] \text{ (see Eqn. (12).}$$

Since this must match smoothly to Φ at x_c, $A'' = ie^{\tau} \div \cos\ \frac{\pi}{6}$ $= B''$, i.e.,

$$\Phi \to \sqrt{\frac{2}{\pi k}}\ \frac{ie^{\tau}}{\cos\ \frac{\pi}{6}}\ \left[\cos\left(w' - \frac{5\pi}{12}\right) + \cos\left(w' - \frac{\pi}{12}\right)\right].$$

For $x < x_c$, ψ_{WKB} consists of an outgoing portion incident on the barrier and an incoming portion reflected from the barrier:

$$\psi_{WKB} \sim \sqrt{\frac{2}{\pi k}}\ \left[\alpha e^{i\left(w' - \frac{\pi}{4}\right)} + \beta\, e^{-i\left(w' - \frac{\pi}{4}\right)}\right].$$

Matching this to Φ we find

$$\alpha e^{iw'} e^{-\frac{i\pi}{4}} + \beta\, e^{-iw'} e^{\frac{i\pi}{4}} = \frac{1}{2}\frac{ie^{\tau}}{\cos\ \frac{\pi}{6}}\ \left[e^{iw'} e^{-\frac{5i\pi}{12}} + e^{-iw'} e^{\frac{5i\pi}{12}} + e^{iw'} e^{-\frac{i\pi}{12}} + e^{-iw'} e^{\frac{i\pi}{12}}\right]$$

so $\alpha = \beta = ie^{\tau}$, and for $x < x_c$

$$\psi_{WKB} \sim \sqrt{\frac{2}{\pi k}}\ ie^{\tau}\ \left[e^{i\left(w' - \frac{\pi}{4}\right)} + e^{-\left(w' - \frac{\pi}{4}\right)}\right] \tag{18}$$

The flux of particles is given by $k|\psi|^2$. Taking the ratio of the fluxes for $x > x_o$ and $x < x_c$ we have, from equations (13) and (18),

the ratios of $k|\psi_{WKB}|^2$ for $x < x_c$ and $x > x_o$:

$$D = \text{Ratio} = \frac{k_{out}\left|\sqrt{\frac{2}{\pi k}}\; e^{i\left(w - \frac{\pi}{4}\right)}\right|^2}{k_{in}\left|\sqrt{\frac{2}{\pi k}}\; i\, e^{\tau}\, e^{i\left(w' - \frac{\pi}{4}\right)}\right|^2} = e^{-2\tau} \qquad (19)$$

This is the WKB probability for barrier penetration, i.e., ionization. Note that in the denominator of equation (19) only the outgoing wave appears. The important quantity is

$$\tau = \left|\int_{x_c}^{x_o} k\,dx\right| = \sqrt{\frac{2m}{\hbar}}\left|\int_{x_c}^{x_o}\sqrt{E-V}\;\;dx\right| = \sqrt{\frac{2m}{\hbar}}\int_{x_c}^{x_o}\sqrt{V-E}\;\;dx \qquad (20)$$

so we must calculate this integral to find the ionization probability.

At the temperature encountered in field ionization work, $T \leq 300$ K typically, the energy levels below the Fermi energy are almost totally full - the fraction of electrons with energies 1% greater than E_F is

$$\left[1 + e^{\frac{0.01 \times 10^5}{77}}\right]^{-1} = 0.02\% \text{ at } LN_2 \text{ temperature.}$$ This means that

there is a critical distance[2] for field ionization, inside which it does not take place. As the atom approaches the emitter the level of its ground state approaches the Fermi level and once below that level, the electron cannot be accepted by the metal and ionization cannot take place. A graph of the energy near an emitter clarifies this, as shown in the schematic diagram of Fig. 1A on the following page.

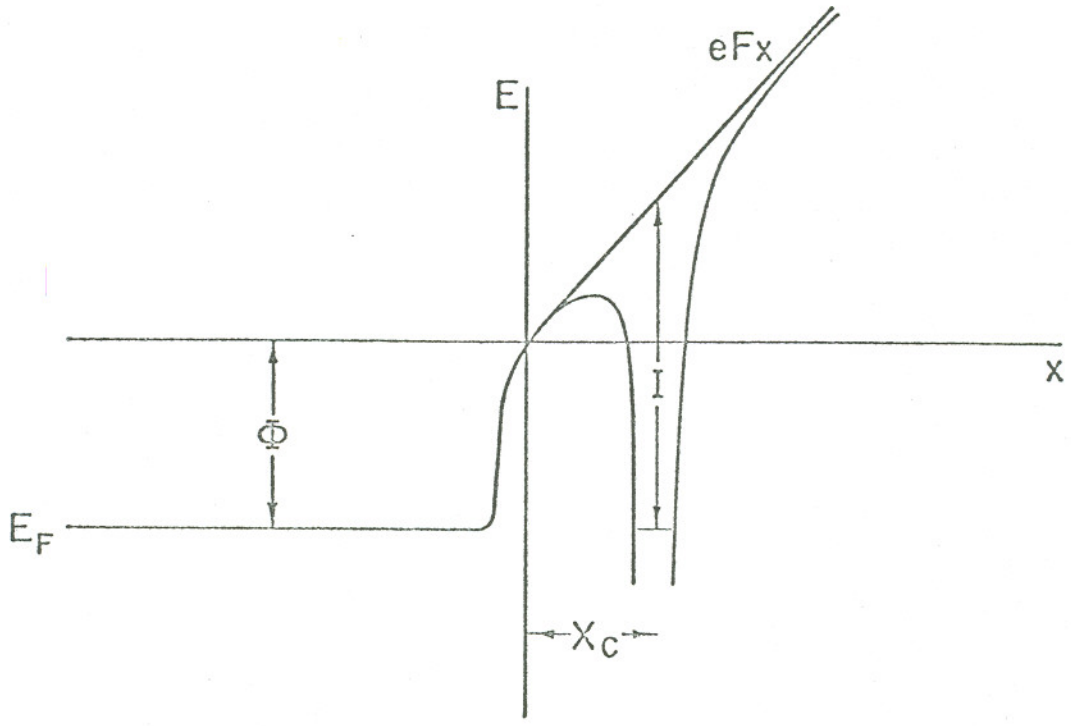

Fig. 1A

The transition of the potential from vacuum to metal ($x < 0$) is schematic. Φ = work function.

From Fig. 1A it is evident that the ground state of the atom is at the level of E_F when $eFx_c = I - \Phi$, or $x_c = \frac{I - \Phi}{eF}$, assuming I is the same as the atom in field free space, which it very nearly is.

We now know that the minimum width of the barrier for which ionization is possible is x_c. When the ionization probability is calculated we will see that it falls very quickly for $x > x_c$, so x_c may be used as the barrier width in general. For I = 13.5 eV, Φ = 5 eV

and F = 2 V/Å, x_c = 4.3 Å. It has been found experimentally[3] that, if the field is not too strong, almost all the ionization takes place within 0.2 Å of x_c.

The approximation used[2] for the potential of the electron (in one dimension) is:

$$V(x) = \frac{-e^2}{4\pi\varepsilon_o|x_i-x|} + eFx - \frac{e^2}{16\pi\varepsilon_o x} + \frac{e^2}{4\pi\varepsilon_o(x_i+x)} \qquad (21)$$

The integral in equation (20) can be approximated[2] by a triangle whose base is x_c and whose altitude is a = [Φ plus V at the point where $\frac{\partial V}{\partial x} = 0$]$^{1/2}$. The contributions to V by the third and fourth terms of (21) are each ~ five times smaller than the first two terms and roughly cancel each other. Taking $V(x) \approx \frac{-e^2}{4\pi\epsilon_o|x_i-x|} + eFx$ we find $\frac{\partial V}{\partial x} = 0$ at $x_i - x = \sqrt{\frac{e}{4\pi\epsilon_o F}}$. The value of V(x) at this point is

$$V(x) = -2\sqrt{\frac{e^3F}{4\pi\epsilon_o}} + eFxi \qquad (22)$$

When $x_i = x_c = \frac{I-\Phi}{eF}$ Eqn. (22) becomes

$$V(x) = -2\sqrt{\frac{e^3F}{4\pi\epsilon_o}} + I - \Phi \qquad (23)$$

and the height of the barrier $[V(x) + \Phi]^{1/2}$ is $a = \left[I - 2\sqrt{\frac{e^3F}{4\pi\epsilon_o}}\right]^{1/2}$.

The integral $\tau = \sqrt{\frac{2m}{\hbar}} \int_{x_c}^{x_o} \sqrt{V-E}\, dx$ is then approximately given by $\sqrt{\frac{2m}{\hbar}} \times$ area of triangle $= \sqrt{\frac{2m}{\hbar}} \frac{1}{2} x_c \left[I - 2\sqrt{\frac{e^3F}{4\pi\epsilon_o}}\right]^{1/2}$

$= \sqrt{\frac{2m}{\hbar}} \frac{(I-\Phi)}{2eF} \left[I - 2\sqrt{\frac{e^3F}{4\pi\epsilon_o}}\right]^{1/2}$. The probability of ionization

$D = e^{-2\tau}$, is then

$$D = e^{-\sqrt{\frac{2m}{\hbar}}\ \frac{(I-\Phi)}{eF}\ \left[I - 2\sqrt{\frac{e^3F}{4\pi\epsilon_o}}\right]^{1/2}} \tag{24}$$

or

$$D = e^{-16\ \times 10^{37}\ \frac{(I-\Phi)}{F}\left[\left(I - 1.22 \times 10^{-23}\sqrt{F}\right)\right]^{1/2}} \tag{25}$$

For an H atom (I = 13.5 eV) and an Ir emitter (Φ = 5.3 eV) with a field of F = 2 V/Å, $D \approx e^{-6.9} = 10^{-3}$. This is the probability the electron will penetrate the barrier.

APPENDIX 2

Boudreaux and Cutler[4] set up the Schrödinger equation to calculate the energy distribution for field ionization as follows. The system is {tip + electron and ion} with an interaction potential between the ion and the tip approximated by an image potential:

$$\left\{-\left(\frac{\hbar^2}{2M}\right)\nabla_\rho^2 + H_c(\vec{r}_c) + U(\vec{r}_c, \vec{\rho})\right\}\psi(\vec{r}_c, \vec{\rho}) = \left\{\frac{1}{2}M'V'^2 + E_f^{\alpha}\right\}\psi(\vec{r}_c\vec{\rho}). \quad (1)$$

Here $\vec{\rho}$ is the separation between tip and ion, $\vec{r}_c$ are the internal variables for the electrons in the tip, H_c is the Hamiltonian of the electrons in the tip, $U(\vec{r}_c, \vec{\rho})$ is the interaction potential, $1/2\ M'V'^2$ is the kinetic energy of the ion immediately after the collision and E_f^{α} the energy of the electrons in the metal in the ground state configuration plus one electron in the state α above the Fermi level (this represents the electron which has just tunneled into the tip). This equation is solved by expanding the wave function in terms of a complete set of eigenfunctions $\phi_\mu(\vec{r}_c)$ representing the state of the emitter after the collision and $\beta_\mu(\vec{\rho})$ representing the outgoing ion: $\psi(\vec{r}_c, \vec{\rho}) = \sum_\mu \beta_\mu(\vec{\rho})\ \phi_\mu(\vec{r}_c)$. Substituting this into the Schrödinger equation, multiplying by $\phi_\alpha^*(\vec{r}_c)$ and integrating over the variables $\vec{r}_c$ leaves the equation

$$\left\{\nabla_\rho^2 + K'^2_\alpha\right\}\beta_\alpha(\vec{\rho}) = \frac{2M'}{\hbar^2}\int \phi_\alpha^*(\vec{r}_c)\ U(\vec{r}_c,\vec{\rho})\psi(\vec{r}_c,\vec{\rho})\ d\vec{r}_c \quad . \quad (2)$$

This equation was solved for $\beta_\alpha(\vec{\rho})$, which are wavefunctions for the outgoing ions, by constructing the Green's function for the equation

$$(\nabla_\rho^2 + K_\alpha'^2)G(\vec{\rho}|\vec{\rho}) = \delta(\vec{\rho} - \vec{\rho}') , \tag{3}$$

which is

$$G(\vec{\rho}|\vec{\rho}') = \frac{e^{iK_\alpha' |\vec{\rho} - \vec{\rho}'|}}{4\pi|\vec{\rho} - \vec{\rho}'|} , \tag{4}$$

and integrating:

$$\beta_\alpha(\vec{\rho}) = \frac{2M'}{\hbar^2} \int d\rho' \int G(\vec{\rho}|\vec{\rho}')\phi_\alpha^* (\vec{r}_c)U(\vec{r}_c,\vec{\rho})\psi(\vec{r}_c,\vec{\rho})d\vec{r}_c , \tag{5}$$

where $|K_\alpha'|^2 = \frac{2M'}{\hbar^2} \times \frac{1}{2} M'V'^2$.

Since the wavefunctions $\beta_\alpha(\vec{\rho})$ representing the outgoing ion must have the form

$\beta_\alpha(\rho) \underset{\rho \to \infty}{\longrightarrow} \frac{e^{iK_\alpha'\rho}}{\rho} f_\alpha(\theta, \phi)$ (outgoing spherical wave), and since

$G(\vec{\rho}|\vec{\rho}') \underset{\rho \to \infty}{\longrightarrow} \frac{e^{iK_\alpha'\rho}}{4\pi\rho} e^{-i\vec{K}_\alpha' \cdot \vec{\rho}'}$, the function

$$f_\alpha(\theta,\phi) = \frac{2M'}{4\pi\hbar^2} \int d\rho \int \phi_\alpha^*(\vec{r}_c)\, U(\vec{r}_c,\vec{\rho})\, e^{i\vec{K}_\alpha' \cdot \vec{\rho}}\, \psi(\vec{r}_c,\vec{\rho})d\vec{r}_c \tag{6}$$

$f(\theta, \phi)$ is the scattering amplitude, so the scattering cross section is $\frac{d\sigma}{d\omega} = |f(\theta, \phi)|^2$ and the total scattering cross section for a collision leaving the electron in state α is $\sigma_\alpha^T = \int \frac{d\sigma}{d\omega} d\omega = \int |f(\theta, \phi)|^2 d\omega$.

If σ_α^T is summed over all states α the total cross section is $\sigma^T = \int \sigma_\alpha^T N(E_\alpha) dE_\alpha$, where $N(E_\alpha)$ is the density of states.

In order to calculate the integral, the Born approximation was used:

$$\psi(\vec{r}_c, \vec{p}) \approx \frac{e^{i\vec{K}_o \cdot \vec{\rho}} \psi_o(\vec{r}_c)}{\sqrt{\Omega}}$$

$1/\sqrt{\Omega}$ is a normalization factor, $K_o^2 = \frac{M^2V^2}{\hbar^2}$, and $\psi_o(\vec{r}_c)$ is the product of the wave function of the electron in the atom before ionization with the wave function of the electrons in the metal. The approximation assumes $\psi(\vec{r}_c, \vec{\rho})$ doesn't change much during the collision.

With this approximation σ_α^T was reduced to an integral that could be evaluated numerically, and which is proportional to K_α^{-8} $\left(K_\alpha^2 = \frac{2mE_\alpha}{\hbar^2}\right)$. Then $\sigma^T = \int \sigma_\alpha^T N(E_\alpha)\, dE_\alpha \sim K_\alpha^{-7}\, \epsilon^{-1/2}$, where

ϵ = energy of incoming atom.

REFERENCES

1. J. R. Oppenheimer, Phys. Rev. 13, 66 (1928).

2. E. W. Müller, Ad. in Elect. and Elect. Phys. Vol. XIII, 1960.

3. E. W. Müller and T. T. Tsong, J. Chem. Phys. 41, 3279 (1964).

4. D. S. Boudreaux and J. H. Cutler, Phys. Rev. 149, 170 (1966).

5. A. J. Jason, R. P. Burns, and M. G. Ingraham, J. Chem. Phys. 43, 3762 (1965).

6. A. J. Jason, Phys. Rev. 156, 266 (1967).

7. J. A. Appelbaum and E. G. McRae, Surf. Sci. 47, 445 (1975).

8. K. Rendulic, Surf. Sci. 28, 285 (1971).

9. K. Rendulic, Surf. Sci. 34, 581 (1973).

10. D. A. Nolan and R. M. Herman, Phys. Rev. B8, 4099 (1973).

11. D. A. Nolan and R. M. Herman, Phys. Rev. B10, 50 (1974).

12. R. H. Dicke and J. P. Wittke, "Introduction to Quantum Mechanics," Addison-Wesley, Ch. 14.

13. R. Gomer, "Field Emission and Field Ionization," Harvard University Press.

14. E. W. Müller, J. App. Phys. 28, 1 (1957).

15. H. A. M. Van Eeklen, Surf. Sci. 21, 21 (1970).

16. M. J. Southon, Ph.D. Thesis, 1963, University of Cambridge (unpublished). Results are quoted in E. W. Müller and T. T. Tsong, "Field Ion Microscopy Principles and Applications," Elsevier.

17. A. Jason, B. Halpern, M. G. Ingraham and R. Gomer, J. Chem. Phys. 52, 2227 (1970).

18. A. R. Anway, J. Chem. Phys. 50, 2012 (1969).

19. I. V. Goldenfeld and V. A. Nazarenko, Int. J. Mass. Spect. 5, 197 (1970).

20. L. W. Swanson and L. C. Crouser, J. Appl. Phys. 40, 4741 (1969).

21. P. M. Morse and H. Feshbach, Methods of Theoretical Physics, Vol. II, McGraw Hill Co.

22. E. Fermi, Notes on Quantum Mechanics, University of Chicago Press.

23. A. Messiah, Quantum Mechanics, Vol. I, John Wiley & Sons.

IV. EXPERIMENTAL PROCEDURE AND RESULTS

A. FI Gun Development

Two FI sources were built, one for use on an optical bench and the other on a high vacuum system. In each case the emitter was surrounded by a Mo cylinder (cathode cap) $\approx$ 1.5 cm in diameter with a thin aperture of 0.5 or 1.0 mm diameter at one end through which the ion beam was extracted. The aperture also served as a pumping port for the dynamic gas supply.[1] Hydrogen (H_2) was chosen as the gas for these experiments because it requires a field of $\approx$ 2.2 V/Å to ionize efficiently, which is similar to or higher than what is required for other gases such as Ar, N_2, O_2, Xe, and because it is not capable of causing significant sputtering damage at the energies encountered here (10 - 20 keV).

The high vacuum study was performed in a glass field ion microscope designed so the incoming gas would be pre-cooled by LN_2 used to cool the emitter. The Mo cathode cap containing the beam aperture fit tightly around the glass LN_2 reservoir and was cooled by it. The configuration of the source was such that gas molecules made many collisions with the walls before escaping through the aperture, thus ensuring that the gas supply to the emitter would be at LN_2 temperature. Because the source configuration did not permit direct measurement of the gas pressure, measurements of the source geometry were made so the pressure drop into the main chamber could

be calculated from kinetic theory. The pressure in the main chamber was monitored with an ionization gauge.

The ion beam was detected on a Willemite screen, where the intensity could be measured with either an electrometer connected to the screen or with a photomultiplier tube. The photomultiplier was interfaced to the screen with a light pipe which could be fitted with various apertures or lenses. H_2 was admitted into the source through a Pd "leak" via a Granville-Phillips leak valve.

Current-Voltage measurements were made with a Keithley 600A electrometer and a Sensitive Instrument Research Corporation electrostatic voltmeter. Voltages could be read to within 0.25% and were reproducible to that extent. The phosphor screen was biased 22 volts positive with respect to the grounded cathode cap to reduce the effects of secondary electrons. The whole source was shielded so that measurements of currents in the 10^{-12} range could be made.

The optical bench system consisted of a metal casting, epoxy sealed, with numerous electrical, vacuum, and mechanical feedthroughs. The system utilized Viton "O" rings and was pumped with a four inch diffusion pump trapped with LN_2. A background pressure of $\sim 3 \times 10^{-5}$ torr was typical during the experiments. The optical bench allowed the insertion of a variety of electrostatic lenses, beam deflectors, apertures, faraday cups and a photomultiplier light pipe. The electron-optical components were held in "ways" machined to high tolerances so that all components were parallel and on axis.

The source used in the optical bench was similar in design to the one used in the high vacuum system, except that it could not be cooled. Pressure in the source volume was measured with a General Electric thermistor pressure gauge fitted on the cathode cap. The gauge was calibrated with the system thermocouple gauge at 10^{-1} torr and with the system ion gauge at 10^{-3} torr.

Ion currents were measured with a faraday cup biased to prevent the escape of secondary electrons. For scanning work requiring a faster response than the electrometer, the beam was detected with a photomultiplier tube and a high speed scintillator.

The emitters used in these experiments were iridium (Ir) with radii generally 800 - 1500 Å, although emitters with radii down to 350 Å have been used. The emitters were examined and photographed with an electrostatic transmission electron microscope (TEM) loaned to the Oregon Graduate Center by Elektros, Inc. Ir was chosen for the emitters because of its resistance to water etch and its general durability. Work done earlier in this laboratory has confirmed the superiority of Ir emitters to W emitters in any situation where water contamination might be present. A comparison of the properties of an Ir emitter and a W emitter after 0.3 hours operation in an environment with $P_{H_2O} \sim 10^{-4}$ torr is shown in Figures 1 and 2, where it may be seen that while the water had virtually no effect on the Ir, the W emitter performance was degraded by several orders of magnitude. A life test on an Ir emitter at room temperature

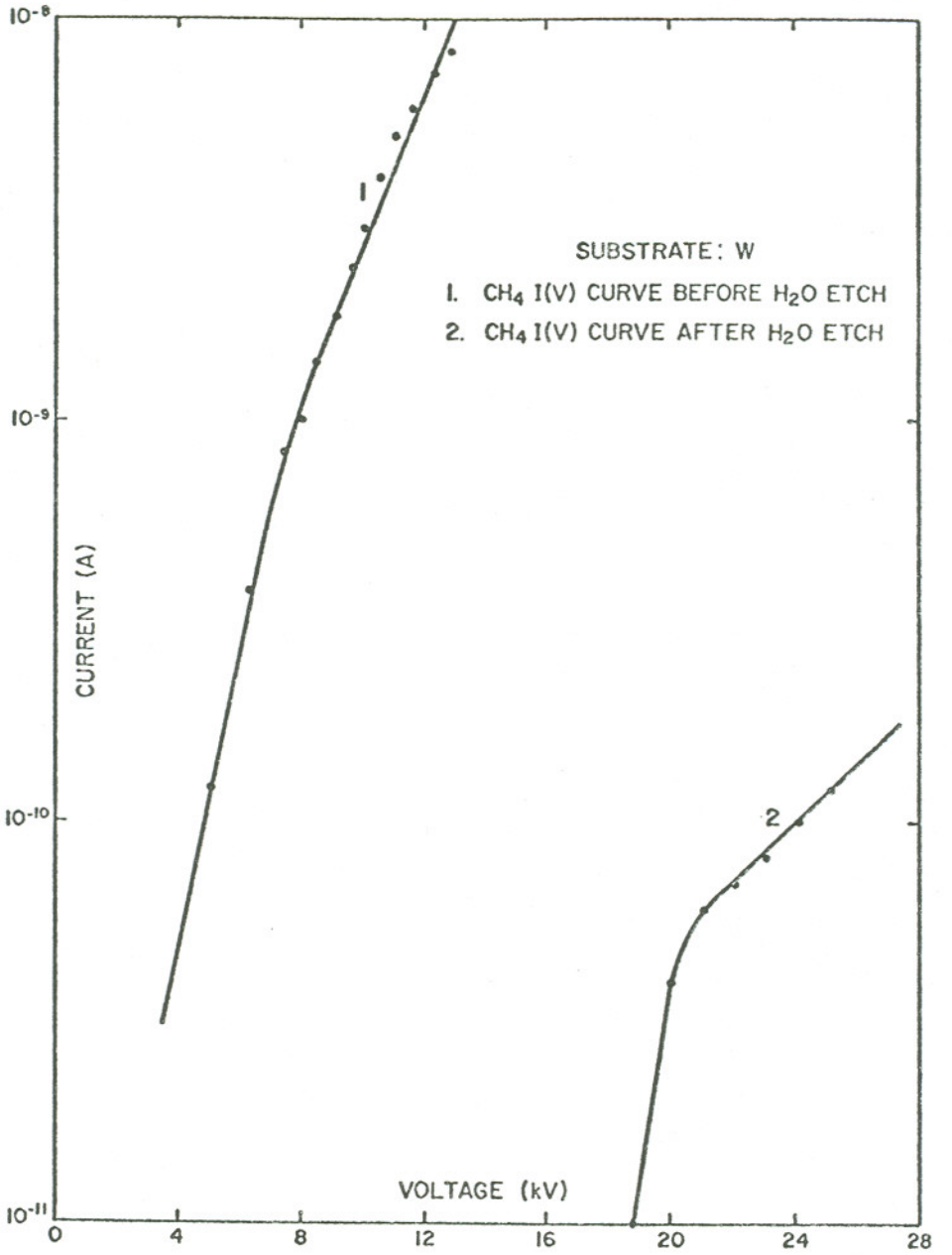

Fig. 1. Performance of W emitter before and after 20 minute exposure to $\approx 10^{-4}$ torr H_2O vapor with field on.

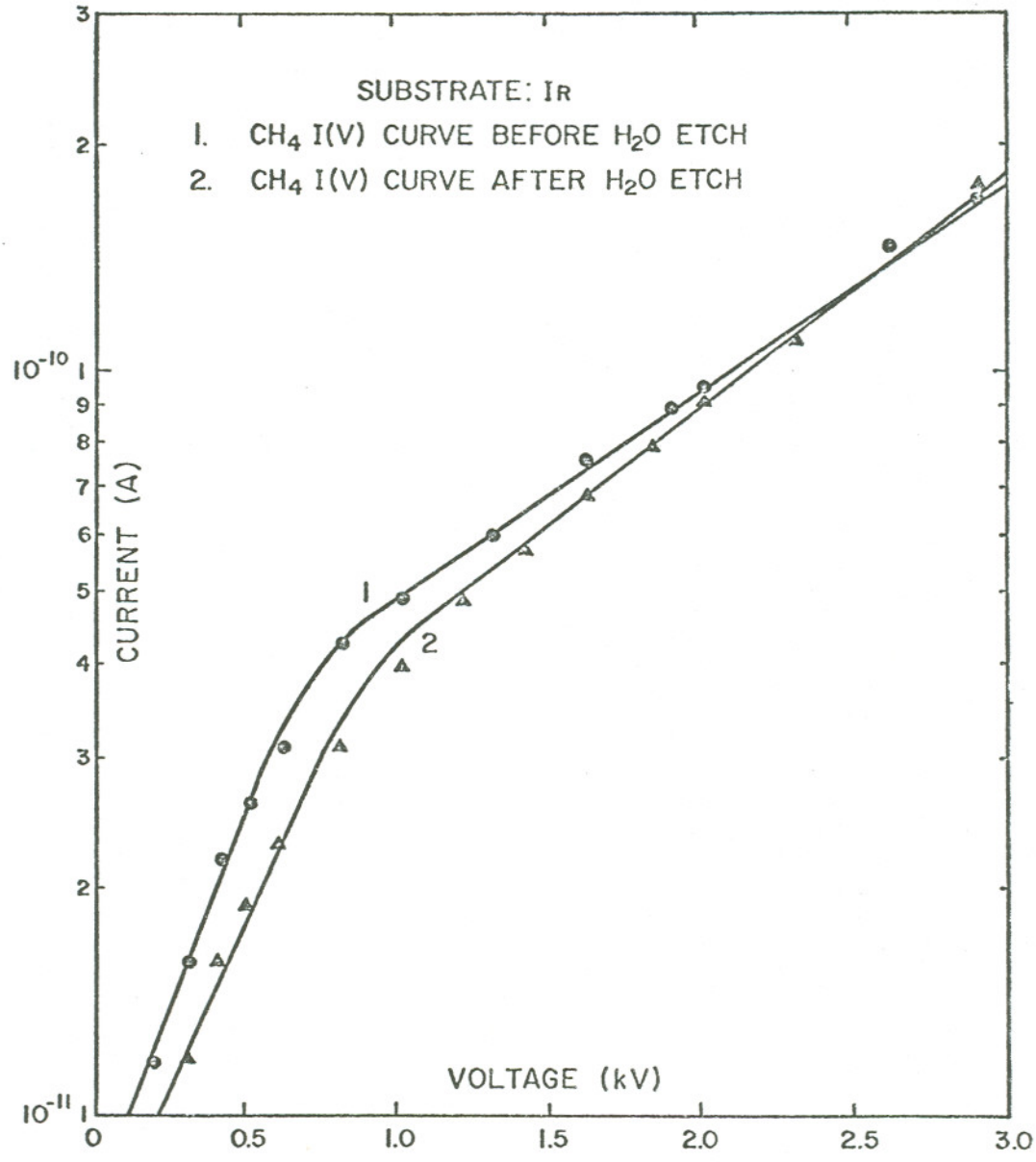

Fig. 2. Performance of Ir emitter before and after 20 minute exposure to $\approx 10^{-4}$ torr H_2O vapor with field on.

with $P_{H_2} = 10^{-3}$ torr showed no change in performance over a period of 12 hours.

B. Emitter Fabrication

The fabrication of Ir emitters is still something of an art. The procedure used by the author is a variation on the method developed by Mr. Noel Martin and begins with the spotwelding of a 0.2" piece of Ir wire 0.002" in diameter to a 0.01" diameter tungsten hairpin, which serves as a heatable base. The Ir is suspended vertically and a small loop of platinum wire is raised around it to about the midway point. A 5% solution of NaOCl (household bleach) is used as an etching solution. A 30 volt A.C. current is then passed between the Ir and the loop. The etching process is quite violent and can be heard across a good sized room. It requires about 7 minutes to reduce the Ir from 0.002" to about 0.001". At this point the voltage is reduced to about 15 volts and the platinum loop is raised and lowered slightly to produce a uniformly thin piece of Ir. When the Ir has been thinned to the point where it is just visible under a 30X microscope the NaOCl solution is lowered from around the loop and a tiny amount of fluid is picked up on the loop for further etching. The voltage is reduced to about 10 volts and the loop brought to the position where the tip of the emitter-to-be is desired. The voltage is applied until the solution on the loop is used up and the process is then repeated until the Ir wire parts, leaving the emitter on the top. The emitter can then be "polished" or sharpened

slightly by etching further with low voltage.

The emitter is examined with a 500X microscope before being used. If its appearance is satisfactory it can be used immediately. If not satisfactory it can be etched further. A photograph of an emitter may be found at the end of this section. The photograph was made with a transmission electron microscope in order to resolve the approximately 1500 Å radius. The emitters in these experiments were not field evaporated.

C. Scanning Ion Microprobe Design

A scanning ion microprobe (SIM) was constructed with a commercial pumping station to provide the necessary vacuum. The optical system consists of two electrostatic lenses, an objective aperture, electrostatic beam steerers and a double deflection beam scanning system with two sets of electrostatic plates for the X and Y directions, respectively. The first lens (objective) is located just below the ion source and the final lens (projector) just above the specimen.

The lenses are arranged as a doublet (see Fig. 3). The objective collimates the beam forming an image at $z \simeq \infty$ of size $d_1 = 2r_1$,

$$r_1 = M\left(\rho^2 + (\tfrac{1}{4}C_{s1}\alpha^3)^2 + (\tfrac{1}{2}C_{c1}\frac{\Delta V}{V}\alpha)^2\right)^{1/2} . \qquad (1)$$

M is the magnification, C_{s1} the spherical aberration coefficient and C_{c1} the chromatic aberration coefficient. ΔV is the energy spread of the beam, V the acceleration voltage, α is the angular divergence of the beam as determined by the objective aperture, which has a diameter of 0.13 mm and ρ is the apparent source size.

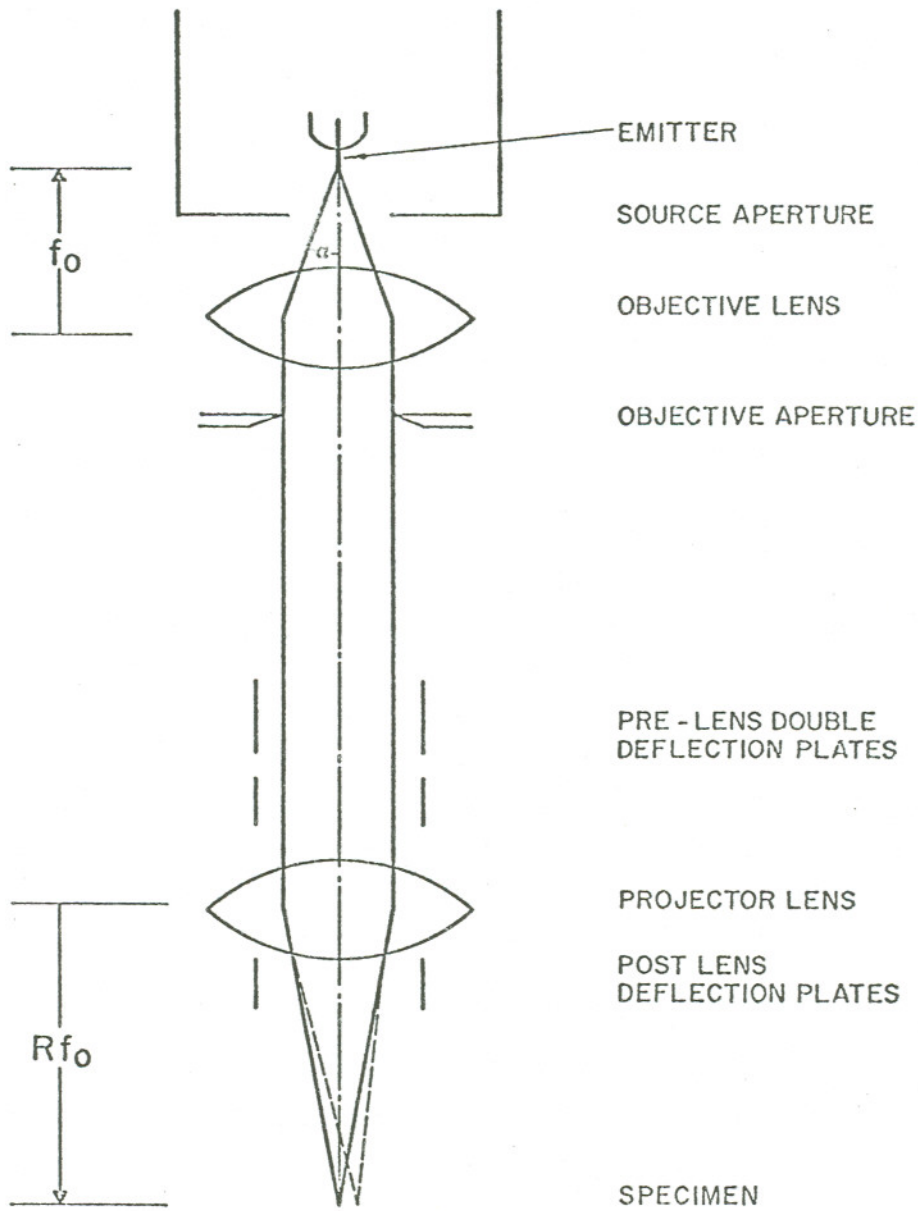

Fig. 3. Schematic diagram of the SIM optical system (beam deflectors not shown). Only one deflection system is used at a time.

The projector lens focusses the collimated beam on the specimen at a working distance of $\approx R f_o$, where f_o is the objective lens focal length $\approx$ 5 mm, R is the ratio of projection and objective lens focal lengths and the amount of demagnification is $M' = \frac{R}{M}$. The overall magnification is $MM' = R$. The diameter of the beam on the specimen is $d_2 = 2r_2$, where

$$r_2^2 = M'^2 \, r_1^2 + \left(\tfrac{1}{4} C_{s2} \left(\frac{\alpha}{R}\right)^3\right)^2 + \left(\tfrac{1}{2} C_{c2} \frac{\Delta V}{V} \frac{\alpha}{R}\right)^2 \qquad (2)$$

Using the values fobj = 5.5 mm $C_{s1} \approx 88$ mm, $C_{s2} \approx 4000$ mm, $C_{c1} \approx 18$ mm, $C_{c2} \approx 150$ mm, $\rho \approx 10$ Å, $\Delta V \approx 4$ eV (for $H_2^+ + H^+$), V = 12 kV, and α = 0.012 and R = 6 then $d_2 = 6300$ Å. The effect of the aberration terms of the project lens are negligible:

$$\left(\frac{\tfrac{1}{4} C_{s2} \left(\frac{\alpha}{6}\right)^3}{M' r_1}\right)^2 = 6 \times 10^{-4}; \left(\frac{\tfrac{1}{2} C_{c2} \frac{\Delta V}{V} \frac{\alpha}{6}}{M' r_1}\right)^2 = 2.5 \times 10^{-2} \qquad (3)$$

so that the overall contribution of the projector lens to the aberration disc of confusion is only 2%.

The objective aperture is a standard 130 μm platinum aperture available commercially for use in electron microscopes. The optical components are mounted in a tube 38 cm long which can be removed from the SIM without affecting the alignment of the components. The lens tube is held rigidly in a vacuum column fitted with a number of feedthroughs for making electrical connections as shown in Fig. 4.

The ion source described above is shown in Fig. 5. It is mounted in an X-Y traversing stage controlled by two 0.00025 cm resolution

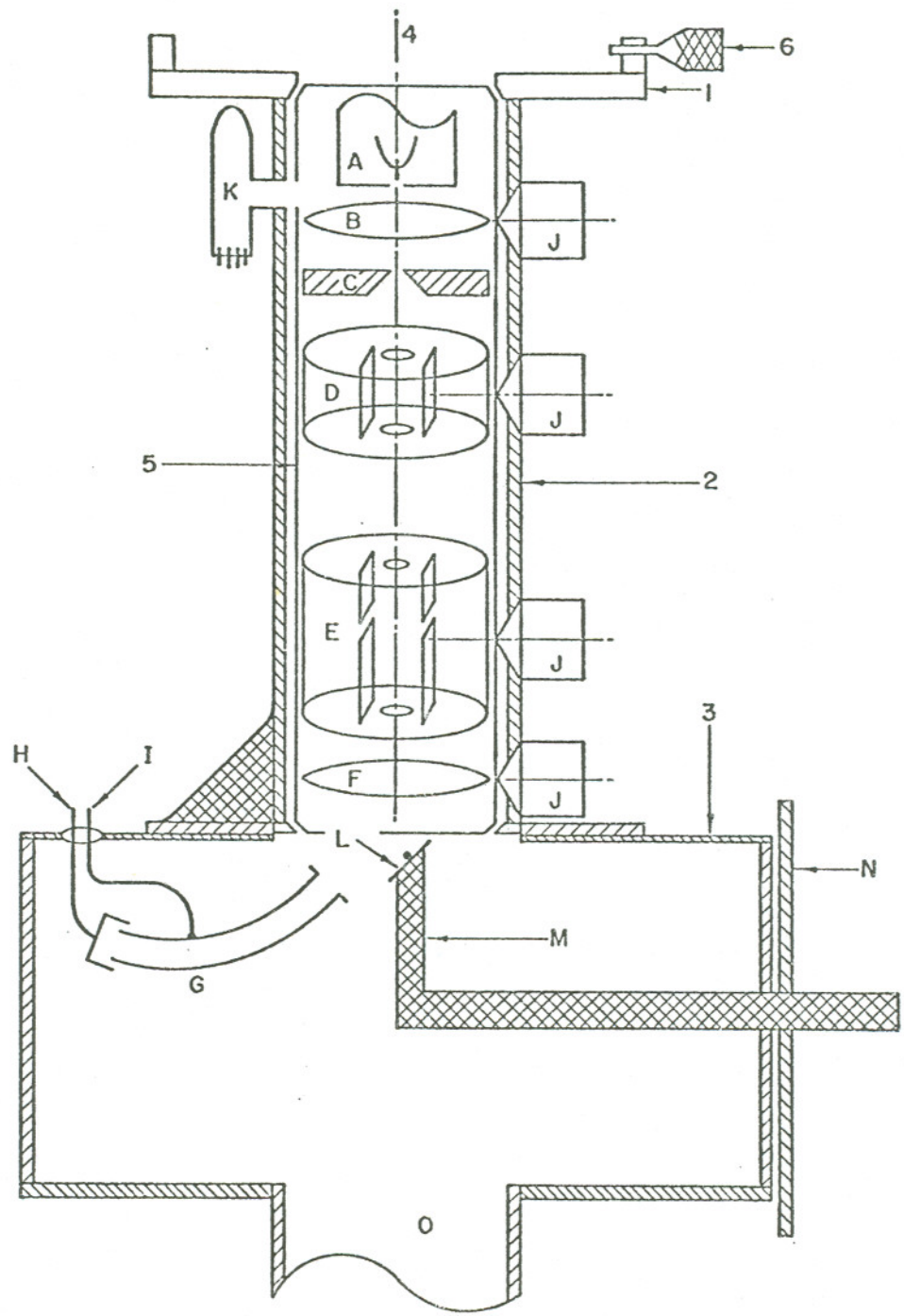

Fig. 4. Schematic diagram of the SIM (see legend following).

LEGEND

1. Ion source traversing stage
2. Vacuum column
3. Specimen chamber
4. Optical axis
5. Lens tube
6. Micrometer

A. FI source
B. Objective lens
C. Objective aperture
D. Beam steering plates
E. Beam deflection plates
F. Projector lens
G. Channeltron secondary electron detector
H. Signal output
I. High voltage input
J. Electrical feedthroughs
K. Ionization Gauge
L. Specimen
M. Specimen holder
N. Vacuum door holding specimen manipulators
O. Vacuum port

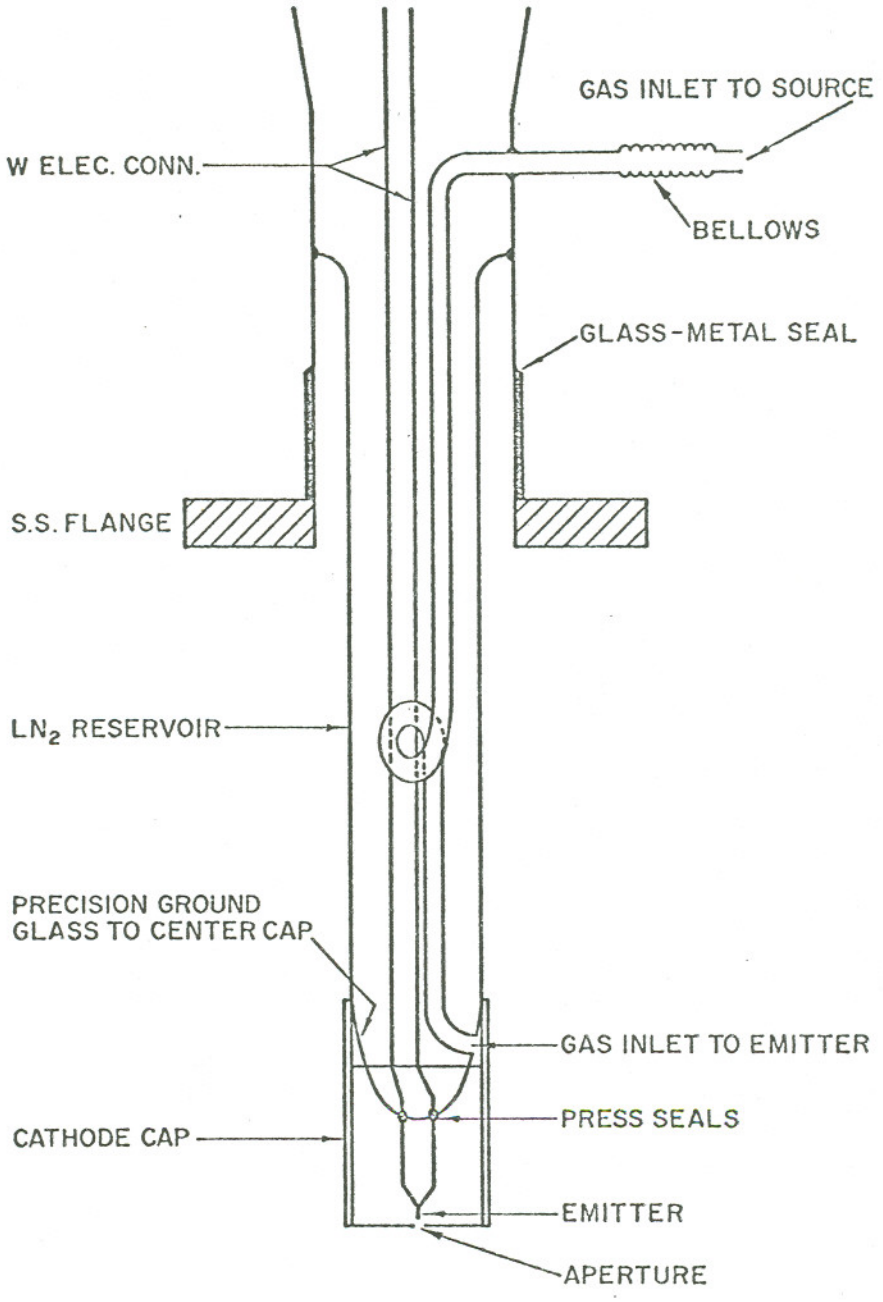

Fig. 5. Drawing of the FI source which was used by technician to build present unit. Aperture size is 0.5 mm, emitter-aperture spacing 0.5 - 1.5 mm.

micrometers. The micrometers are located at the ends of lever arms with the gun halfway between them and the pivot points, so that the motion of the gun is one-half that of the micrometers, i.e., the gun can be moved in 0.00013 cm increments. When the gun is aligned for maximum current on the specimen a movement of the gun by 0.005 cm (50 μm) will alter the image location so that no current strikes the specimen.

The double deflection beam scanner is located 77 mm below the objective aperture and has a 1 mm aperture at the top. The scanner is driven by a set of four high voltage operational amplifiers controlled by a two channel ramp generator. For ordinary viewing the beam is driven at ~ 1 Hz in the x-direction and 100 Hz in the y-direction. The sweep rate can be slowed for photography to ensure that the resolution of the monitor is not exceeded. Just under the beam deflector there is a movable beam stop on which the beam can be intercepted to read the specimen current. The stop is biased +20 volts with respect to ground to suppress secondary electrons.

An ionization gauge is located ≈ 5 cm from the ion gun. The base pressure at that point is $2\text{-}5 \times 10^{-6}$ torr. When gas is allowed into the gun the pressure rises to between 0.9 and 3×10^{-5} torr, depending on how much current is desired and the type of gas being ionized.

The high voltage for the SIM is provided by a regulated power supply which also energizes the electrostatic lenses. In order to

vary the lens focal lengths the voltage applied to them must be variable. This is accomplished by connecting the lenses to the high voltage through a 1000 MΩ voltage divider. In addition, potentiometers can be connected across the high voltage divider for fine focus control. A "floating" nanometer is connected in series with the lead to the FI source so the total current can be measured. All the electrical connections to the SIM are shielded by grounded braid.

Secondary electrons produced when the beam strikes the specimen were originally detected with a secondary electron collector of the Everhart-Thornley type and the signal multiplied with a photomultiplier. Recently (August, 1976) this detector was replaced by a high gain channeltron detector. The signals produced by the multipliers are amplified and the contrast modified slightly by a bias circuit before being fed to the Z axis (intensity control) of the CRT monitor to modulate the intensity.

A simple three-axis stage is used to hold the specimen. The stage is controlled by three micrometers with 10 μm resolution.

The gas inlet system for the gun consists of a Pd hydrogen purifier connected to a manifold where other gas bottles may be attached. Gas is leaked into the gun via a finely controlled Granville-Phillips valve. The manifold has provision for independent pumping to ensure gas purity.

Because of the optical design in which the overall magnification of the source is of the order of unity, pains have been taken to

decouple the microprobe from building vibration.

Vibrational amplitude ~ 3000 Å would be magnified to cause a beam displacement of 1 μm on the specimen. The estimated frequency of vibration of the field emitter mounted on a 0.010" W loop is ~ 20 kHz. Since the vertical scan rate is typically 100 Hz the result of such vibration would be to cause a loss of resolution along the direction of the emitter motion. The gas supply is fixed firmly to the frame of the instrument and the whole SIM is mounted on springs with a ~ 1 Hz resonant frequency. No motion of the emitter is visible under a 500X light microscope with the gun resting on a table. A sharp tap on the glass portion of the gun excites no discernable vibration.

D. Source Sensitivity

Ion current was measured as a function of H_2 pressure in both the optical bench and the high vacuum system to determine the sensitivity in A/sr·torr. Sensitivities were referenced at 3 kV above the Best Image Voltage (BIV)* or 3 kV above the break in the I-V curve as shown in Figures 6 and 7. At room temperature (294 K) sensitivities of 0.5 - 3 × 10^{-6} A/sr·torr were measured in the optical bench

---

*In his studies of FI microscope images Müller found the images of emitter tips to be sharpest ("best") at different voltages depending on the emitter radius and the gas used, hence the term "best image voltage" (BIV) or best image field. For hydrogen the BIV corresponds to about 2.2 V/Å. See Field Ion Microscopy, Principles and Applications, by Müller and Tsong (Elsevier Press, 1969) page 12.

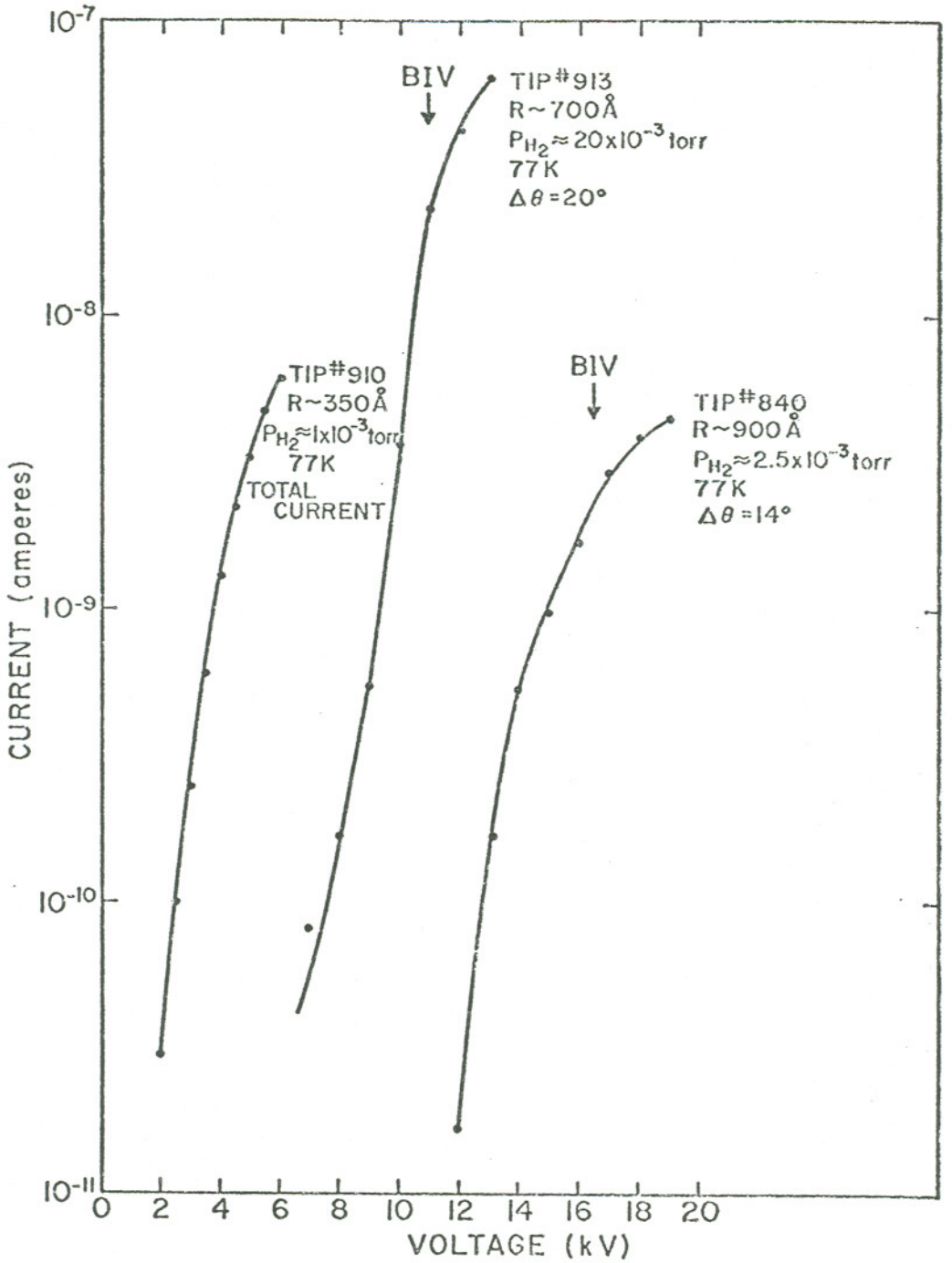

Fig. 6. Current-voltage characteristics for three emitters of varying radii and at various H_2 pressures. Current from emitters 840 and 913 was extracted through apertures of 0.19 and 0.38 sr, respectively.

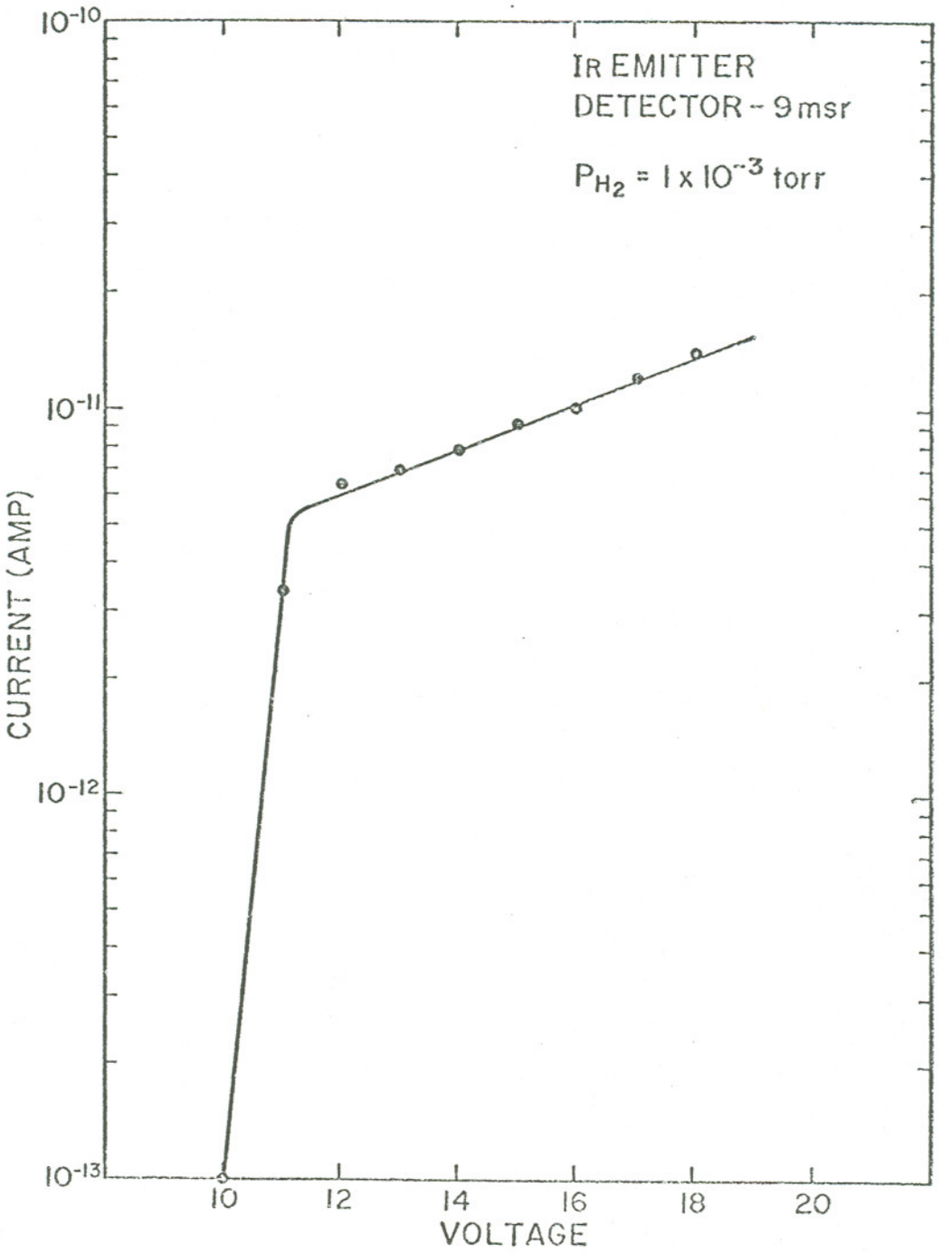

Fig. 7. Current-voltage characteristic of an emitter measured in the optical bench at 300 K.

system. Sensitivities of 0.3×10^{-6} A/sr·torr below 10^{-2} torr, rising to 0.7×10^{-6} A/sr·torr at 3×10^{-2} torr were measured in the high vacuum system. The reason for the increase in sensitivity with pressure in the high vacuum system is not yet known. The greater sensitivity in the optical bench system may be due to low ionization potential contaminating gases entering the source with the H_2. At 77 K the sensitivity in the high vacuum system was measured to be 5×10^{-5} A/sr·torr over the range 3×10^{-4} - 2×10^{-2} torr (see Fig. 8). These results are similar to work recently performed in this laboratory with an array of four Ir emitters where sensitivities of 6×10^{-6} A/sr·torr and 3.7×10^{-5} A/sr·torr were measured at 300 K and 150 K, respectively.

When an emitter was placed 0.7 mm from the 0.5 mm diameter aperture the sensitivity was found to be about 2 times less than when the emitter was 2 mm from the aperture. This result may be due to a lower emitter sensitivity, since no effort was made to ensure emitter uniformity by field desorption before use. On the other hand, the lower sensitivity may reflect a lower gas pressure near the aperture. It is to be expected that at pressures corresponding to molecular flow, the pressure gradient through the aperture would manifest itself at a distance comparable to the aperture dimensions. The maximum H_2 pressure consistent with reasonable emitter life was $\sim 8 \times 10^{-2}$ torr at 300 K. At pressures above $\sim 5 \times 10^{-2}$ torr there are fairly frequent breakdowns through

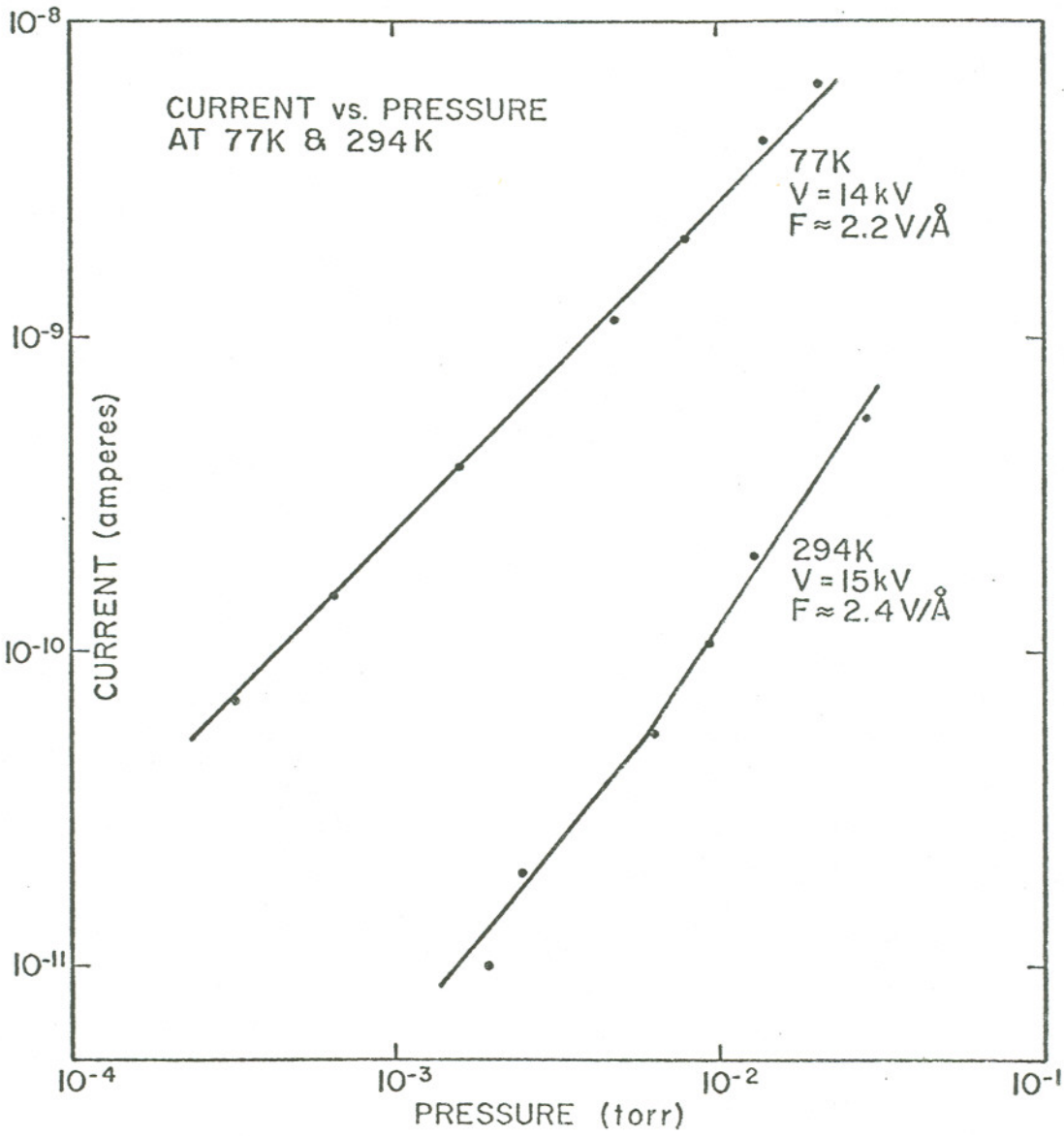

Fig. 8. Current versus H_2 pressure for an emitter at 77 K and one at 300 K demonstrating the improvement in sensitivity due to better accommodation of gas to emitter at low temperature.

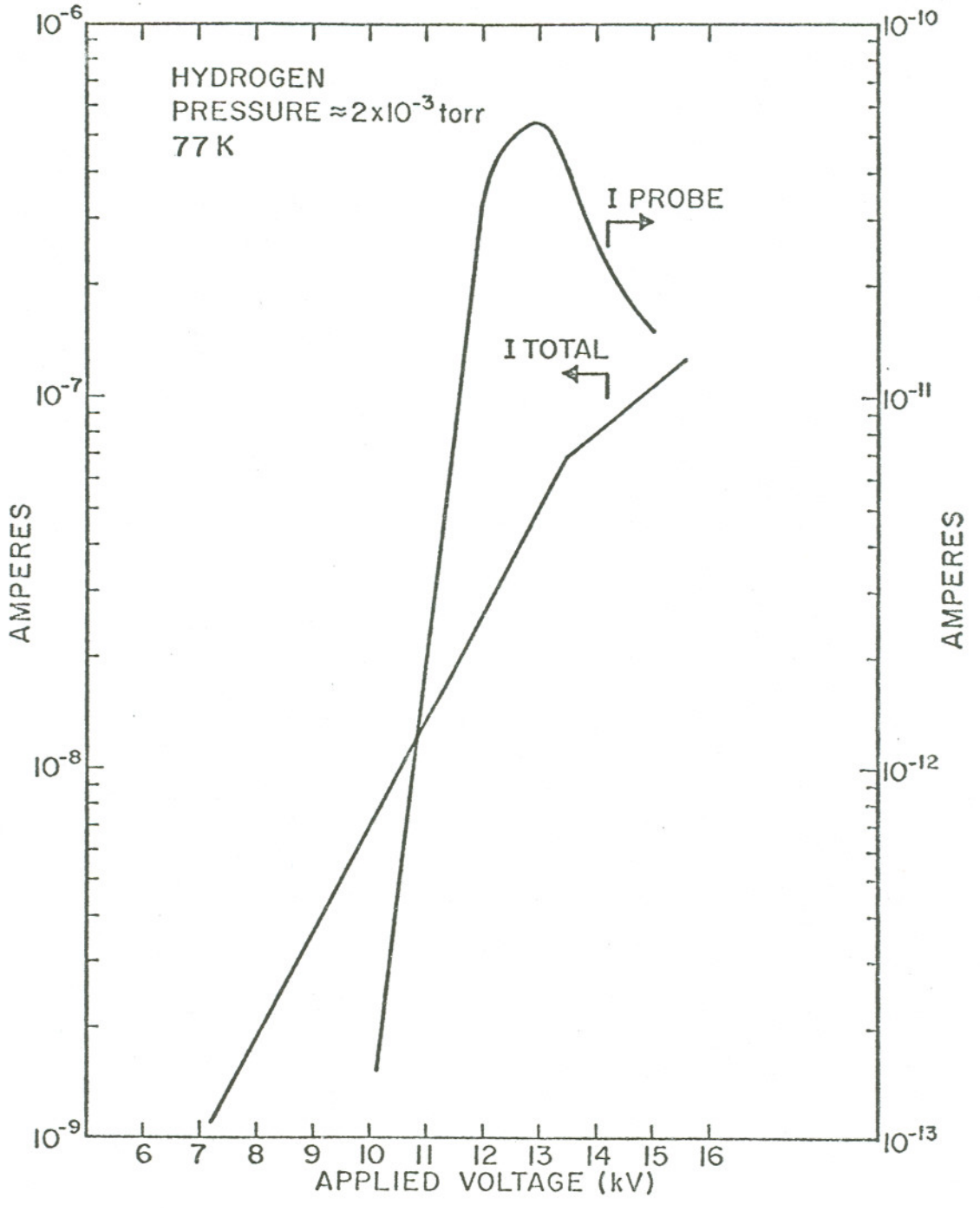

Fig. 9. Probe current and total current as a function of emitter voltage as measured in the SIM near the specimen. Angle subtended by the objective aperture was $\alpha = 0.012$ rad.

the gas, especially with close emitter-aperture spacings.

As mentioned previously, sensitivities were measured at field strengths of 2.3 to 2.6 V/Å -- 10 to 20 percent above the BIV -- in order to achieve maximum source current density within reasonable limits of beam energy spread. At these field strengths the ion current is roughly equally distributed between H^+ and H_2^+.[1] The bulk of the H^+ current falls within an energy spread of 2 eV and the bulk of the H_2^+ current within about 3 eV.[3] The first Jason peak[4] for H_2^+ occurs about 7 - 10 eV below the main peak and is rather small in intensity. No Jason peak is seen for H^+. Diagrams of the total energy distribution for H^+ and H_2^+ may be found on pages 10 and 11 of Section III.

The microprobe has been operated primarily with hydrogen gas at a pressure of $\approx 10^{-2}$ torr and with a field of $\approx$ 2 volts/Å on Ir emitters formed from polycrystalline wire. The applied voltage varies from 10 kV to 20 kV, depending on the emitter radius. A typical current-voltage curve for the gun is shown in Fig. 9, where probe current refers to the current measured just above the specimen.

The objective aperture subtends a solid angle of 0.45 msr when the objective lens is properly focussed to produce a collimated beam with a 5 mm focal length. Under these conditions, with a source sensitivity of 5×10^{-5} A/sr torr the expected probe current is 2×10^{-10} amperes with $P_{H_2} = 1 \times 10^{-2}$ torr.

Because of the optical system employed the current on the specimen is not affected by the focal length of the final lens. As the specimen is moved closer to the lens and its focal length is shortened the overall magnification of the source by the two lenses is lessened and the beam spot size reduced. Thus the current is independent of the resolution for a given objective aperture size.

In addition to hydrogen, Xe and Ar have been used in the microprobe. With Ar total and probe currents similar to hydrogen were observed. Current-voltage characteristics for Ar are shown in Fig. 10 where the pressure was estimated at 2×10^{-3} torr and a probe current of 2×10^{-11} amperes was measured, corresponding to a sensitivity of 6×10^{-5} amperes/sr torr.

Current-voltage curves were taken for Ar and hydrogen with the same emitter and pressures of 7×10^{-3} torr and 15×10^{-3} torr, respectively at 77 K. The results, shown in Fig. 11, are quite interesting. Ar and H_2 have almost identical ionization potentials, 15.7 eV and 15.6 eV, so the barrier penetration probabilities should be almost identical. However, the break in the I-V curve for Ar at 77 K occurs at a much lower voltage than for hydrogen at 77 K or Ar at 300 K. This evidently means that the ionization probability of the Ar atoms is much greater at 77 K than at 300 K. This effect has been seen by Swanson, Bell and Crouser (unpublished) and by Jason et al[4] with H_2 on W at 4.3 K, where films of H_2 form and a much higher current was measured at 1 V/Å than could be accounted for by gas phase

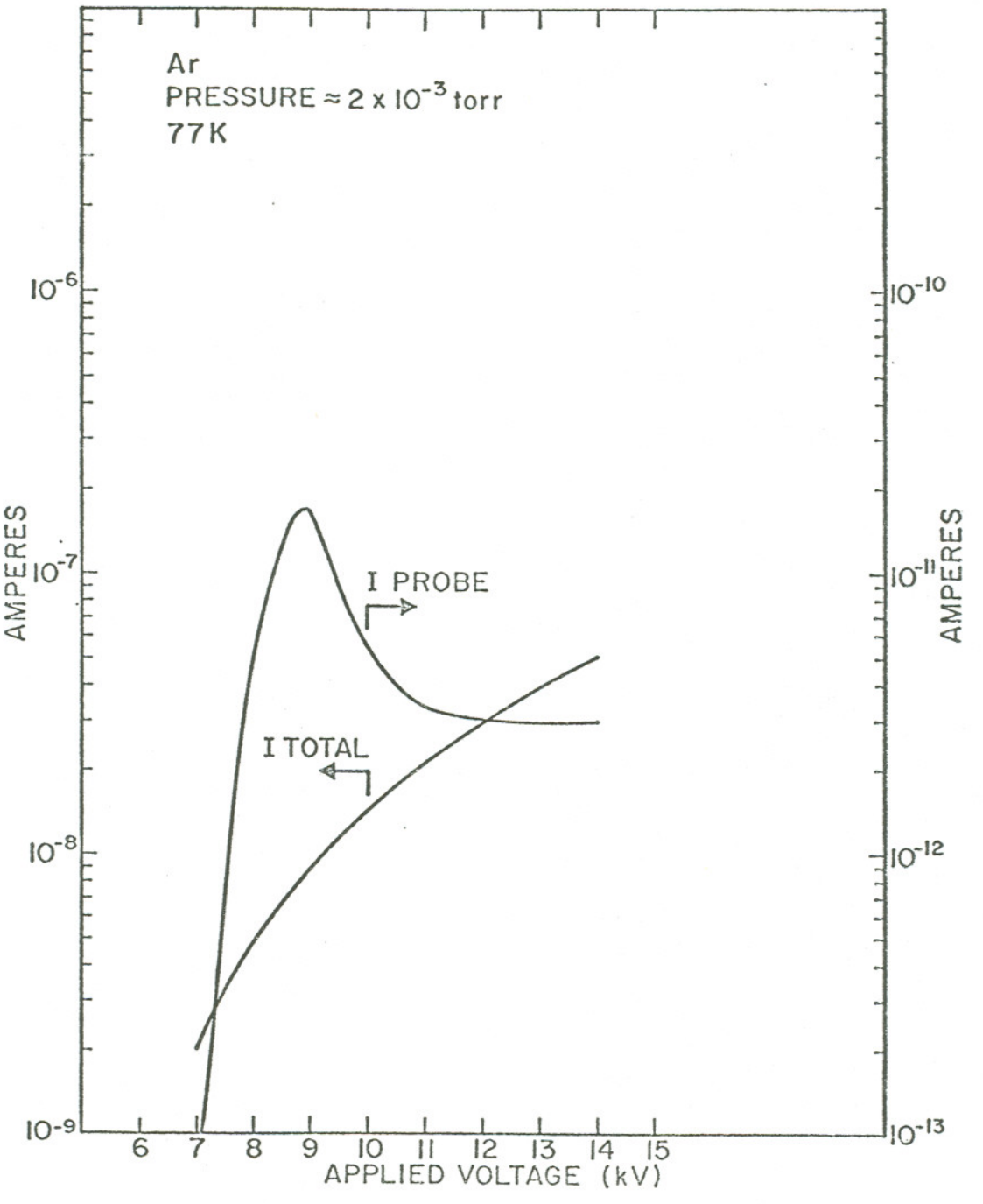

Fig. 10. Probe current and total current as a function of emitter voltage for Ar as measured in the SIM near the specimen, $\alpha = 0.012$ rad.

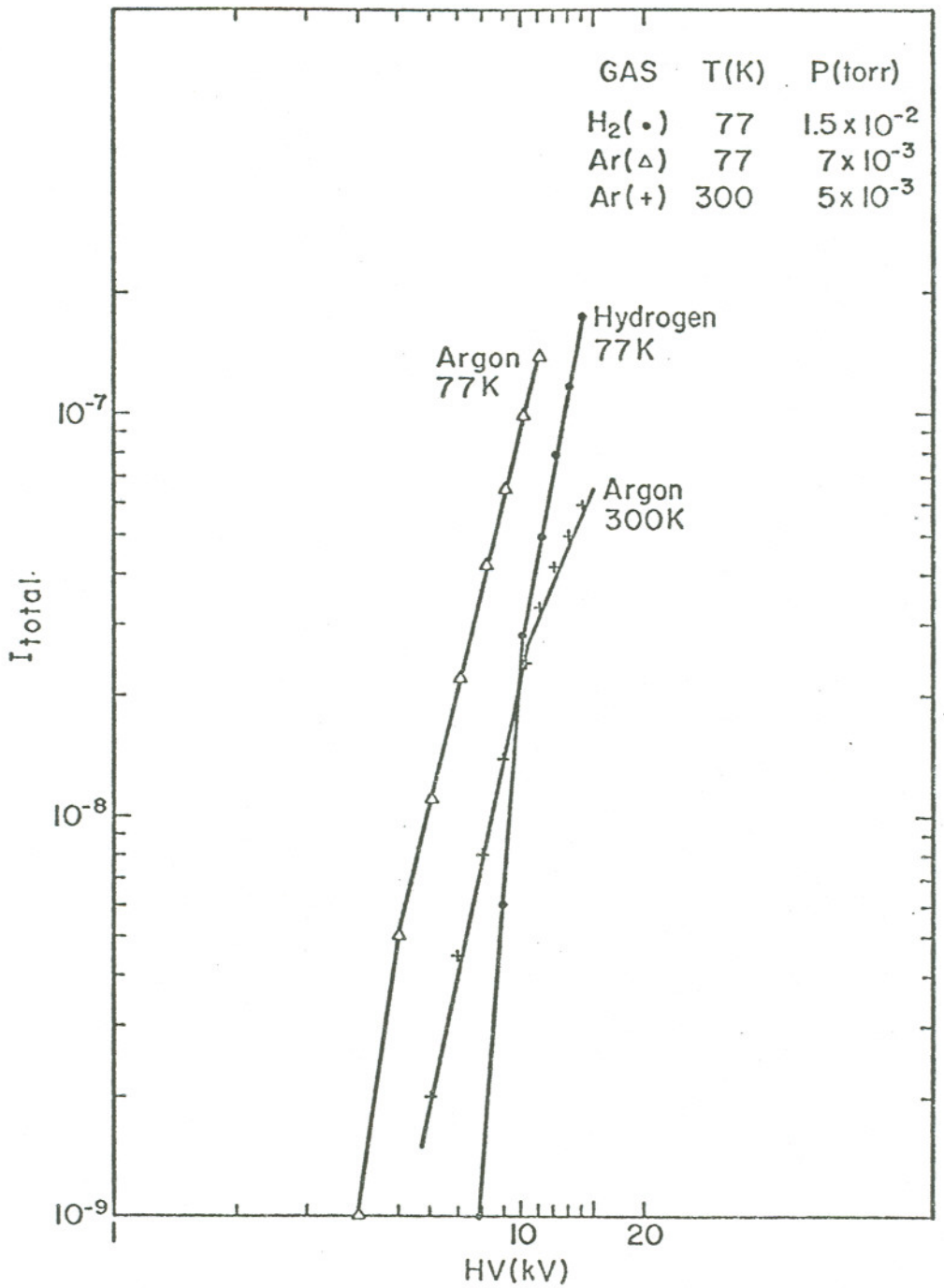

Fig. 11. Total current vs. voltage with the same emitter for H_2 and Ar gases. Note the shift in the I-V curve for Ar at 77 K. Ionization potentials are I_p = 15.7 eV and 15.6 eV for Ar and H_2, respectively.

ionization at the pressure the experiment was performed.

The Ar current was found to be greater than the hydrogen current at any given voltage at 77 K. If the supply S of ionizable material from the gas phase is calculated by means of the hyperboloidal emitter approximation of Van Eekelen[5] for a field at the emitter tip of 2 V/Å (which corresponds to approximately 10 kV in Fig. 11), it is found that $S(Ar) = \text{const.} \times 3\ P_o$ and $S(H_2) = \text{const.} \times 7\ P_o$, where P_o is the gas pressure with the field off. In this case P_o is 7×10^{-3} torr for Ar and 15×10^{-3} torr for H_2 so the expected ratio of hydrogen current to Ar current is 5. In actuality we see there was 5 times more Ar current than hydrogen current.

These two results mean that the supply of Ar is not coming solely from the gas phase. The higher ionization probability indicates that a film of Ar forms on the emitter and that the ionization takes place from this film. The dwell time t of the Ar atoms in the ionization region would be longer in a film and since the ionization probability is proportional to t (see Section III B) the barrier penetration factor D, which depends strongly on the field, could be less and the ionization probability remain the same. The indicated field at the break in the Ar I-V curve is about 1.1 V/Å which implies a dwell time $\sim 10^8$ times longer than in the gas phase.

That such a film formation is possible can be inferred from the properties of Ar. The triple point of Ar is at 84 K and 518

torr. The Ar pressure at the emitter when the field is 1.1 V/Å if the pressure when the field is off is 7×10^{-3} torr will be about 300 torr. This rises to about 2×10^{4} torr if the field is 1.3 V/Å. Thus one could expect both liquid and solid films, depending on the local field strength at the tip.

Additional evidence for film formation comes from an experiment by Swanson (unpublished) and dynamical calculations by Van Eekelen.[5] Swanson measured the I-V characteristics for hydrogen with an array of Ir emitters at 300 K and 150 K and found a shift towards lower fields for a given total current as the temperature was lowered, but the curves cross at higher fields. It is certain that hydrogen does not form films at these temperatures. The same effect is predicted by Van Eekelen for He field ionized from the gas phase, i.e. a shift towards lower fields for given current and a convergence of the characteristic curves at high fields. In the case of Ar, the curves diverge at higher fields, indicating the supply mechanism is not pure gas phase. Different results were found with Xe. The total currents were similar to hydrogen again but now the probe current was very low, as shown in Fig. 12. The ratio of Xe to hydrogen current at 77 K and 3.5×10^{-3} torr with a field of 2 V/Å is unity, based on gas phase supply considerations. This is what was measured. Since the triple point of Xe is at 161 K and 616 torr, and the pressure at the emitter tip at 2 V/Å is 10^{6} torr, a solid layer will form. Evidently the Xe does not diffuse up the emitter shank

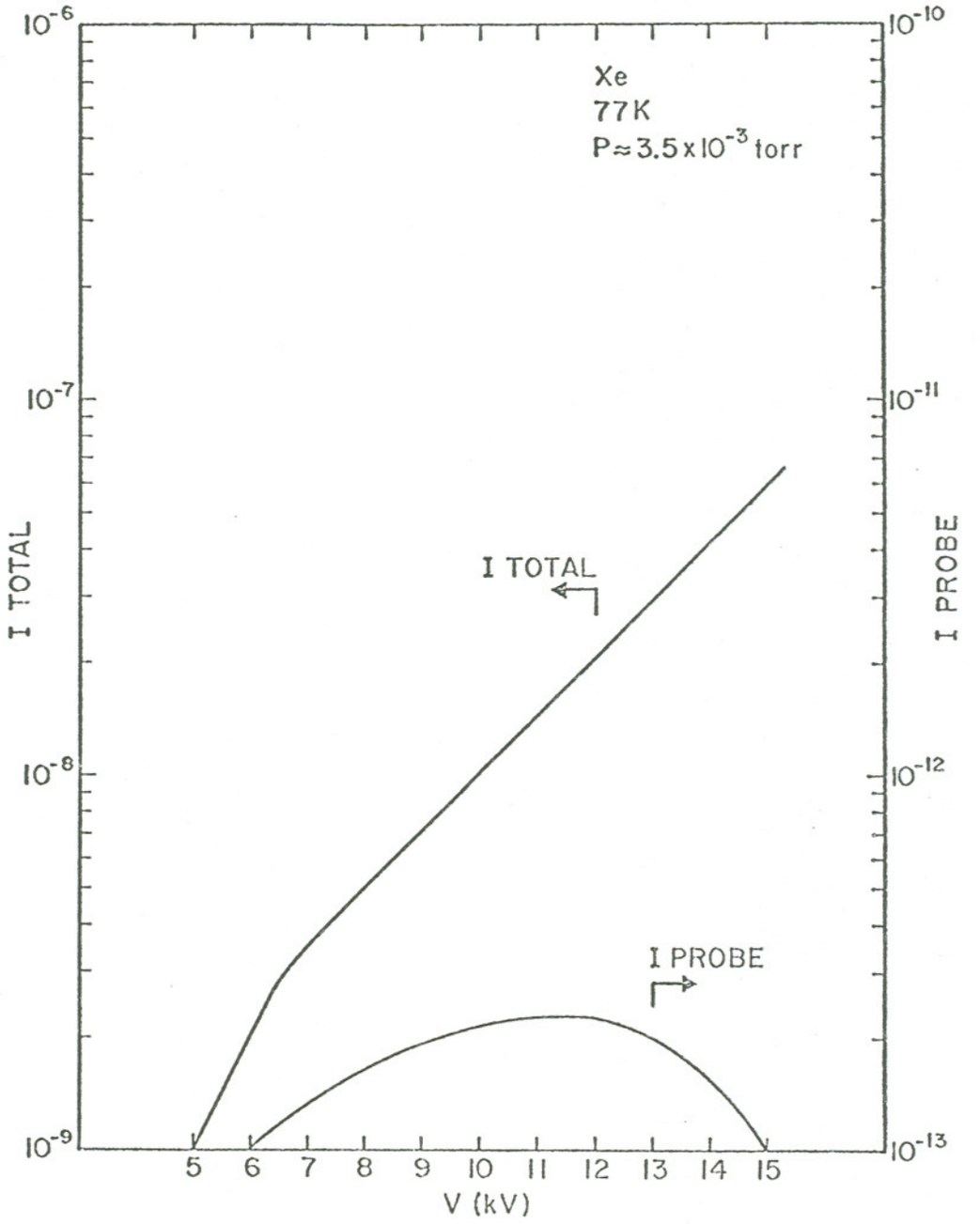

Fig. 12. Total current and probe current as a function of emitter voltage for Xe at 77 K.

to the ionization zone, since the current is what one would expect from pure gas phase supply.

During the initial experiments the effect of residual water vapor in the vacuum system ($P \sim 10^{-5}$ torr) was seen when large currents $\sim 10^{-7}$ amperes were seen while no gas was admitted and I-V curves were measured which showed "hysteresis," i.e., depended on whether the voltage was being raised or lowered. This is evidence of complex water films forming on the emitter.[6]

E. Noise Measurements

The signal to noise ratio of the source was measured with a spectrum analyzer attached to the output of an EMI 9502B photomultiplier which faced against the phosphor screen of a glass tube. The ion source at 300 K was attached to the tube and pumped on a high vacuum system. The photomultiplier subtended a solid angle of $\simeq$ 9 msr. The photomultiplier current was monitored with a high quality microammeter and the background current I_{BG} and $\langle \Delta I_{BG}^2 \rangle^{1/2}$ were constant. The results are shown in Table I. Since it is evident that there is relatively little noise in the signal above f = 10 Hz, the frequency of the spectrum analyzer was swept from f = 1 Hz to f = 100 Hz with a bandwidth of Δf = 10 Hz with the beam on and then with the beam off. It was found that the spectral densities were practically identical above f = 15 Hz. It was noticed upon visual examination of the viewing screen that various emission sites on the emitter surface turned on and off in a random fashion,

and it appeared that the main contribution to the low frequency noise is the current from these sites. Since the noise remained constant as the current was increased (by increasing the gas supply pressure) it appears that the sites responsible for the noise emit independently of the gas pressure. Thus, as the current is increased the signal to noise ratio improves. Measurements made on the current on target in the SIM with the FI source at 77 K show the same behavior. In the first case the current was increased twofold by increasing the source gas pressure and S/N improved twofold as well. In the latter case the current was increased approximately threefold by increasing the voltage applied to the emitter and S/N improved by the same ratio.

In the SIM the objective aperture subtended 0.15 msr, the maximum detected current on the specimen was 7×10^{-11} amperes and S/N = 43 in the interval 1 - 11 Hz, as measured with a spectrum analyzer. The noise spectrum was also analyzed by recording it on a wideband tape recorder and analyzing it with a computer program which performs a Fourier decomposition of the signal with $\Delta f = 2$ Hz. The result of this analysis is shown in Fig. 13. On the same scale the shot noise current for $\Delta f = 10$ Hz would be at approximately 0.06, with $\langle I^2_{SHOT} \rangle = 2eI\Delta f$.

It was found that the angular distribution of hydrogen extended out to $\approx 18°$ (see below). When the emitter was placed so the source aperture subtended $\approx 27°$ S/N was ~ twice what was measured when the

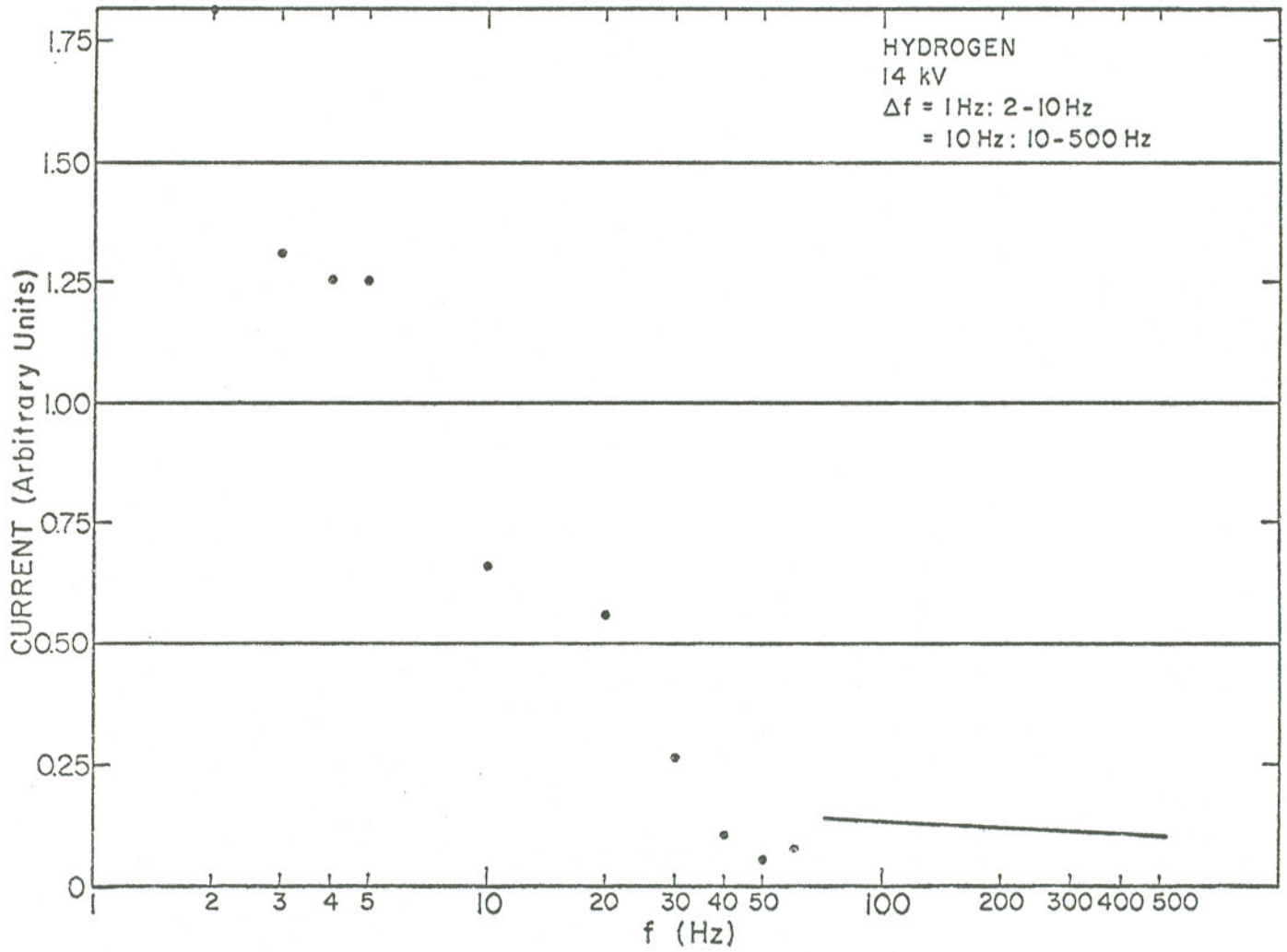

Fig. 13. Spectral density of the probe current for H_2 gas at 77 K, F ≈ 2 V/Å. The shot noise limit is $\langle I^2_{Shot} \rangle^{1/2} \approx 0.06$.

emitter was moved away from the aperture to the point where the aperture subtended $\approx 14°$. The most likely explanation for this effect is that ions striking the aperture with energy E_o cause adsorbed gas molecules to be liberated. The molecules which are negatively ionized in this process will be accelerated back to the emitter where they will cause sputtering damage. This can be expected to affect current generation at the emitter tip.

As mentioned above, the field emitters used here have not been field evaporated, but they are flashed briefly before use. The exact state of the emitter surface is not known so that it is difficult to specify mechanisms for noise generation. It is known that surface adsorbates affect ionization rates, and so changes in amounts and location of adsorbates could be important. At the fields used to ionize hydrogen, $\sim 2 \times 10^{10}$ volts/meter, there are numerous gases which can reach the emitter or emitter shank without being ionized.

F. Angular Distributions

Angular distributions were measured in the optical bench by using a four plate deflection system, calibrated by deflecting an electron beam of known energy across two 100 micron apertures separated by 0.391 cm. The faraday cup was fitted with a slit aperture 1.2 × 12.5 mm located 40 mm from the emitter. The aperture subtended a solid angle of 9.4 msr and had a resolution of 30 mr in the direction of deflection.

Angular distributions shown in Fig. 14 were measured with two emitters at 294 K in the optical bench system, with H_2 gas at

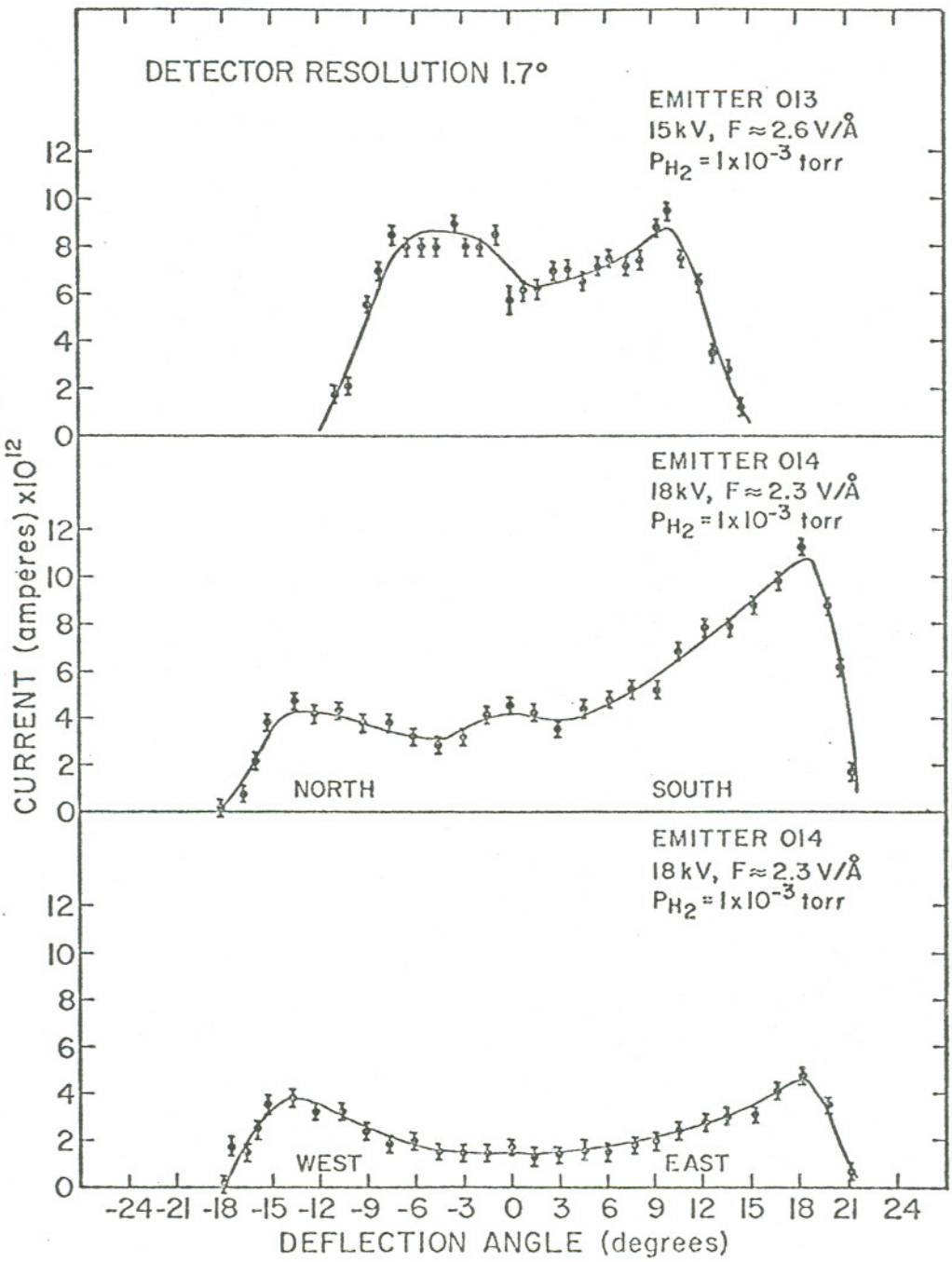

Fig. 14. Angular distributions measured in the optical bench at 300 K for emitters 013 and 014. Note symmetry for orthogonal directions of emitter 014. Detector resolution was 30 mrad (1.7°).

1×10^{-3} torr at 18 kV and 15 kV ($F \cong 2.6$ V/Å and $F \cong 2.3$ V/Å). The background pressure was 3×10^{-5} torr. The asymmetry of the angular distributions taken at right angles indicates a probable emitter orientation along the [111] direction.

In Fig. 15 is shown an angular distribution taken in the high vacuum system with a field of 2.3 V/Å at a H_2 pressure of 1.5×10^{-3} and an emitter temperature of 77 K. This was measured by slowly sweeping the photomultiplier, light pipe and collimating aperture across the faceplate of the FI tube. The angular resolution is $\approx 3°$. The horizontal line represents the photomultiplier background current.

A difficulty that was found when using the emitters in the SIM is that the fabrication procedure results in some emitters having poorer emission along the axis than others, although the total emission remains fairly constant. This is due primarily to local structure variations on the end of the emitter. An example of this is shown in Fig. 16 reproduced from an unpublished report by Swanson, Bell and Crouser. It can be seen that emission comes from different crystal planes of the emitter in very different amounts and changes with field in ways which depend on the plane. When an emitter is used in the SIM it is flashed to a high temperature briefly to try to smooth the surface, but the fabrication process gives different results each time. The problem is serious because the emission on the axis can change by as much as a factor of ten.

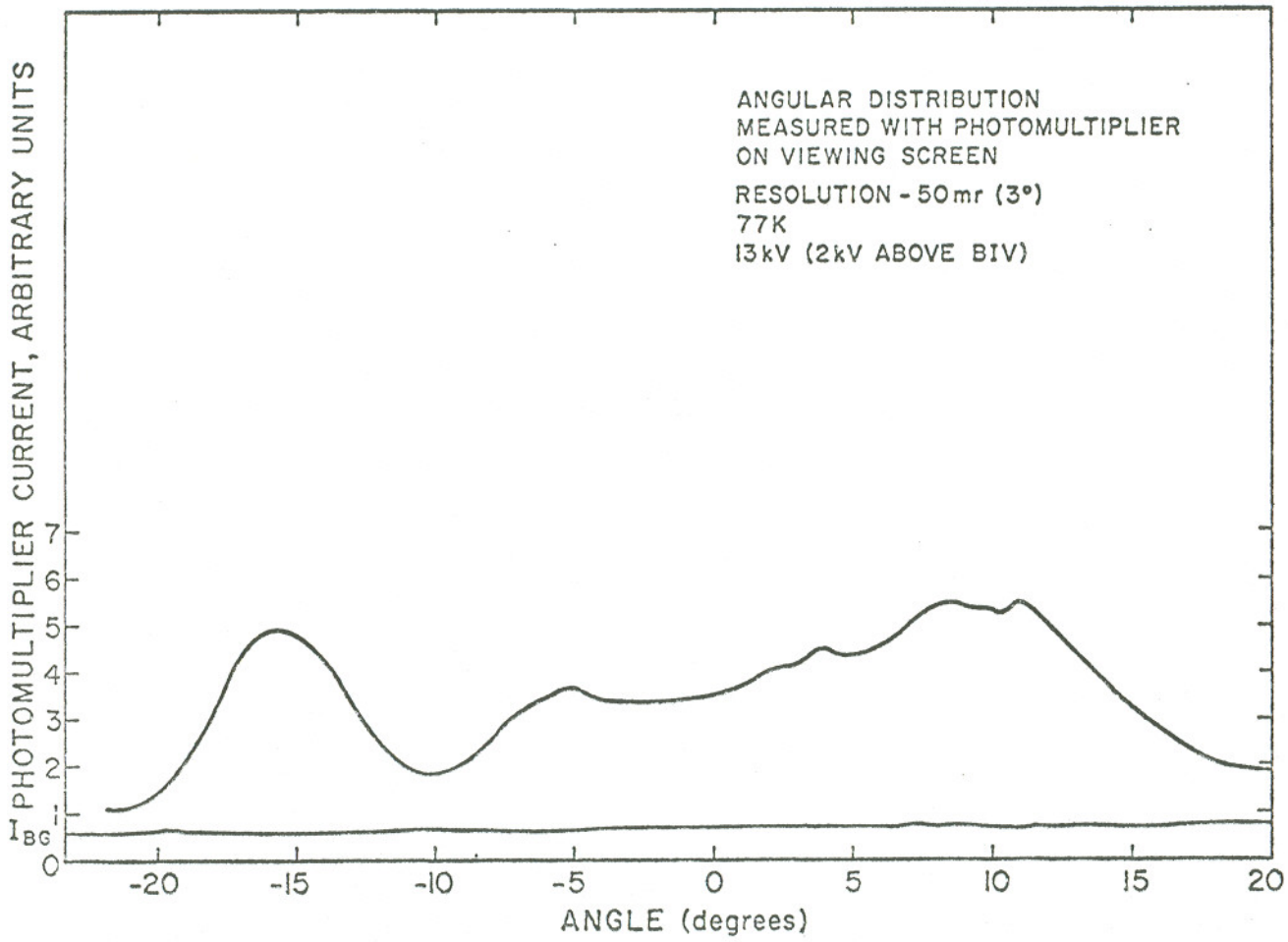

Fig. 15. Angular distribution measured in a high vacuum system with a photomultiplier apertured to accept 3°, as seen from the emitter. I_{BG} is the photomultiplier reading with the emitter voltage off.

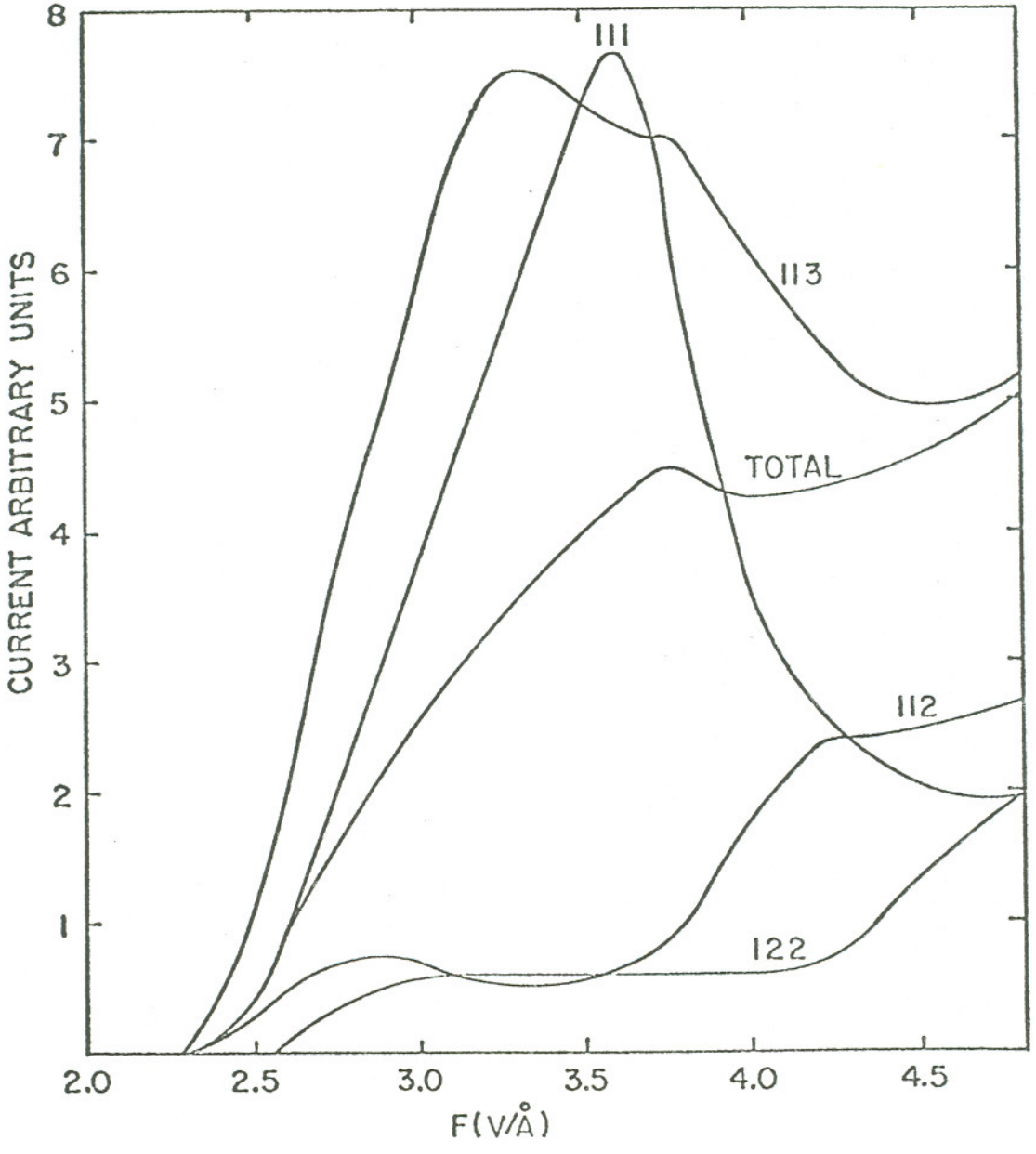

Fig. 16. Current-voltage characteristics of different crystalline facets of a W emitter showing the effects of local field variation (reproduced from unpublished work of Swanson, Bell and Crouser).

A primary goal of the continuing research on the FI microprobe will be to study ways of fabricating emitters so the emission on axis is uniform.

G. Resolution

The resolution of the SIM was estimated from the following considerations. Suppose two similar objects are close together and the beam is scanned over them. When the beam is moved so it just falls on one object the number of secondary electrons generated is $N = N_o$. When it is moved so it just falls on the other object the number of secondaries is again N_o. When the beam is moved between the objects the number of secondaries falls to $N = 0$ until the objects are a distance $d \approx \delta$ apart, where δ = beam diameter. As d grows smaller, $N \to N_o$. The objects can be considered resolved until $N = \frac{N_o}{2}$.

The signal generated by the secondary electrons in the microscope is proportional to N, and depends on two factors for a simple specimen which consists of a uniform material. One is how much of the beam is striking the object, the other is the angle the beam makes with the normal to the specimen's surface. If the object is small these effects must be multiplied together and integrated over the beam profile.

The beam is assumed to be circular and to have a Gaussian profile:

$\frac{dI(r)}{dr} = \frac{\exp\left(-\frac{r^2}{2\sigma^2}\right) I_o}{(2\pi\sigma^2)^{1/2}}$, where I_o is the total current. The beam radius

was taken to a = 2σ, since 95% of the current will be within r = a. The number of secondary electrons generated as the beam passes over a specimen was calculated for three configurations: uniform circular wires of radius R = 10a and R = 2a, and a straight edge.

The variation of the number of secondaries produced varies as $\frac{1}{\cos\theta}$, where θ is the angle the beam makes with the specimen normal, up to some maximum angle θ_m determined by the range ρ of the beam in the target and the range X_o of the secondary electrons in the target. For 12 keV H_2^+ ρ is[7] ≈ 200 Å in Au and will be the same in W. X_o ≈ 30 Å so $\theta_m = \cos^{-1}\left(\frac{X_o}{\rho}\right) = 81.4°$. When $\theta > \theta_m$ the number of secondaries is approximately constant.

The result of the calculations is shown in Fig. 17 where the distance is measured in units of beam radius a. The leading edges of the three curves in Fig. 17 which fall between x/a = +1 and x/a = -1 can be fit by the equation $f = \text{const.} \times \left(\exp\left(\frac{x + a}{a}\right) + 1\right)^{-1}$. As can be seen in Fig. 18 the separation of the objects in order that $N = \frac{N_o}{2}$ must be $\simeq \frac{a}{2}$, and this distance corresponds to the distance over which the signal rises from approximately 25% to 75% of its maximum. These points also correspond to the full width of the derivative of the curve f at 64% of its maximum.

The resolution of the beam was measured by photographing a tungsten D.C. dropoff field emitter and measuring the negative with a microdensitometer. The data points fit a curve described by the function f perfectly (see Fig. 19). As a check, a measurement

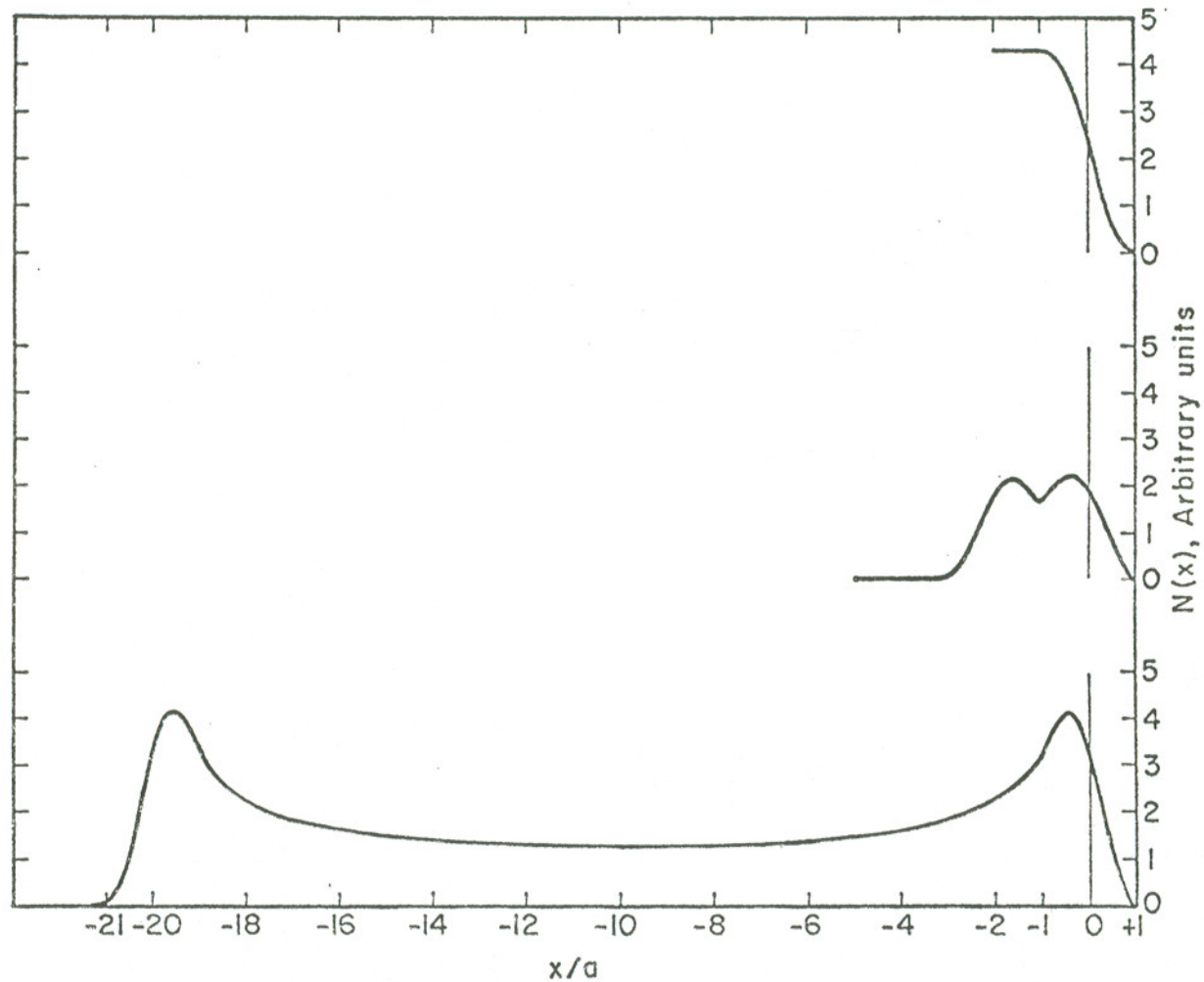

Fig. 17. Calculated secondary electron yield for an ion beam of radius a passing over three objects. From bottom to top: a circular rod of diameter 10a; a circular rod of diameter 2a; a straight edge. In each case the beam begins to strike the objects when the center of the beam is at x/a = +1.

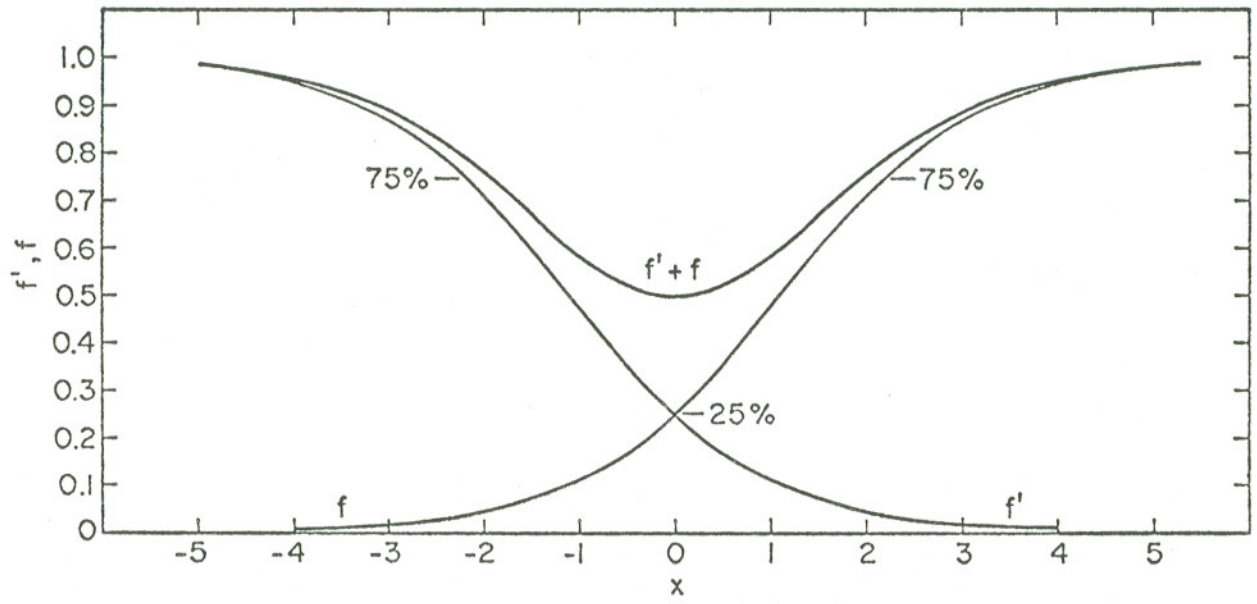

Fig. 18. Calculated secondary electron yields for two objects separated by x = a/2 (a = beam radius) so that the yield falls to 0.5 when the beam is midway between them.

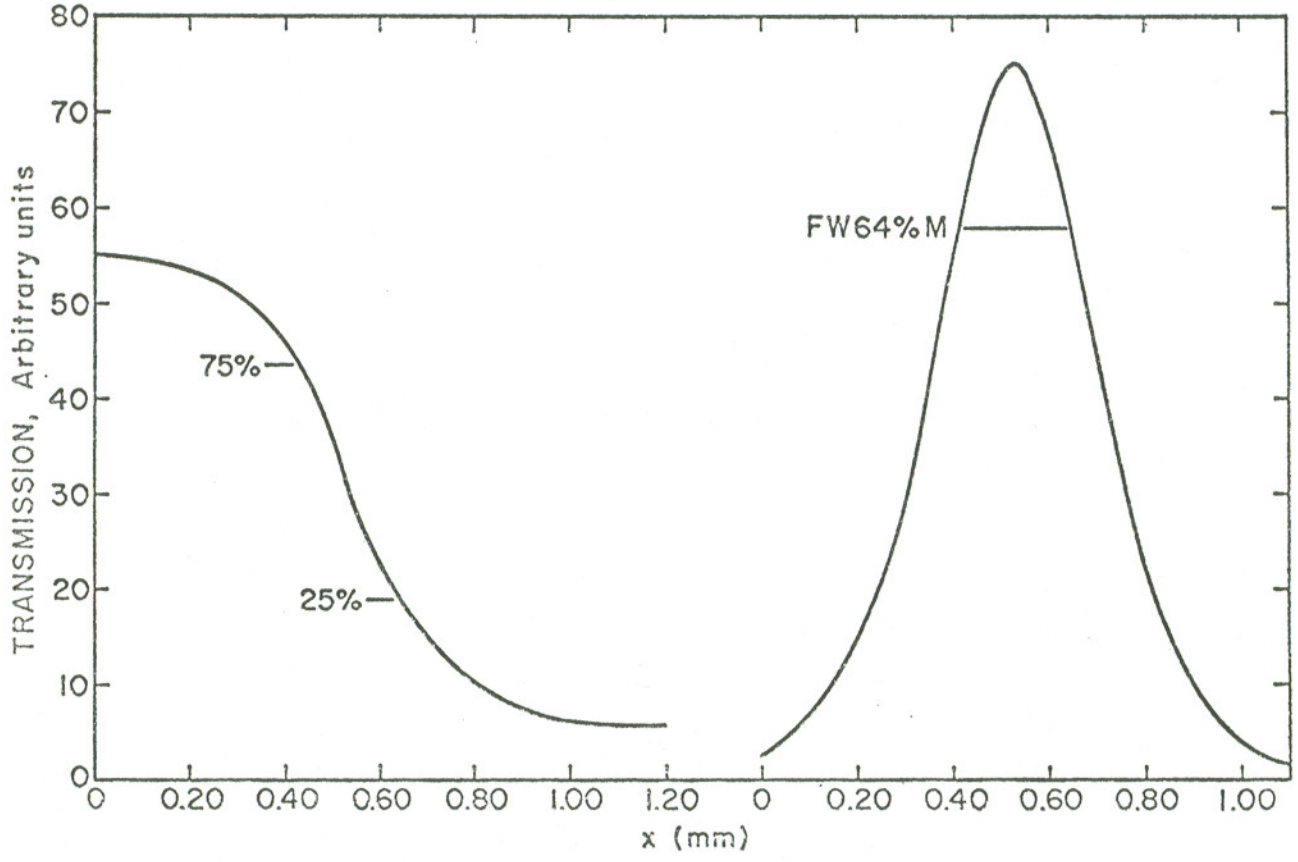

Fig. 19. Transmission through a negative produced in the SIM for a resolution test. Right hand figure is the derivative of the transmission curve. Specimen was a W emitter.

was made by scanning over the emitter in one dimension and recording the output of the photomultiplier on a storage oscilloscope. The emitter was moved 50 μm between scans as shown in Fig. 20. The resolution was taken to be the rise distance of the trace from 25% to 75% of maximum. In both cases the measurements gave $\delta = 2a = 6700$ Å.

H. Contrast Mechanisms

The contrast in the image of a scanning microscope operating in the secondary electron mode naturally depends on the mechanisms which govern the emission of secondary electrons. It is worthwhile to look at the mechanisms for ions and electrons to see if there are any drastic differences. Because studies of secondary electron yields from electron and ion bombardment have mostly been done with metallic and polycrystalline materials we will compare results for these materials.

The secondary electron emission coefficient δ, i.e., ratio of secondary electrons emitted to primaries incident for an electron beam incident on a surface depends[8,9,10,11] on the work function of the material, the surface roughness, angle of incidence of the primary beam, and energy of the primary beam. Secondary emission is caused by a transfer of momentum from the incident beam to the electrons and the lattice (in a metal) or atoms of the target. Interaction with the lattice is essential if electrons are to be emitted in accordance with the conservation of momentum.[12]

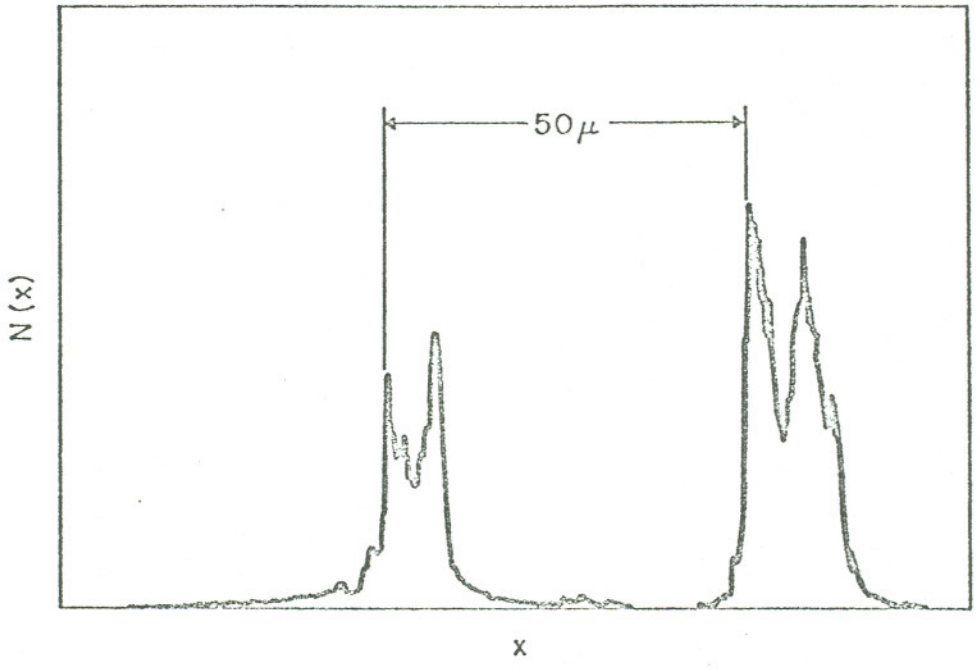

Fig. 20. Secondary electron yield produced by scanning the beam in one dimension across a W emitter. Recording was made on a storage oscilloscope driven in the x-direction by the SIM deflection voltage.

For a given angle of incidence the secondary yield rises with energy until a maximum is reached and then declines.[11,13] The decline is due to the inability of the secondaries to reach the surface when produced deep in the specimen by the high energy primaries, and the decreasing cross section for the production of secondaries as the primary energy increases. The value of δ_{max} is much higher for halides, oxides, phosphors, etc. than for pure metals.* For metals, δ ranges from 0.5 for Be and Li to 1.4 for W and 1.7 for Tl. δ_{max} varies from 1 to 10 for various halides, phosphors and oxides and can be as much as 15 - 20 for crystals such as KBr, CsBr, etc. δ has its maximum value for primary energies of between 250 eV and 800 eV for most metals, but for many halides and oxides the maximum value occurs between 1 and 2 keV.*

The energy distribution of the secondary electrons, not counting recoiling primaries, is peaked at a low energy, < 20 eV independent of the bombarding energy E_B if 20 eV < E_B < ~ 20 keV.[11]

Above ~ 20 kV there are significantly more secondary electrons with higher energies,[14] apparently due to primaries which have suffered several collisions and then been re-emitted. $\frac{\delta_{true}}{\delta_{re\text{-}em}}$ is roughly proportional to (target density)$^{-1}$.

Since the beam energy of a scanning electron microscope is

---

*American Institute of Physics Handbook, 1972 ed., pages 9-184 and 9-185.

usually variable the change in δ with energy can be a useful property to exploit. Of greater importance, however is the variation of δ with composition of the specimen and with angle of incidence of the primary beam. It is the latter effect which causes the considerable contrast in the image generated by the scanning microscope when it is used in the secondary electron detection mode.

For a slow moving secondary electron in the specimen the probability of a collision with another electron will be proportional to the number of electrons in its path. This means the probability of traversing a path of length x is $\exp -\frac{x}{x_o}$. This has been experimentally confirmed[11] and it means that there is a depth x_o below the specimen surface from beneath which few secondaries can escape. If the primary beam strikes the specimen at normal incidence secondaries from the first x_o cm of the path will escape. When the beam strikes at an angle θ with respect to the normal the number of secondaries will be then increased by $\frac{1}{\cos\theta}$. This effect creates contrast in the scanning microscope image as a function of specimen shape.

The secondary electron emission coefficient due to ion bombardment, γ_i, depends on the mechanism for production of secondaries by ions which is quite different than the mechanism for production by electrons. There are two components to γ_i, one due to potential ejection of secondary electrons, the other due to kinetic ejection.[7,15,16]

Potential ejection is the name given to a variety of processes which are important only when the incident ion energy $E_i \lesssim 1$ keV. The most important process is[7] Auger neutralization of an ion, in which an electron from the target neutralizes the ion and the energy difference between the ionization potential of the atom and twice the work function of the target appears as an electron ejected from the target (the precise energy of this electron will depend on the electron band structure of the target). Kinetic ejection is important when the incoming ions have energies $\gtrsim 0.5$ keV. The physical process is the release of bound electrons from atoms near the target surface, and is independent of work function and ion velocity (hence ion mass, for a given bombarding energy).[7] γ_i increases steadily as E_i increases up to rather high energies, ~ 100 keV, levels off and then decreases.[15] Values of γ_i depend on the ion-target system and range from about 0.2 - 2 at E_i = 10 keV. The systematics are complicated and sometimes plots of γ_i versus energy cross for different ions bombarding the same target.[17] γ_i varies according to $\frac{1}{\cos\theta}$ with variation of incident angle, as with electrons.[7,16] The energy distribution of the secondary electrons is peaked at less than 5 eV,[16] and is not sensitive to E_i.

When single crystals of metal are bombarded the value of γ_i oscillates as the angle of incidence from the normal increases,[17] and the yields γ_i from different crystal faces of the same metal can be very different.[18] The latter effect is believed to be due

to the varying density of atoms per cm^2 of the different crystal faces seen by the incoming ions. The more closely packed the atoms are, the higher γ_i is.[18]

It is evident that there are a variety of mechanisms which will affect γ_i and hence the contrast in an image formed by a scanning ion microscope. The most important ones are variation of γ_i with work function and with angle of incidence of the beam to the target surface normal. The latter effect is the larger and results in images with an appearance similar to those generated by a scanning electron microscope. In the case of organic specimens data for ions are apparently not yet available, but one may conjecture similar effects.

I. The Optical Components

The optical components used in the SIM consist of two einzel lenses, a double deflection beam deflector, a post lens beam deflector, a stigmator and a beam steerer. The einzel lenses were designed by Dr. Gertrude Rempfer and come from an electrostatic TEM manufactured by Elektros, Inc., as do the stigmator and beam steerer. The double deflector system was designed by the author and was removed from the column recently (November, 1976) to make room for the stigmator. It was replaced by a post lens deflector located underneath the projector lens. This deflector was also designed by the author.

The heart of the optical system is the einzel lens. The properties of the objective and projector lenses may be found in Figs. 21 and 22. In Fig. 23 are curves showing the calculated current vs.

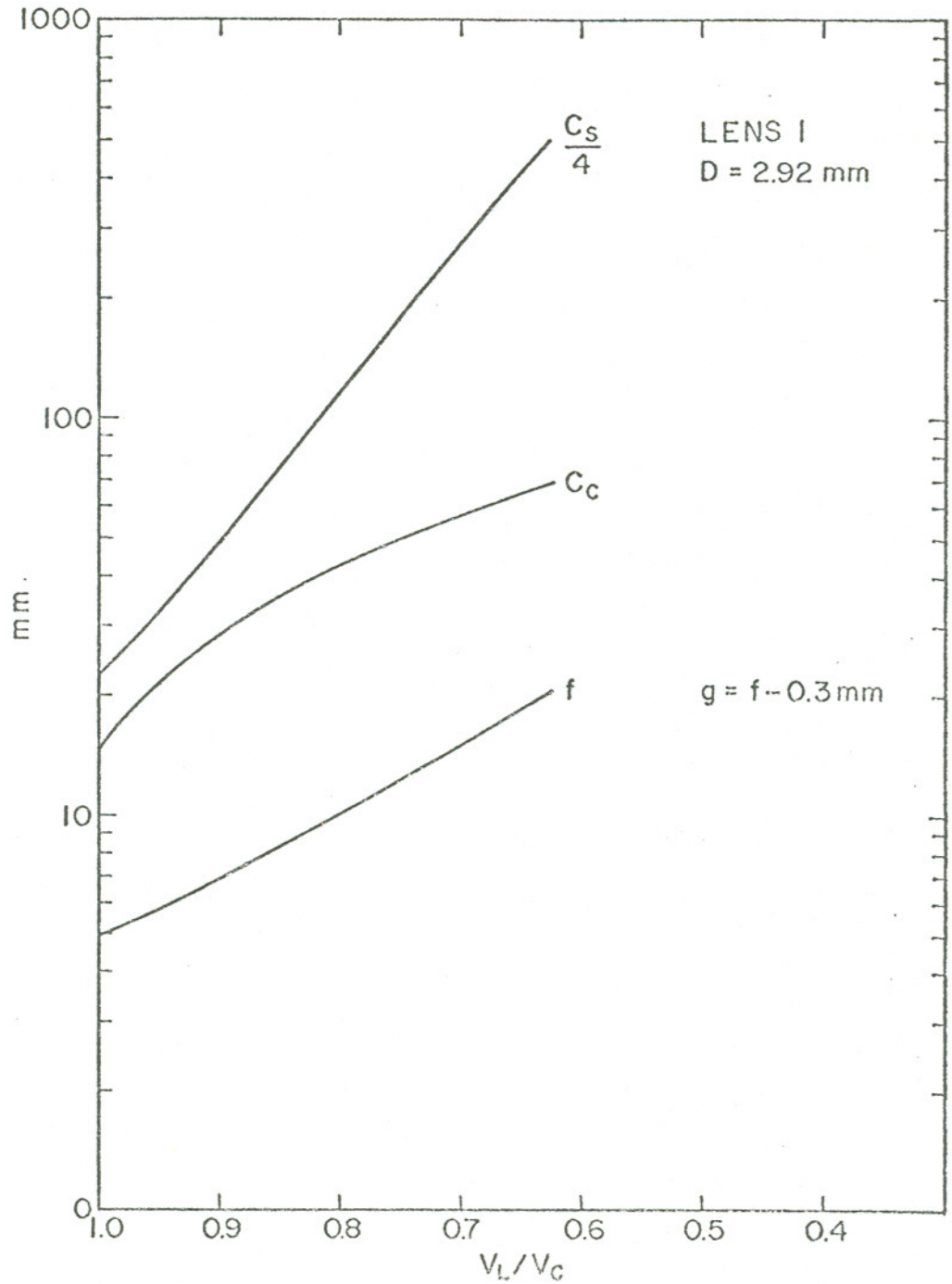

Fig. 21. Chromatic aberration, spherical aberration and focal length of the objective lens as a function of the ratio of lens to beam voltage. g is position of focal point with respect to lens center.

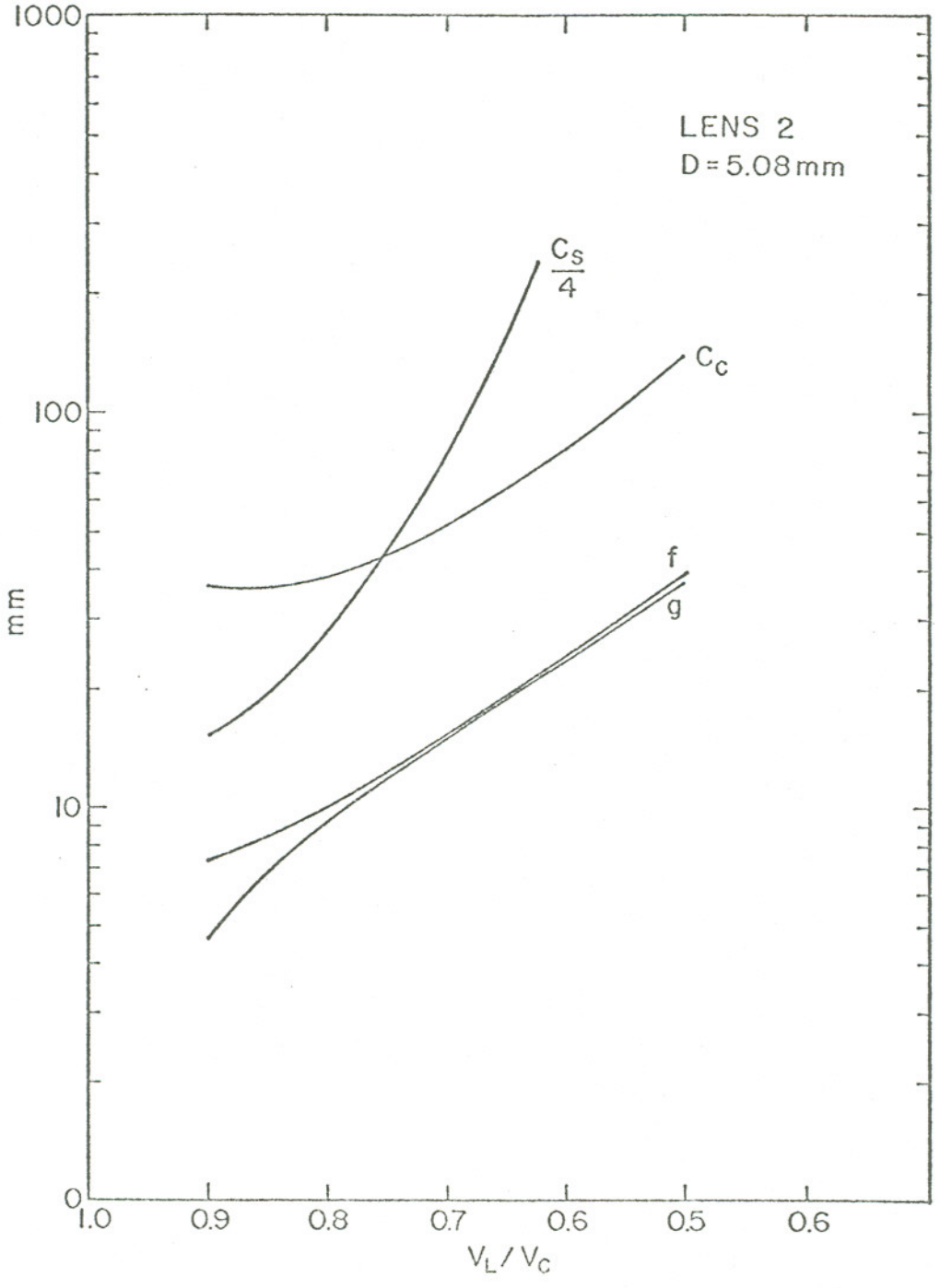

Fig. 22. Chromatic aberration, spherical aberration, focal length and focal position g of the projector lens as a function of the ratio of lens to beam voltage.

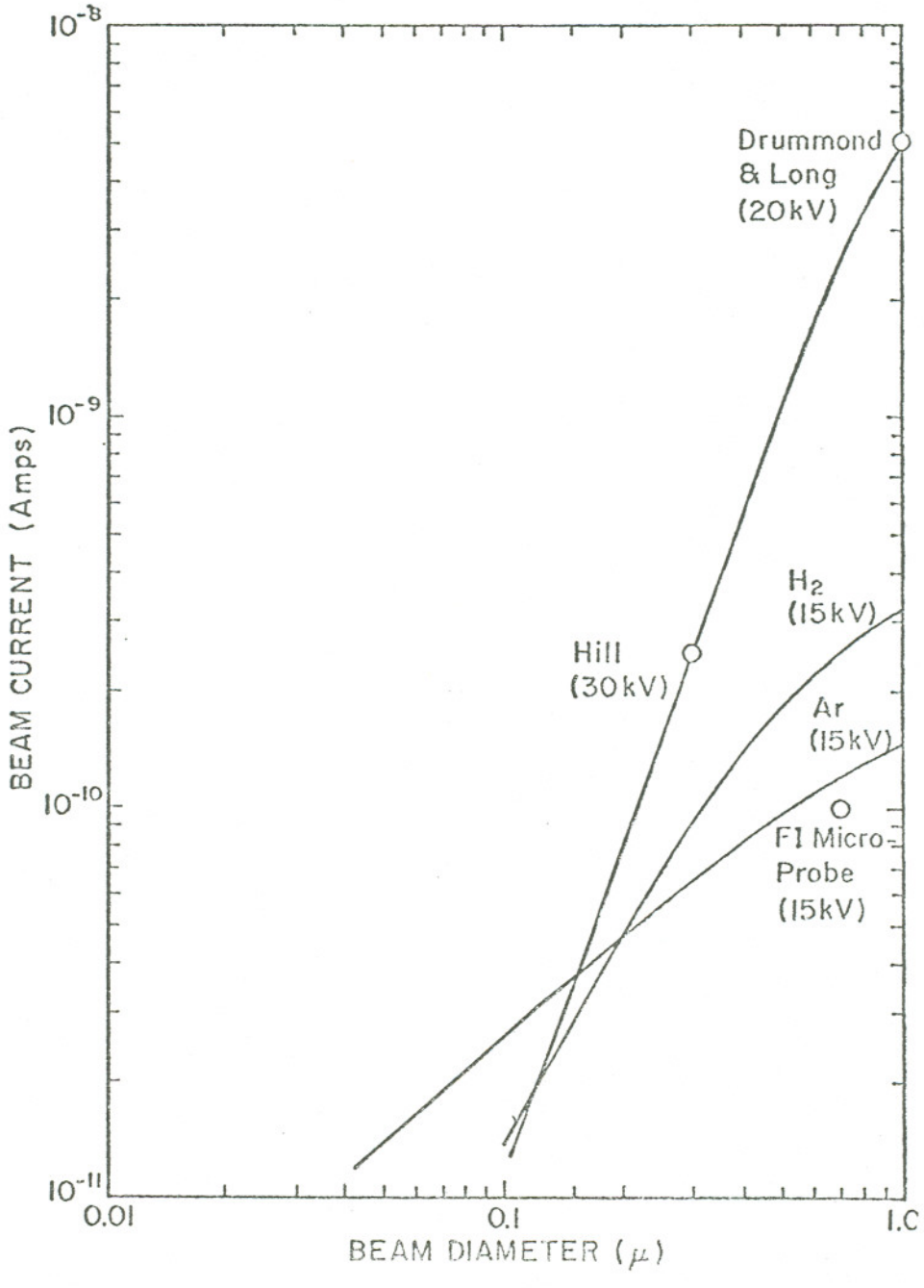

Fig. 23. Estimated current vs. beam diameter for a duoplasmatron source, extrapolated from work by Drummond and Long[20] and by Hill.[19] Calculated current vs. beam diameter for the FI source for Ar and H_2 and actual performance point of the SIM.

beam diameter for the SIM with these lenses, based on a source sensitivity for hydrogen of 5×10^{-5} A/sr torr and a source pressure of 2×10^{-2} torr, and a sensitivity of 1×10^{-5} A/sr torr for Ar. The lens parameters are from Figs. 21 and 22 with focal lengths of $f_{obj} = 8.5$ mm, $f_{proj} = 45$ mm and $V_{acc} = 15$ kV for hydrogen and $V_{acc} = 40$ kV for Ar. The results of Drummond and Long,[19] Hill[20] and the present SIM are shown as well.

J. Micrographs

Eight micrographs representative of the capabilities of the SIM as of December 1976 may be found at the end of this section. The subjects are: (1) an A.C. dropoff tungsten field emitter spot-welded to a 0.010" tungsten wire; (2) a portion of an integrated circuit with detail of the electrical runs obliterated by charging of the silicon substrate; (3) a portion of the leg of a housefly, gold coated; (4) a pad on an integrated circuit with a 0.002" gold wire attached; (5) a D.C. dropoff tungsten field emitter; (6) a higher magnification picture of the same field emitter as in (5); (7) a higher magnification micrograph of the same emitter; (8) an integrated circuit lightly gold coated to minimize specimen charging.

The first four micrographs were taken with the double deflection system and the secondary electron signals were amplified with a linear amplifier. The next four micrographs were taken with

beam diameter for the SIM with these lenses, based on a source sensitivity for hydrogen of 5×10^{-5} A/sr torr and a source pressure of 2×10^{-2} torr, and a sensitivity of 1×10^{-5} A/sr torr for Ar. The lens parameters are from Figs. 21 and 22 with focal lengths of $f_{obj} = 8.5$ mm, $f_{proj} = 45$ mm and $V_{acc} = 15$ kV for hydrogen and $V_{acc} = 40$ kV for Ar. The results of Drummond and Long,[19] Hill[20] and the present SIM are shown as well.

J. Micrographs

Eight micrographs representative of the capabilities of the SIM as of December 1976 may be found at the end of this section. The subjects are: (1) an A.C. dropoff tungsten field emitter spot-welded to a 0.010" tungsten wire; (2) a portion of an integrated circuit with detail of the electrical runs obliterated by charging of the silicon substrate; (3) a portion of the leg of a housefly, gold coated; (4) a pad on an integrated circuit with a 0.002" gold wire attached; (5) a D.C. dropoff tungsten field emitter; (6) a higher magnification picture of the same field emitter as in (5); (7) a higher magnification micrograph of the same emitter; (8) an integrated circuit lightly gold coated to minimize specimen charging.

The first four micrographs were taken with the double deflection system and the secondary electron signals were amplified with a linear amplifier. The next four micrographs were taken with

the post lens deflection system and here the signals were amplified with a logarithmic amplifier. The reduced contrast due to the logarithmic response gives a result more pleasing to the eye. Also, more detail is captured on film because the dynamic range of the film is frequently exceeded with the linear system. The micrographs were taken with beam currents between 3 and 30 pA and with scan rates of 330 Hz in the vertical direction and 0.045 Hz in the horizontal direction (22 second sweep). Micrographs (1), (3) and (4) were taken with current in the low pA range while the rest were taken with higher currents (in the 30 pA range). The effect of shot noise is quite apparent in the former pictures.

If the magnification is 100X and the resolution 0.7 μm, then in a micrograph scanned at the given rate each area 0.7 μm square will be covered by the beam for ≃ 0.5 microseconds. If the current on the specimen is 5 pA and one secondary electron is produced per incident ion then $\sqrt{N}/N = 25\%$. When the current is 50 pA, $\sqrt{N}/N = 8\%$. The scan generator in use has a maximum scan of about 22 seconds. It is evident that an improvement in the picture quality will be brought about when this is increased.

The increased number of secondary electrons produced when the beam strikes the specimen at a large angle is readily apparent, for example in micrograph (5) where the rapidly changing angle of the wires with respect to the beam creates great contrast.

The quality of the micrographs is not as good as those taken on commercial SEM's. It has shown a more or less steady improvement, however, and with improvements in the electronics and the addition of the stigmator the process of improvement will continue.

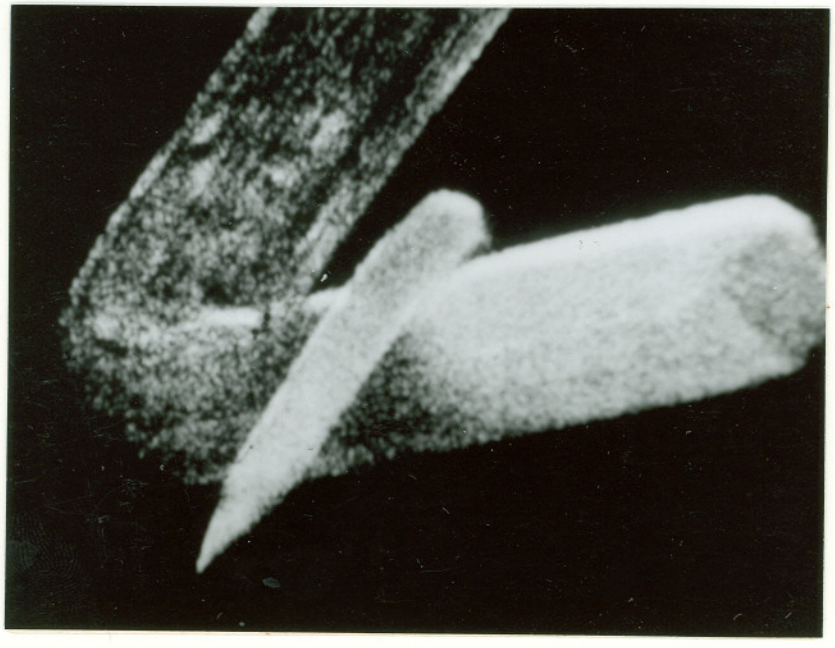

Micrograph 1

An A.C. dropoff tungsten field emitter spotwelded to a 0.010" tungsten wire. 100X, H_2.

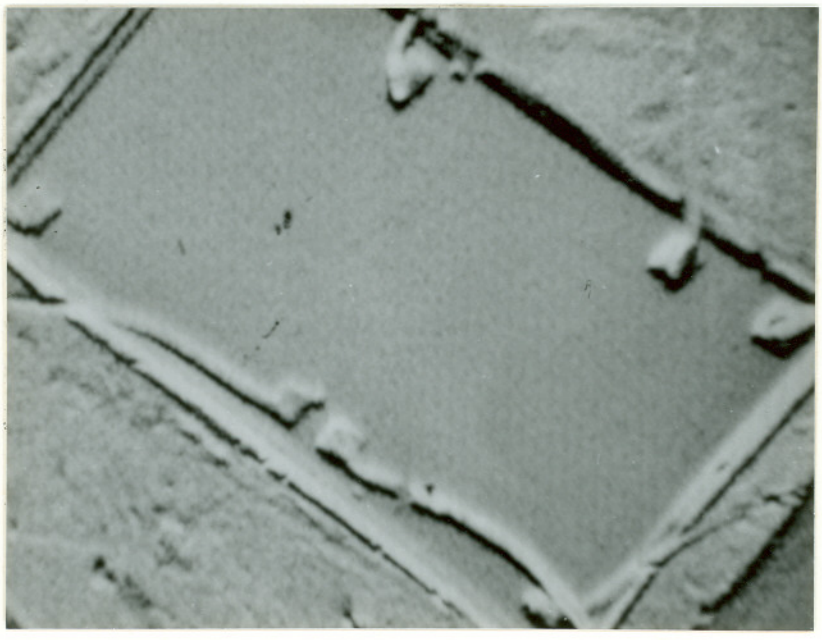

Micrograph 2

Integrated circuit. 50X, H_2. Detail is washed out by the charging of the Si substrate.

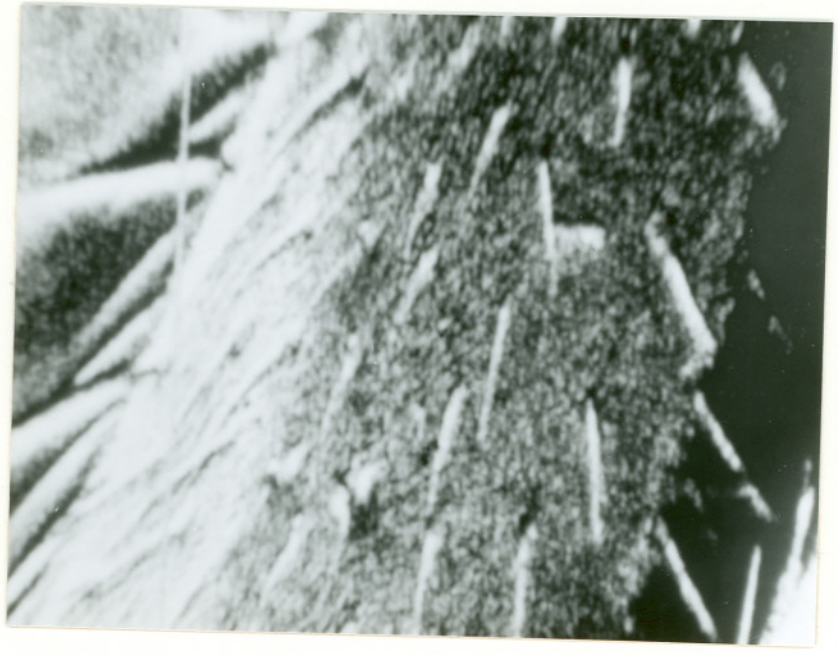

Micrograph 3

Leg of a housefly coated with a thin ($\sim$ 100 angstrom) layer of gold to prevent charging. 700X, H_2.

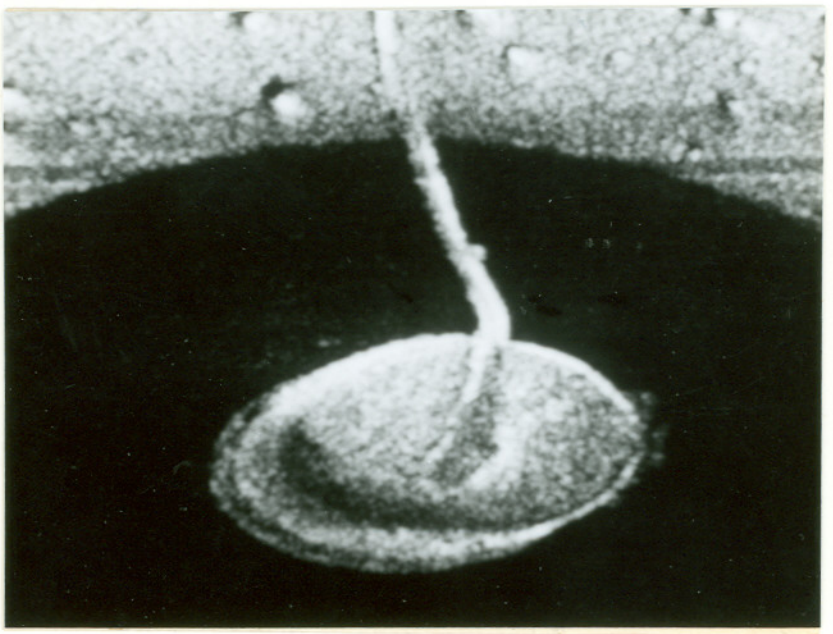

Micrograph 4

Pad on an integrated circuit. Black area surrounding connector is insulator with a lower secondary electron coefficient than the gold. 50X, H_2.

Micrograph 5

D.C. dropoff tungsten field emitter. 140X, H_2. Note die marks produced by wire drawing process.

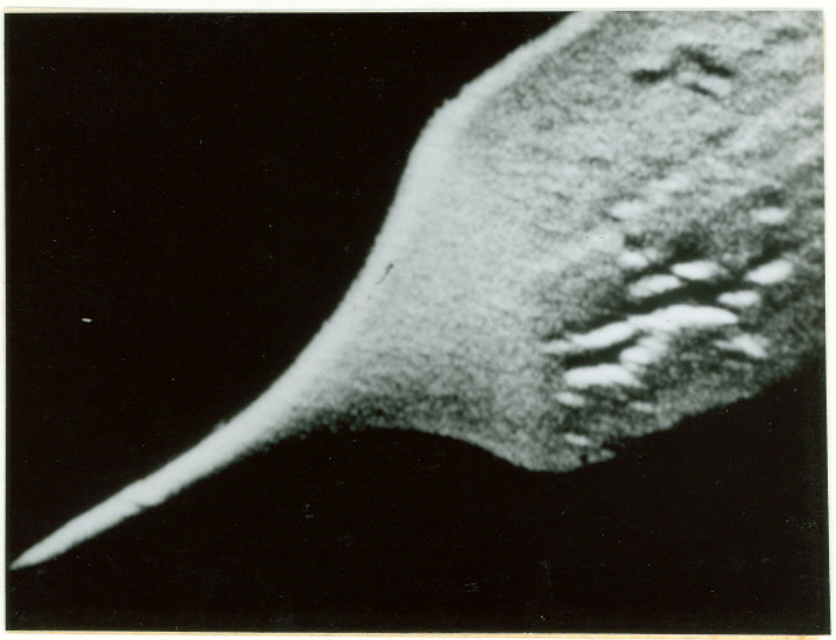

Micrograph 6

The same emitter as in micrograph 5. 440X.

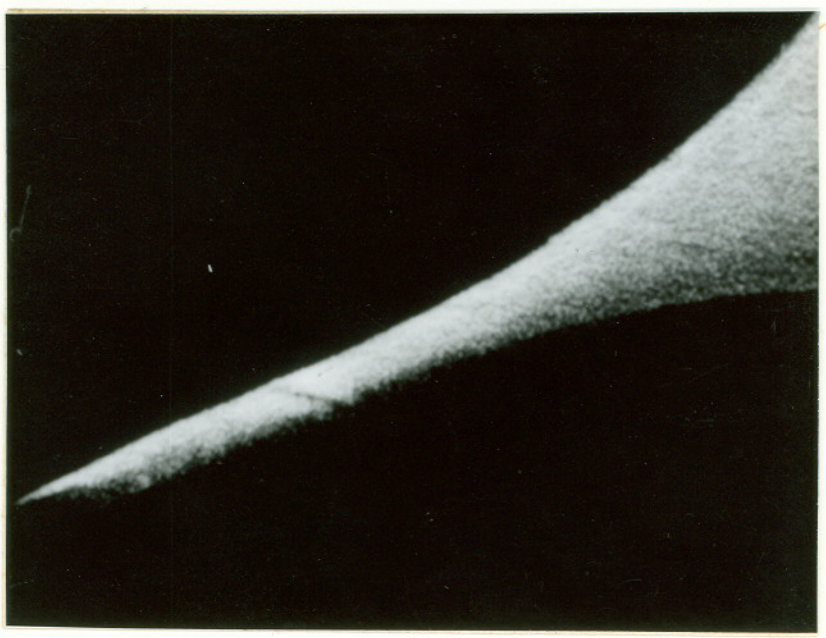

Micrograph 7

The same emitter as in micrograph 5. 770X. Note the fault or contamination near the end of the emitter. The emitter seems to disappear at about 0.5 microns diameter. Actual diameter of the end of the emitter is about 0.05 microns.

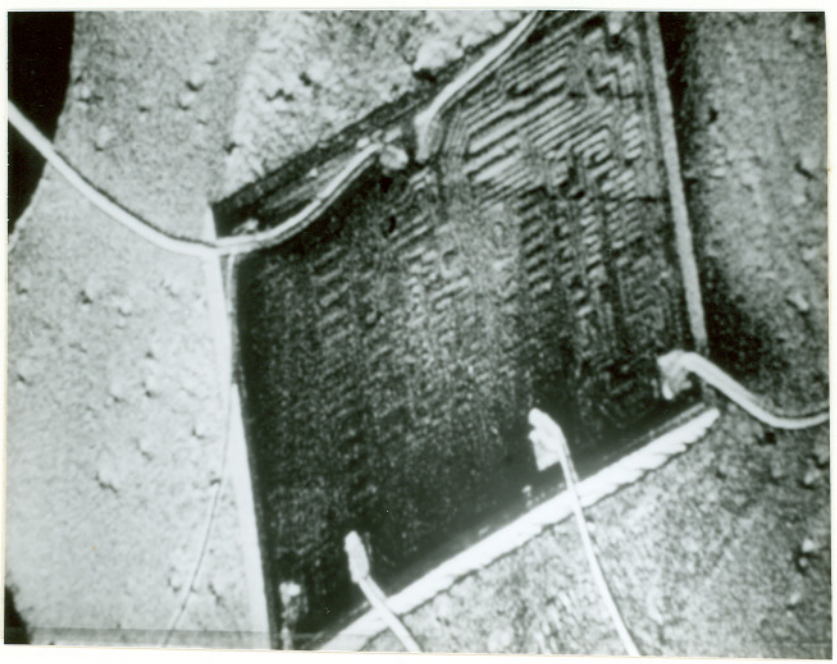

Micrograph 8

Integrated circuit lightly coated with gold to prevent charging. 40X, H_2.

TABLE I

Noise Data For FI Beam

Taken With 10 Hz Bandwidth

f	$I - I_{BG}$	$\langle \Delta I^2 \rangle^{1/2} - \langle \Delta I_{BG}^2 \rangle^{1/2}$	S/N
1 Hz	21 μA	0.5 μA	42
10	21	0.2	105
60	21	0.2	105
1	11	0.5	22
10	10	0.1	100
60	10	0.1	100

TABLE II

High Voltage (kV)	Aperture Angle	S/N
12	14°	4
12	27°	9
13	14°	5
13	27°	10
14	14°	8
14	27°	15

Frequency Range: f = 1 Hz, Δf = 10 Hz. Emitter and gas temperature: 77 K. Current measured at specimen.

Fig. 24

A micrograph of a polycrystalline Ir emitter, 40,000X. Note uneven etching. Micrograph taken with a conventional TEM.

REFERENCES

1. B. J. Waclowski and E. W. Müller, J. Appl. Phys. 32 (1961) 1472.
2. T. T. Tsong and E. W. Müller, J. Chem. Phys. 41 (1964) 3279.
3. A. J. Jason, Phys. Rev. 156 (1967) 266.
4. A. Jason, B. Halpern, M. G. Inghram and R. Gomer, J. Chem. Phys. 52 (1970) 2227.
5. H. A. M. Van Eeklen, Surf. Sci. 21 (1970) 21.
6. Allen R. Anway, J. Phys. Chem. 50 (1969) 2012.
7. G. Carter and J. S. Colligon, "Ion Bombardment of Solids," American Elsevier Publishing Co. 1968.
8. M. G. Wells and D. A. King, J. Phys. C, 7 (1974) 4053.
9. P. W. Palmberg, J. Appl. Phys. 38 (1967) 2137.
10. I. M. Bronshteyn and B. S. Frayman, Radiotekn. i. Elektron. 7 (1962) 1643-8.
11. H. Bruining, Secondary Electron Emission, Pergamon Press (1954).
12. R. Kollath, Handbuch Der. Physik, Vol. 21 (1956) 232-303.
13. E. M. Barody, Phys. Rev. 78 (1950) 780.
14. J. G. Trump and R. J. Van de Graaf, J. Appl. Phys. 18 (1947) 327.
15. U. A. Arifov, "Interaction of Atomic Particles With the Surface of a Metal," Izdatel'stvo Akademii Nauk Uzbekskoi SSR, Tashkent, 1961.
16. M. Kaminsky, "Atomic and Ionic Impact Phenomena on Metal Surfaces," Academic Press, 1965.
17. G. D. Magnuson and C. E. Carlston, Phys. Rev. 129 (1963) 2403.

super large capacity archival storage system (10^{15} bits). The Oregon Graduate Center is, in effect a subcontractor to develop FE and FI sources for this project.

REFERENCES

1. B. J. Waclowski and E. W. Müller, J. Appl. Phys. 32 (1961) 1472.

2. T. T. Tsong and E. W. Müller, J. Chem. Phys. 41 (1964) 3279.

3. A. J. Jason, Phys. Rev. 156 (1967) 266.

4. A. Jason, B. Halpern, M. G. Inghram and R. Gomer, J. Chem. Phys. 52 (1970) 2227.

5. H. A. M. Van Eeklen, Surf. Sci. 21 (1970) 21.

6. Allen R. Anway, J. Phys. Chem. 50 (1969) 2012.

7. G. Carter and J. S. Colligon, "Ion Bombardment of Solids," American Elsevier Publishing Co. 1968.

8. M. G. Wells and D. A. King, J. Phys. C, 7 (1974) 4053.

9. P. W. Palmberg, J. Appl. Phys. 38 (1967) 2137.

10. I. M. Bronshteyn and B. S. Frayman, Radiotekn. i. Elektron. 7 (1962) 1643-8.

11. H. Bruining, Secondary Electron Emission, Pergamon Press (1954).

12. R. Kollath, Handbuch Der. Physik, Vol. 21 (1956) 232-303.

13. E. M. Barody, Phys. Rev. 78 (1950) 780.

14. J. G. Trump and R. J. Van de Graaf, J. Appl. Phys. 18 (1947) 327.

15. U. A. Arifov, "Interaction of Atomic Particles With the Surface of a Metal," Izdatel'stvo Akademii Nauk Uzbekskoi SSR, Tashkent, 1961.

16. M. Kaminsky, "Atomic and Ionic Impact Phenomena on Metal Surfaces," Academic Press, 1965.

17. G. D. Magnuson and C. E. Carlston, Phys. Rev. 129 (1963) 2403.

18. G. D. Magnuson and C. E. Carlston, Phys. Rev. 129 (1963) 2409.

19. A. R. Hill, Nature 218 (1968) 292.

20. I. W. Drummond and J. V. P. Long, Premiere Conference International Sur Les Sources D'ions, Saclay, France, 1969.

V. CONCLUSIONS

The goals of this project were to demonstrate the feasibility of using the FI phenomenon in a practical ion source and to build an ion microprobe which utilizes the source. These may be considered the initial goals in a longer term project to produce high resolution ion beams for a variety of purposes, and as such they have been fulfilled. There remains much work to be done to improve the SIM, primarily involving source improvement to increase brightness and emitter uniformity.

The great brightness of the FI source makes it attractive for ion microprobes where resolution $\lesssim$ 2000 Å is desired. With the simple optical system now employed it should be possible to achieve $\lesssim$ 1000 Å resolution with monoatomic gases, the limit being chromatic aberration. The application of ion probes with beam diameters $\lesssim$ 1000 Å for microfabrication purposes is an exciting possibility which may be realized in the near future. Work is in progress at the Oregon Graduate Center using the SIM for microscopy and the FI source has been used at the University of Chicago for STIM since 1974. The Hughes Research Laboratory is investigating the possibility of microfabrication of electronic devices with the FI source and the IBM Corporation has evidenced interest in investigating it, presumably for similar purposes. The General Electric Company is prime contractor for a Department of Defense project to develop a

super large capacity archival storage system (10^{15} bits). The Oregon Graduate Center is, in effect a subcontractor to develop FE and FI sources for this project.

VITA

The author was born in New York City on 30 April, 1942 and was educated at M.I.T., receiving a Bachelor's Degree in Physics in 1964. Further work in experimental nuclear physics followed at the University of Pittsburgh. In 1970 the author became involved with a small company which attempted to market a transmission electron microscope with electrostatic lenses. This attempt was unsuccessful and the effort abandoned in 1973. In 1974 with an aroused interest in electron optics, the author approached the Oregon Graduate Center about the possibility of writing a Ph.D. thesis on some subject involving electron optics. Work on this project began in late 1974 and began to produce meaningful results about three months later. The SIM produced its first image on 28 August, 1975. Results were first presented in April of 1975. Publications by the author are:

J. H. Orloff and W. W. Daehnick, "Elastic Scattering of O^{16} by Ca^{40}, Al^{27}, C^{12}, Li^{7} and Li^{6}," Phys. Rev. C3 (1971) 430; W. W. Daehnick, J. H. Orloff, T. Canada and T. S. Bhatia, "Nuclear Structure of ^{46}K: Studies With ^{48}Ca (d, $\alpha\gamma$)^{46}K and Deuteron Transfer Reactions," Phys. Rev. C10 (1974) 136; J. H. Orloff and L. W. Swanson, "A Study of a Field Ion Source for Microprobe Applications," J. Vac. Sci. Tech. 12 (1975) 1209; J. Orloff and L. W. Swanson, "A Scanning Ion

Microscope With a Field Ionization Source," SEM/1977, Proceedings of the Tenth Annual Scanning Electron Microscope Symposium (in print).

The author is currently an Instructor at the Oregon Graduate Center and is a consultant for the Hughes Research Laboratories, Malibu, California.